Josephson transport driven by optically imaged and manipulated single Abrikosov vortices

Siddharatha Thakur

THÈSE DE DOCTORAT

pour obtenir le grade de

Docteur de l'Université de Bordeaux

ÉCOLE DOCTORALE DES SCIENCES PHYSIQUES

ET DE L'INGÉNIEUR

SPÉCIALITÉ LASER, MATIÈRE, NANOSCIENCES

---

par

Siddharatha THAKUR

le 15 décembre 2022

Josephson transport driven by optically imaged and manipulated single Abrikosov vortices

Transport Josephson piloté par des vortex d'Abrikosov individuels imagés et manipulés optiquement

Commission d'examen:

Président	M. Alexandre Bouzdine	Professeur (Univ. Bordeaux)
Rapporteurs:	M. Javier Villegas	Directeur de Recherche CNRS (THALES)
	M. Stéphane Berciaud	Professeur (Univ. Strasbourg)
Examinateurs:	Mme. Brigitte Léridon	Chargée de Recherche CNRS (ESPCI)
	M. Edward Goldobin	Professeur Associé (Univ. Tübingen)
Membres invités:	M. Hamed Majedi	Professeur (Univ. Waterloo)
Directeur de thèse:	M. Brahim Lounis	Professeur (Univ. Bordeaux)
Co-directeur:	M. Philippe Tamarat	Professeur (Univ. Bordeaux)

Laboratoire Photonique Numérique et Nanosciences
UMR5298, 33400 Talence, France.

I am time,
the destroyer of all.
I have come to consume the world.

कालोऽस्मि
लोकक्षयकृत्प्रवृद्धो
लोकान्समाहर्तुमिह
प्रवृत्तः |

The Bhagavad Gita: Chapter 11, Verse 32

Contents

Acknowledgements

The work of this thesis was conducted in the Laboratoire Photonique Numérique et Nanosciences. I would like to extend my gratitude to the directors of the laboratory during this time, Philippe Bouyer and Laurent Cognet. I would also like to extend my heartfelt gratitude to the members of the jury who accepted their roles as part of my committee. Their time, effort and presence was greatly appreciated during the course of my defense process. The opportunity to engage and discuss with these distinguished researchers during this process was an incredible opportunity and an appreciated generosity.

Thank you to Brahim Lounis, director of my thesis and leader of the Nanophotonics group. His active engagement, enthusiasm and guidance helped me develop as a young researcher in all aspects. I would like to especially thank him for the opportunity that he gave me. His confidence and consistent drive was always an asset to push past the many hurdles that we faced in this project, and there were many. My gratitude as well to Philippe Tamarat, co-director of this thesis, his generosity with his time and patience is something I have greatly appreciated and relied on. He has been a consistent and reliable aid in all aspects of this work. I would also like to thank Alexandre Bouzdine for his wealth of knowledge and kind spirit. Finally, I want to extend my heartfelt appreciation to Hamed Majedi, his kindred spirit, guidance and support has been a great help during this challenging pursuit.

Having spent more than 4 years at LP2N I have had the privilege to work with and get to know some wonderful people. When I started I had the good fortune to meet Antonine and William who were kind and welcoming, that I decided to return to Bordeaux as a Ph.D student. Throughout my time the group evolved inviting new members and we grew from colleagues to friends, encouraging each other when we felt disheartened by the day's challenges. In that spirit I want to thank Lei, Malo, Elise, Matthias and Quentin for their friendship and support. In this fire we have forged a bond that will stay with me. It is the coffee and table tennis that keeps the wheel turning. The endearing relationships extends beyond the team and to the people in lab. In communal moments like having lunch together we shared our woes and victories. Thank you for your friendship JBG, Luisa, Dylan, Vincent, Celia, Somen, Naveen, Ani and Alberto. To Anna, your patience and support sustained me through this time, thank you.

To my parents, if I am here it is because of you. We know where we came from, the struggle, the sacrifice. In the end, this is dedicated to you.

Nanophotonics 2022. Credit to the artist Luisa Loranca.

List of Figures

Introduction

Historical context

The infamous story of discovery of superconductivity in 1911 by Heike Kamerlingh Onnes and colleagues in Leiden is scientific lore. The series of events leading to this discovery was grounded in a more fundamental question: *What are the ultimate constituents of matter?* This question led to a century of work by scientists trying to liquefy gases, for their potential use as refrigerants, so matter could be studied at low temperatures. This effectively was the inception of the field of low temperature physics. Following the successful liquefaction of helium in 1908 in Leiden, temperatures as low as 1K were suddenly achievable. Cooling an extremely pure sample of mercury, a sudden drop in resistance was observed at 4.2K, which was reversible above this *critical temperature* (T_c)[1]. This phenomenon was dubbed the *superconducting state*. By 1914, physicists would make pilgrimages to Leiden to observe the persistent current in a loop of superconducting wire, interacting with a common magnetic needle.

Onnes was awarded the Nobel Prize for the liquefaction of helium and the significance of his achievement was evident by the fact that since his initial success in 1908, for 15 years Leiden was the only place on Earth where liquid helium could be produced. However, in 1923 Leiden lost its monopoly on liquid helium research, as Walther Meißner in Berlin among others had managed to construct their own liquefaction setups. Meißner had designed an experiment to determine whether the current in a superconductor flows on its surface or in its bulk, by measuring the magnetic field between two tin cylinders. Meißner, along with Robert Ochsenfeld, carried out this experiment. They found that there was an increase of external field due to the expulsion of internal fields when the cylinders were cooled below T_c (*Meißner effect*)[2]. Superconductors were not only perfect conductors, but also perfect diamagnets .

The discovery of the Meißner effect proved to be a crucial turning point in the theoretical development of superconductivity. It was around this time at Oxford when two brothers fleeing Nazi Germany, Heinz and Fritz London, worked out an electrodynamical model for the behaviour of superconductors, reconciling perfect conductivity with diamagnetism[3]. The effects of external fields and temperature on the supercon-

[1] H. K. Onnes. *The resistance of pure mercury at helium temperatures*. Commun. Phys. Lab. Univ. Leiden, 12, 1911.

[2] W. Meissner & R. Ochsenfeld. *Ein neuer Effekt bei Eintritt der Supraleitfähigkeit*. Naturwissenschaften Vol 21, 787–788, 1933.

[3] H. London & F. London. *The Electromagnetic Equations of the Supraconductor*. Proceedings of the Royal

ducting condensate were uncharted at the time Ginzburg and Landau proposed their phenomenological model in 1950[4]. The superconducting state was represented by a thermodynamic variable or an *order parameter*, governed by an equation similar to the Schrödinger equation. The resulting analysis could account for the thermodynamic behaviour of the superconducting condensate as it passed through a phase transition, and for its spatial behaviour near a normal boundary. The real significance of the wavefunction-like order parameter would be fully understood eventually when the microscopic theory by Bardeen, Cooper and Schrieffer, the BCS theory, was introduced in 1957[5]. The theory was an elegant formulation in which electrons form a coherent phonon coupled ground-state acting like bosonic particles, *Cooper pairs*, producing unhindered macroscopic supercurrent. The theory succeeded in accounting for the many puzzling phenomena of superconductivity, and satiating the sceptics who doubted the grounds of Ginzburg and Landau's theory, as it lacked microscopic basis at the time. However, even with that understanding, the much simpler and easier-to-use Ginzburg-Landau model remained (and remains) the every-day working theory used by theorists and experimentalists alike to analyse all manner of complex phenomena in superconductivity.

On the experimental front, studies on the critical field of superconducting thin films had yielded perplexing results, inconsistent with the Ginzburg-Landau model. The surface energy separating the superconducting and normal phase was always expected to be positive, but one of Landau's students at the time, Alexei Abrikosov, decided to consider the case for negative energy. Upon calculating the implications of this case, he found that in the presence of a magnetic field a new superconducting state was possible, one where the diamagnetism is relaxed and the magnetic flux can penetrate the superconductor. This mixed state manifested as quantised flux lines called *Abrikosov vortices* (AV), thus forming a new class of superconductors dubbed as *type-II*. An AV carries a flux quantum $(h/2e)$ and a circulating supercurrent around the vortex core, inducing a 2π phase rotation in the superconducting condensate[6]. Compared to the perfectly diamagnetic type-I superconductors, type-II materials allow for higher operational critical fields, making them more appealing for applications. Another foundational phenomenon in superconductivity is the *Josephson effect*, which was postulated by Brian Josephson in 1962 as a phenomenon where Cooper pairs could flow across an insulating barrier from one superconducting electrode to another, by means of quantum tunneling[9]. The Josephson effect exhibits a precise relationship between different physical quantities, such as voltage and frequency. This has become the basis for what is considered the global standard for one volt.

The next milestone in practical use of superconducting materials was the operational

Society A, 149, 1935.

[4]V. L. Ginzburg & L.D. Landau. *On the Theory of superconductivity*. Zh .Eksp. Teor. Fiz., 20, 1950.

[5]L. N. Cooper, J. R. Schrieffer & J. Bardeen. *Theory of Superconductivity*. Physical Review, 108, 1957

[6]A. A. Abrikosov. *On the magnetic properties of superconductors of the second group*. Journal of Experimental and Theoretical Physics, 5, 1957.

[9]B. D. Josephson. *Possible new effects in superconductive tunnelling*. Physics Letters, 1, 1962.

temperature limitation. In 1986 Bednorz and Müller at IBM Zurich observed superconductivity in the temperature range of 30-35K in a copper-oxide based compound[7]. This kickstarted the field of high-temperature superconductivity (HTS), and further exploration of materials with higher and higher critical temperatures. HTS materials are a subset of type-II superconductors. One of the more prominent HTS materials is yttrium barium copper oxide (YBCO) which can become superconducting at 90K, above the boiling point of liquid nitrogen. The advent of having superconductivity at high temperatures is an appealing prospect as it widens the scope of its applications.

Applications

Superconductive materials have found widespread applications in a diverse array of fields. Applications tend to be categorised based on different operating temperatures, cooling costs, required magnetic fields and material properties. Superconducting electromagnets based on low-temperature superconductors (LTS) cooled with liquid helium are capable of generating intense magnetic fields, while operating at less cost compared to their equivalent non-superconducting magnet due to reduced energy dissipation. These magnets are used to produce large-volume, stable, and high-intensity magnetic fields (above 1 T) for magnetic resonance imaging (MRI) and nuclear magnetic resonance (NMR) spectrometer systems. Particle accelerators such as the Large Hadron Collider at CERN and particle fusion reactors make use of these electromagnets to generate large fields required for particle acceleration and reaction confinement, respectively. High-speed trains using magnetic levitation technology use LTS alloys to achieve fast and friction-less transport. A combination of nanostructured LTS/HTS materials have the capability for ultrahigh magnetic fields, and will most likely be integrated in the next generation of accelerators, reactors and magnetic levitation systems. More large scale industrial applications requiring lower fields ($< 1\ T$) use HTS materials cooled with liquid nitrogen. The limitation of HTS materials tends to be that they are ceramic materials that are brittle, expensive to manufacture and cannot easily be formed into wires. Despite that, industrial applications such as power cables, transformers, generators, motors and induction heaters are prevalent. Projects to design electric grid systems built from superconducting transmission lines are currently in development across the world[8].

In contrast to these large scale applications that exploit primary characteristics of superconductivity, the subtle properties find niche applications. A superconducting nanowire single-photon detector is the fastest single-photon detector for photon counting, and is based on measuring critical current changes due to breaking of Cooper pairs. It provides very high detection efficiency, very low dark counts and very low timing jitter, as compared to other single-photon detectors. It is a key enabling technology for quantum optics and optical quantum technologies. Another important application is

[7] J. G. Bednorz & K. A. Müller. *Possible high-T_c superconductivity in the Ba-La-Cu-O system*. Zeitschrift für Physik B, 64, 1986.

[8] C. Yao & Y. Ma. *Superconducting materials: Challenges and opportunities for large-scale applications*. iScience, 24, 2021.

the superconducting quantum interference device (SQUID), which is one of the most sensitive magnetometers available, with a sensitivity of 10^{-14} T. The SQUID is made from a more fundamental component called a *Josephson junction* (*JJ*). Additionally, JJs form the fundamental constituent for superconducting tunnel junction detectors, single-electron transistors, superconducting qubits and RSFQ digital electronics. The field of superconductivity is quite mature in this respect, as the applications find their place in varied industries and at varied scales.

Motivation

As the miniaturization of semiconductor-based electronics reaches its fundamental limits, realisation of new robust platforms becomes essential to herald a new era in technological evolution. Potential alternative platforms include optical, superconductor, atomic, molecular, and numerous solid-state systems. While these alternatives are well suited for niche applications, mass implementation is often hindered by fundamental limitations. In addition to that, advancement also faces socio-economic and environmental challenges. The promise of widespread global digitalisation is projected to increase the energy demands of the information and communication technology sectors, using as much as 51% of global electricity by 2030 and strongly influencing global policy[10,11]. Considering these issues, superconductor electronics using JJs are the most feasible option given the high operating frequencies, low switching energies and current maturity of the field[12]. Superconductor switching operations can be performed on the order of millivolts compared to an equivalent semiconductor operation which requires volts. Superconducting logic circuits intrinsically generate less heat, and as a result, can be packed more densely than the semiconducting equivalent. JJs are also rapidly becoming an attractive component in quantum electronics due to their high non-linearity and long coherence times for quantum states. The maintenance costs of semiconductors exceed cryogenic refrigeration costs of superconductors in similar systems[13].

Modern large scale superconducting circuits are based on *rapid single flux quantum* logic (RSFQ), which uses a SQUID as its fundamental building component. The information is stored in the form of magnetic flux quanta which is read as single flux quantum voltage pulses. In comparison, using an AV driven JJ as the fundamental unit of the circuit presents the advantage of using only one JJ, which has the potential for higher density superconducting circuits. In the simple geometry of a planar JJ with a AV trapped in the electrodes, the vortex currents cross this barrier and induce a

[10] A. S. G. Andrae & T. Edler. *On Global Electricity Usage of Communication Technology: Trends to 2030*. Challenges, 6, 2015

[11] J. Morley et al. *Digitalisation, energy and data demand: The impact of Internet traffic on overall and peak electricity consumption.* Energy Research Social Science, 38, 2018.

[12] H. Rogalla & P. H. Kes. *100 Years of Superconductivity*. CRC Press Taylor Francis Group, 2011.

[13] D. S. Holmes et al. *Energy-Efficient Superconducting Computing—Power Budgets and Requirements*. IEEE Transactions on Applied Superconductivity, 23, 2013.

$0 \rightarrow \pi$ phase difference with the variation of the vortex-barrier distance[14]. This creates a possibility of developing a class of superconducting circuits based on AV driven Josephson transport. Moreover, AVs can be precisely manipulated by magnetic fields, current or light. A proof of concept of AV based random access memory (AVRAM) cell has indeed been reported[15]. Vortices were switched between two fabricated trap sites close and far from the junction, using current pulses. The system showed repeatability, distinguishability and high endurance in clearly distinguishable 1-0 switching functions of the AVRAM. The limitation of this design is the need for fabricated traps to determine the vortex-junction proximity, thus limiting it to a finite number of states which cannot be altered post-fabrication. In contrast to that, a dynamic method that can precisely move and position the vortex in this system would be advantageous in accessing intermediate states for complex operations in real time.

Proposition

In order to address this specific problem, this project focuses on exploiting the interplay of optics, magnetism and sub-micron scale superconductivity to develop methodologies and tools that allow for all optical control of Josephson transport. In our group we have developed several techniques that would allow the creation of a completely optical controlled system, from creating a junction to controlling its transport.

The approach focuses on utilising AVs as magnetic bits in order to modulate the local superconducting state. We have firstly developed a methodology based on the Kibbel-Zurek mechanism to spontaneously generate vortex and anti-vortex pairs[17]. Once generated the vortices can be separated and isolated, ready to be manipulated as modulation bits. Following that, a far-field optical tweezers technique that we developed facilitates highly precise and fast single vortex manipulation[16]. Using this technique the vortex can be moved close to junction without the limitation of pre-determined positions dictated by the fabricated traps. We can not only freely move and pin the vortex, but in the case of a high density of vortices in a devices that can contribute to systemic noise, we can also perform mass clean up. Therefore, this method can be scaled depending on the required scale of manipulation. Additionally, we can also potentially use optical patterning techniques to create illuminated junction-like structures by locally suppressing superconductivity[18]. With the applications of these techniques in a device, the system can be driven by an AV with complete optical control.

The work of this thesis builds on the previously developed techniques, further addressing a bottleneck due to optical imaging resolution, to attempt optically driven

[14] J. R. Clem. *Effect of nearby pearl vortices upon the I_c versus B characteristics of planar Josephson junctions in thin and narrow superconducting strips*. Physical Review B, 84, 10 2011.

[15] T. Golod et al. *Single abrikosov vortices as quantized information bits*. Nature Communications, 6, 10 2015.

[17] A. Rochet et al. *On-Demand Optical Generation of Single Flux Quanta*. Nano Letters, 9, 2020

[16] I. S. Veshchunov et al. *Optical manipulation of single flux quanta*. Nature Communications, 7, 2016.

[18] W. Magrini et al. *In-situ creation and control of Josephson junctions with a laser beam*. Applied Physics Letters, 114, 2019.

Josephson transport. The chapters in this manuscript are outlined as follows:

Ch 1. Superconductivity Phenomena. The first chapter presents some foundational history, theory and formulism necessary to understand and contextualise the work produced in this thesis. Starting from the discovery of the defining properties of superconductors, we build towards the various phenomenological and microscopic models formulated to explain this macroscopic quantum phenomena. Emphasis is placed on the properties of Abrikosov vortices and Josephson junctions due to their relevance to this work.

Ch 2. Experimental Methods. In this chapter the experimental methods used in this thesis are detailed. The primary technique used here is magneto-optical imaging and a detailed survey of the operating principles, magneto-optical indicators and imaging acquisition scheme are presented. The second half of the chapter focuses on the transport measurements. Here, the measurement equipment customised to work with the imaging apparatus is detailed. Following this the acquisition scheme, including the handling of the devices is provided.

Ch 3. Solid immersion magneto-optical imaging. The third chapter concerns the modified magneto-optical imaging set-up, which integrates a solid immersion lens to achieve an enhanced sub-micron resolution capable of resolving single vortices in superconducting devices. The subsequent sections focus on characterising the new imaging technique in vortex resolution and contrast. The experimental work is driven by finding the optimal conditions for imaging, while the numerical simulations focus on the potential sources of aberrations and loss in extinction that can affect the overall imaging quality.

Ch 4. Optically driven Josephson transport. In the fourth chapter we amalgamate all the techniques we have developed thus far and apply them on real devices. This chapter is separated into two primary parts. The first deals performing single vortex imaging in a planar JJ and using the optical tweezers technique to move the vortex and studying the transport response. The second part deals with optically heating a constriction in a SQUID to observe modulation of the transport due local heating.

Following this, we present some conclusions and perspectives of this work. We present some initial results in the foray of magneto-optical imaging of single vortices in YBCO, which is promising for future work extending our catalogue of optical methods to high-T_c systems. At this juncture all the techniques and methodologies have been developed to pursue a detailed and diverse study on optically driven Josephson transport, with the new possibility of applications in HTS devices.

Chapter 1

Superconductivity Phenomena

Introduction

Pure superconductivity is characterised by two physical properties of zero electrical resistance and perfect diamagnetism (that is complete expulsion of an external magnetic field from the bulk) below a critical temperature (T_c). This unique combination of properties characterises superconductivity as a distinct phase of matter.

The discovery of the superconducting transition in 1911 by Kamerlingh Onnes at Leiden University was part of a larger quest to reach lower temperatures, and explore the behaviour of matter at these temperatures. Passing current through the mercury sample as the temperature was lowered, the resistance abruptly vanished at 4.19 K, shown in this historical plot in Fig. 1.1. Exploiting this behaviour, he showed that a persistent current initiated in a superconducting wire shows no noticeable loss, even after a year [1].

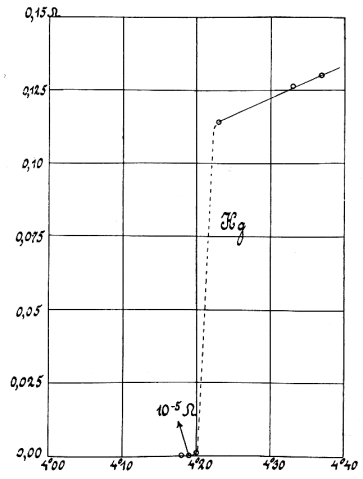

Figure 1.1: **Superconducting transition (1911).** Resistance versus temperature [K] for mercury (Hg). The resistance drops 4 orders of magnitude at a T_c of 4.19 K within 0.04 K.

Later in 1933, while measuring the magnetic field distribution outside of superconducting samples, Walther Meißner and Robert Ochsenfeld found that a superconducting sample cooled below its T_c will expel all internal fields. This was indirectly measured as the increase of external field due to the decrease of internal fields as flux is conserved. This added another facet of *superdiamagnetism* in defining the superconductive state.

The reconciliation of zero electrical resistance and superdiamagnetism is not straightforward, as the behaviour of a perfect conductor with infinite conductivity ($\sigma \to \infty$) does not exhibit the same behaviour in a field cooled scenario as a superconductor does. This is illustrated in further detail in Fig. 1.2. In part (a-c), taking a hypothetical perfect conductor which is cooled down in zero magnetic field or zero field cooled below the temperature at which the resistance becomes zero. Now when an external magnetic field is applied, surface screening currents are induced to

maintain the initial zero field within the material. When the applied field is removed, the field within the material stays at zero. However, when the perfect conductor is field cooled and then the applied field is removed , the perfect conductor creates currents to maintain the internal field, conserving the previous state (d-f). In contrast, a superconductor when cooled with or without a field, expels the internal flux (g-j). Surface currents are spontaneously produced to cancel the internal fields. Perfect conductors are flux conserving and not flux expelling. This distinction differentiates the state of perfect conductivity from superconductivity.

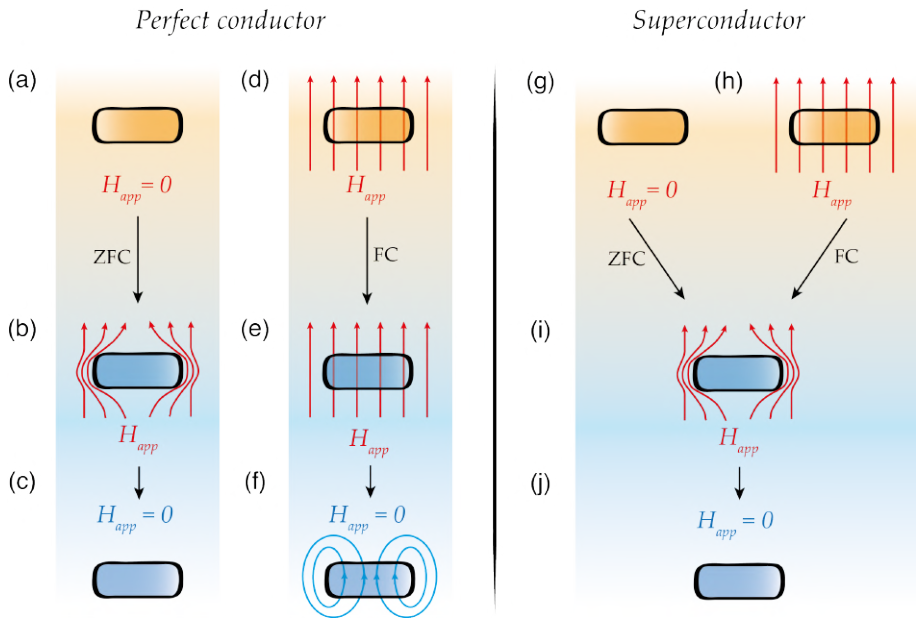

Figure 1.2: **Meißner effect.** Comparative response of a perfect conductor (**a-f**) and a superconductor (**g-j**) under an applied magnetic field with zero field cooled (ZFC) and field cooled (FC) conditions.

In the following sections, some important theoretical frameworks in superconductivity will be described including Londons' electrodynamical model, the thermodynamic model of phase transitions introduced by Ginzburg and Landau, and the microscopic theory of Bardeen, Cooper and Schrieffer. Following this, the chapter will delve into the physics of Abrikosov vortices and the Josephson effect, two very important consequences of macroscopic quantum behaviour of superconductivity. The chapter is intended to provide a cohesive and concise survey of superconducting physics while providing insight on relevant concepts pertaining to the work produced here.

1.1 London Equations

The London equations are a set of electrodynamical equations that form constitutive relations for a superconductor, relating the superconducting current to the electromagnetic fields inside and around the superconductor. These equations are analogous to Ohm's law ($\mathbf{J} = \sigma_0 \mathbf{E}$) which is the constitutive relation for a normal conductor. An important aspect of these equations is their consistency with the Meißner effect, providing a framework which combines perfect conduction and flux expulsion [2].

1.1.1 First London Equation

A superconductor provides a true lossless state of perfect conductivity. However, it is not as simple as inserting the condition $\sigma_0 \to 0$ into $\mathbf{J} = \sigma_0 \mathbf{E}$ and invoking perfect conductivity. A new relation is required to describe conductivity under the superconductivity paradigm. In the classical model the motion of electrons are subject to external electromagnetic fields (f_{em}) and opposing drag forces (f_{drag}). We can impose perfect conductivity by setting the mean free path $l \to \infty$, effectively eliminating drag forces. The equation of motion can be written as follows

$$m^* \frac{d\mathbf{v}}{dt} = q\mathbf{E}$$
$$\mathbf{J}_s = n^* q^* \mathbf{v} \tag{1.1}$$

Here $\mathbf{J}_s$ is the supercurrent density, and m^*, n^* and q^* are the mass, number density and charge for the *superelectron* carrier, respectively. Differentiating $\mathbf{J}_s$ with respect to time leads to a new constitutive relation analogous to Ohm's law and this is referred to as the first London equation.

$$\boxed{\frac{\partial}{\partial t}(\mathbf{J}_s) = \frac{1}{\Lambda}\mathbf{E}} \tag{1.2}$$

where $\Lambda \equiv \frac{m^*}{n^*(q^*)^2}$ is a phenomenological parameter. The equation describes perfect conductivity as the electric field accelerates the carriers rather than travelling at a sustained velocity dictated by the resistance or scattering events as described by Ohm's Law.

1.1.2 Second London Equation

Ideal diamagnetism in a superconductor can be deduced by exploring the existence of a magnetic field in a material described by the first London equation. Taking curl on both sides of Eq. 1.2 and using Faraday's law we obtain

$$\frac{\partial}{\partial t}(\nabla \times \mathbf{J}_s) = -\frac{1}{\Lambda}\frac{\partial \mathbf{B}}{\partial t} \tag{1.3}$$

This equation tells us that any change in the magnetic field $\mathbf{B}$ will be be screened immediately. However, static currents and magnetic fields also satisfy these equations as

would be the case for a perfect conductor. Therefore to address this inconsistency, it was proposed to restrict the solutions for superconductors to fields and currents that satisfy the following equation. Integrating both sides leads to the second London equation

$$(\nabla \times \mathbf{J}_s) = -\frac{1}{\Lambda}\mathbf{B} \tag{1.4}$$

This equation states that an external field applied to a superconductor will induce an equal and opposite field, in line with the Meißner effect.

1.1.3 London penetration depth, λ_L

Exploring further the behaviour of a magnetic field inside a superconductor, assuming **B** and **E** are time-independent, we take the differential form of Ampere's circuital law $\nabla \times \mathbf{B} = \mu_0 \mathbf{J}_s$, and take curl on both sides

$$\nabla \times (\nabla \times \mathbf{B}) = \mu_0 \nabla \times \mathbf{J}_s \tag{1.5}$$

Using the vectorial identity $\nabla \times (\nabla \times \mathbf{B}) = \nabla(\nabla \cdot \mathbf{B}) - \nabla^2 \mathbf{B}$, where $\nabla \cdot \mathbf{B} = 0$, along with the second London equation we get

$$\nabla^2 \mathbf{B} = \frac{\mu_0}{\Lambda}\mathbf{B} = \frac{1}{\lambda_L^2}\mathbf{B} \tag{1.6}$$

This equation accounts for the Meißner effect because it does not allow a spatially uniform solution, so a magnetic field cannot exist in a superconductor. That is to say, $\mathbf{B}(\mathbf{r}) = \mathbf{B}_0 = \text{const.}$ is not a solution unless $\mathbf{B}_0 = 0$. Therefore, in the pure superconducting state the only field allowed is exponentially damped as we move in from the external surface. We find a new characteristic length known as the London penetration depth given by

$$\lambda_L = \sqrt{\frac{m^*}{n_s q^{*2} \mu_0}} \tag{1.7}$$

The penetration depth has an empirical temperature dependence [3]

$$\lambda_L(T) \approx \frac{\lambda_L(0)}{\sqrt{1 - \left(\frac{T}{T_c}\right)^4}} \tag{1.8}$$

This can be qualitatively understood by taking the total density of carriers $n = n_s + n_n$, as a sum of the superelectrons and normal electrons below T_c. At $T = 0$, the total carrier density is $n = n_s$. With rising temperature $T \to T_c$ and $n_s \to 0$, the penetration depth grows indefinitely and there is complete penetration of magnetic field into the material [4]. This is known as the *two-fluid temperature dependence*, a model conceived by Gorter and Casimir [5] which interpreted the thermodynamics of superconductors in terms of coexisting normal and superconducting fluids. This temperature scaling is prevalent for other facets of superconductive behaviour.

1.2 Ginsburg-Landau Theory

While the London equations provide an electrodynamical framework for understanding key aspects of superconductivity, effects of external fields or temperature on the superconducting condensate was uncharted at the time Ginzburg and Landau (GL) proposed their phenomenological model for superconductivity [6]. The model uses Landau's general mean-field theory of continuous phase transitions (i.e., second-order) [7] for charged fluids to describe the macroscopic properties of the superconductor in the vicinity of the phase transition point (i.e., critical temperature, T_c).

1.2.1 Ginzburg-Landau Equations

Landau introduced the concept of *order parameter*, which is a thermodynamic variable that goes from zero to one across a phase transition. In a superconductor a single-valued macroscopic wavefunction describes the superelectron condensate:

$$\Psi(\mathbf{r}) = \psi(\mathbf{r})\, e^{i\theta(\mathbf{r})} \tag{1.9}$$

where $\psi(\mathbf{r})$ is the complex amplitude and $\theta(\mathbf{r})$ is the phase. The normalisation condition $|\Psi(\mathbf{r})|^2 = n_s$ yields the superelectron density. The phase θ plays an imperative role in determining the the supercurrent density and will be elucidated upon in the follow sections.

The thermodynamic potential or free energy can be written as a function of the order parameter (Ψ) and relevant thermodynamic properties like temperature, magnetic field, etc. Hence, we write the free energy as $F = F(\Psi, T)$, where the equilibrium state at temperature T minimises the free energy. Since the form of F is not explicitly known, Landau proposed that the free energy can be Taylor expanded around T_c in terms of Ψ by considering that the order parameter is small. Only terms allowed by the symmetries of the system and the differentiability (continuity) of the order parameter at T_c are retained. Then the free energy is given by:

$$F_s(\Psi, T) = F_n(T) + \alpha(T)|\Psi|^2 + \frac{\beta(T)}{2}|\Psi|^4 \tag{1.10}$$

where F_n denotes the free energy in the normal state. Although $\alpha \geq 0$ is mathematically valid, this limit gives a single maximum for $F(\psi = 0)$ which means the equilibrium state has $n_s = 0$. This describes a normal state. Therefore in the case of superconductors $\alpha = \alpha_0(T - T_c)$ is negative, and α_0 and β are positive constants all below T_c. With these considerations, the local extrema in F_s are given by two solutions for the order parameter below T_c

$$|\Psi| = 0 \qquad \text{and} \qquad |\Psi| = \sqrt{\frac{\alpha_0}{\beta}}\sqrt{T - T_c}$$

The first solution corresponds to a maxima and the normal state where the order parameter is null, while the second corresponds to minimas and the state determined by the coefficients α and β below T_c.

Thus far we have treated the system as a spatially homogeneous neutral superfluid, all within the framework of Landau's mean-field theory. To account for spatially nonuniform conditions, a gradient term associated with the quantum mechanical kinetic energy is introduced, $\frac{\hbar^2}{2m^*}|\nabla\Psi|^2$. If we consider $\Psi(\mathbf{r})$ as a discretised wave function where each discrete step has some value for the wavefunction, spatial variations between steps will have an associated free energy cost. The prefactor $(\frac{\hbar^2}{2m^*})$ is referred to as the "stiffness" as it controls the material's ability to fluctuate. In addition to that, to consider the case of a charged superfluid such as a superconducting condensate, a term for the quantum mechanical interaction of the magnetic field and kinetic energy is included, $q^*\mathbf{A}$. Here the magnetic vector potential $\mathbf{A}$ obeys $\mathbf{B} = \boldsymbol{\nabla} \times \mathbf{A}$. The contributions from an applied magnetic field ($\mathbf{H}_{app}$) and the subsequent screening currents ($\mathbf{B}_{scr}$) can also be included. With these considerations, the free-energy functional over all space is written as:

$$\begin{aligned} F_{GL} &= F_s(\psi, T) - F_n(T) \\ &= \int d^3r \left[\alpha(T)|\Psi|^2 + \frac{\beta}{2}|\Psi|^4 + \frac{1}{2m^*}|(-i\hbar\nabla - q^*\mathbf{A})\Psi|^2 \quad \cdots \right. \\ &\qquad \left. \cdots + \frac{\mu_0|\mathbf{H}_{app}|^2}{2} + \frac{|\mathbf{B}_{scr}|^2}{2\mu_0}\right] \end{aligned} \tag{1.11}$$

Minimising this free-energy functional with respect to ψ leads to a differential equation which is known as the first Ginzbug-Landau equation.

$$\alpha(T)|\Psi| + \beta|\Psi|^2\psi + \frac{1}{2m^*}(-i\hbar\nabla - q^*\mathbf{A})^2\Psi = 0 \tag{1.12}$$

where m^* and q^* are still the mass and charge for the superelectron carrier, respectively.

The functional in Eq. 1.11 can also be minimised with respect to the magnetic vector potential $\mathbf{A}$ to obtain an expression for the supercurrent density $\mathbf{J}$. Using Gauss' law ($\nabla\cdot\mathbf{B} = 0$) and the previously defined relation $\mathbf{B} = \boldsymbol{\nabla}\times\mathbf{A}$, Ampère's law ($\boldsymbol{\nabla}\times\mathbf{B} = \mu_0\mathbf{J}_s$) can be used to obtain $\mu_0\mathbf{J} = -\nabla^2\mathbf{A}$. Minimisation of the free energy as a function of $\mathbf{A}$ leads to the second Ginzburg-Landau equation or the supercurrent equation.

$$\mathbf{J}_s = \frac{q^*}{2m^*}[\Psi^*(-i\hbar\nabla - q^*\mathbf{A})\Psi + \text{c.c}] \tag{1.13}$$

This equation describes the probabilistic flow of a bosonic particle. Expansion of the equation with the complex conjugate terms leads to a simplified expression where the supercurrent is a function of the gradient of the superconducting phase θ and the superelectron density n_s.

$$\begin{aligned} \mathbf{J}_s &= \frac{-iq^*\hbar}{2m^*}(\Psi^*\nabla\Psi - \Psi\nabla\Psi^*) - \frac{q^{*2}}{m^*}\mathbf{A}|\Psi|^2 \\ &= \frac{q^*n_s\hbar}{m^*}\left(\nabla\theta - \frac{2\pi}{\Phi_0}\mathbf{A}\right) \end{aligned} \tag{1.14}$$

In the limit of uniform $\Psi(\mathbf{r})$ or negligible phase variation ($\nabla\theta$), the expression simplifies to the first London equation (Eq. 1.2)

$$\mathbf{J}_s = \frac{q^{*2} n_s}{m^*}\mathbf{A} \tag{1.15}$$

1.2.2 Coherence length, ξ_c

Under the paradigm of Ginzburg-Landau theory, it is possible to show that in the presence of a perturbation, a spatial variation in superfluid density occurs gradually over a characteristic length scale. The first Ginzburg-Landau equation can be applied in one-dimension without an applied field to find the variation of $\psi(x)$ near the surface of a superfluid filling the half space $x > 0$, where the boundary condition $\psi(x = 0) = 0$ is imposed.

$$-\frac{\hbar^2}{2m^*}\Psi(x)'' + \alpha(T)|\Psi(x)| + \beta|\Psi(x)|^2\Psi(x) = 0 \tag{1.16}$$

Applying a substitution,

$$f(x) = \Psi(x)/\Psi_\infty(x)$$
$$\psi_\infty(x) = \lim_{x\to\infty}\Psi(x) = \sqrt{-\alpha(T)/\beta}$$

we obtain

$$-\frac{\hbar^2}{2m^*\alpha(T)}f''(x) + f(x) - f(x)^3 = 0 \tag{1.17}$$

Since we want to examine the order parameter for the case $T \approx T_c$, where variation is small, we can neglect higher order terms and retain terms linear in Ψ as follows

$$f''(x) = \frac{1}{\xi^2}f(x) \tag{1.18}$$

This equation contains a characteristic length scale, $\xi_c > 0$, known as the *Ginzburg-Landau* coherence length

$$\xi_c^2 = -\frac{\hbar^2}{2m^*\alpha(T)} \cong \frac{\hbar^2}{2m^*\alpha_0(Tc - T)} \tag{1.19}$$

The coherence length is a length scale over which the order parameter fluctuate without undue energetic costs. In application this is the distance over which the superconducting order decays near a non-superconducting interface. It is also clear that this parameter shows a strong dependence on temperature similar to Eq. 1.8.

$$\xi(T) \approx \frac{\xi(0)}{\sqrt{1 - \frac{T}{T_c}}} \tag{1.20}$$

where $\xi(0)$ is the coherence length at $T = 0$.

1.2.3 Type-II superconductivity

Up to this point, the formulaic framework that has been developed to explain the superconductivity phenomena has described superconductors of the class *Type*-I. This class is described by strict adherence to the diamagnetic condition where under an applied magnetic field, resistanceless surface currents circulate to nullify the external flux. As the applied field increases, the counter acting currents also increase until a critical magnetic field $H_c(T)$ and a corresponding *critical current density* $\mathbf{J}_c$ is reached by the shielding current where superconductivity breaks.

In contrast, a material of the class *Type*-II exhibits an intermediate or mixed state where the diamagnetism relaxes. For applied field strengths less than the lower critical field, $H_{c1}(T)$, the superconductor will exhibit the Meißner effect. Applied fields greater than the *upper critical field*, $H_{c2}(T)$, will destroy superconductivity. However, for the range $H_{c1}(T) \leq H \leq H_{c2}(T)$, the superconductor is in a mixed state where there is partial penetration of magnetic flux into the interior volume of the material. These states are illustrated in the phase diagram in Fig. 1.3b.

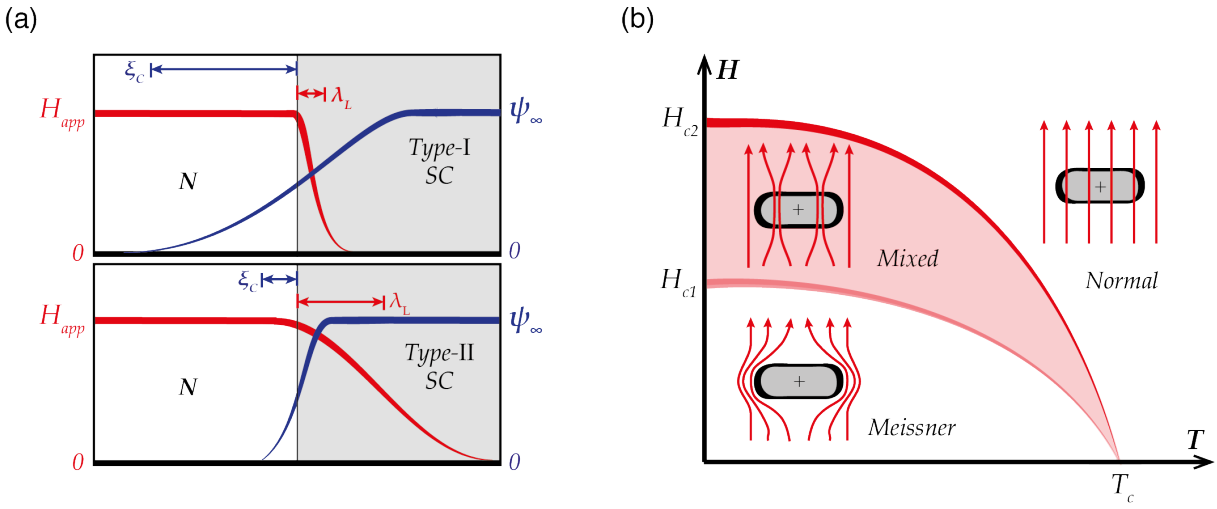

Figure 1.3: **Type-II superconductivity.** **(a)** Variations in relative length scales of the penetration depth and coherence length for type-*I* and type-*II* superconductor. **(b)** Phase diagram for type-*II* superconductor showing the lower (H_{c1}) and upper (H_{c2}) critical field. Below H_{c1} the material is superconductive. Between H_{c1} and H_{c2} a mixed state appears. Above H_{c2} the material behaves as a normal conductor.

The criterion to classify a material as either *type*-I or *type*-II is explained through free energy considerations. Taking a sample in an applied magnetic field where there is a distinct interface between a superconductor and normal region (Fig. 1.3a), the net surface energy per unit length at the interface is given by [8]:

$$\sigma = \frac{1}{2}\mu_0 H_{app}^2 \pi[\xi_c^2(T) - \lambda_L^2(T)] \tag{1.21}$$

Then according to Eq. 1.21, surface penetration of the magnetic field over a distance $\lambda_L(T)$ provides a negative contribution to the free surface energy at the interface. Additionally, $\psi \to 0$ over a distance $\xi_c(T)$ effectively decreasing the superconducting volume

and providing a positive contribution to surface energy. It is the case that in *type*-I superconductors $\xi_c(T) > \lambda_L(T)$, while in *type*-II superconductors $\lambda_L(T) > \xi_c(T)$ (Fig. 1.3a).

It is clear that *type*-I superconductors have positive surface-energy and prevalence of normal-superconducting interfaces increases the total free energy making it energetically unfavourable. On the other hand, *type*-II superconductors have negative surface-energy and total energy is minimised by introducing more interfaces. These normal regions can take form of lamina of very small thickness $\sim \xi$ or of filaments of size $\sim \xi_c$. The Ginzburg-Landau parameter κ gives a distinct condition that distinguishes the two classes of superconductors.

$$\kappa \equiv \lambda_L(T)/\xi_c(T) \tag{1.22}$$

It is shown that the sign of the surface energy changes at $\kappa = 1/\sqrt{2}$ [9]. *Type*-I superconductors are characterised by $\kappa < 1/\sqrt{2}$, while *type*-II superconductors are distinguished by $\kappa > 1/\sqrt{2}$. In the case of the high-T_c superconductors $\kappa \gg 1/\sqrt{2}$. The more complex anisotropic crystal structure brings with it large penetration depths and short coherence lengths, putting the condition for κ at the so-called London limit.

1.3 Microscopic Theory

While the London equations and the theory of Ginzburg and Landau worked well to explain the phenomenological observations of superconductive behaviour, a lack of understanding of the microscopic nature of superconductivity proved perplexing for the community at that time. In 1957, Bardeen, Cooper and Schrieffer proposed a microscopic theory, aptly called the BCS theory, of superconductivity which bridged this gap and was able to provide a full picture of this macroscopic quantum phenomena [10].

An appropriate starting point is by considering particles described by Fermi-Dirac and Bose-Einstein statistics, namely *fermions* and *bosons*, respectively. The distinguishing characteristic of these two kinds of particles is the intrinsic property of spin. Fermions like electrons, protons and neutrons possess half-integral spin, while bosons like photons and phonons possess integral spin. Fermions confined to a potential will repulse each other as per the *Pauli exclusion principle*, so only two fermionic particles with opposite spins are allowed to occupy one energy state. While in the case of bosons, several bosons can occupy the same energy state. At a temperature of absolute zero the energy distribution of fermions allows a sequential packing from the lowest energy state one by one, but in the case of bosons an infinite number of bosons can be packed into the lowest energy state. This is schematically illustrated in Fig. 1.4a.

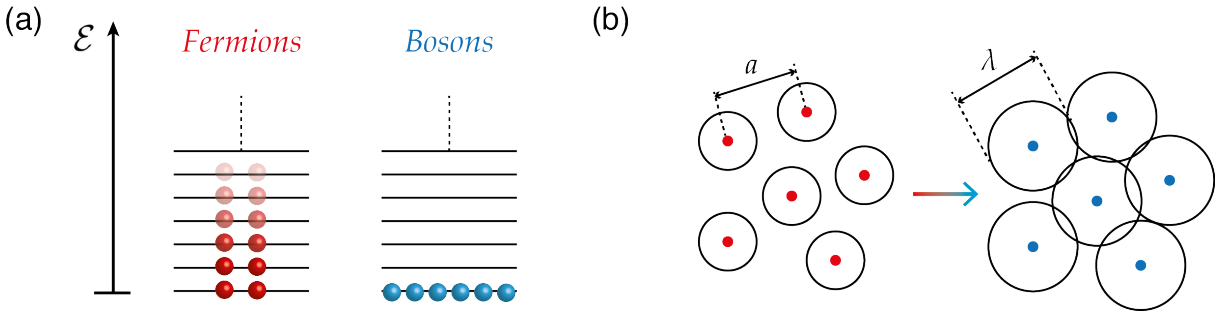

Figure 1.4: **Fermions and bosons.** (**a**) Distribution of fermions and bosons in the discrete energy levels at the temperature of absolute zero. Fermions pack one by one from the lowest to the highest energy level, while bosons are simultaneously packed in the lowest energy level. (**b**) Overlap of the wave functions of gas particles with decreasing temperature as *de Broglie wavelength* (λ_{dBl}) starts to equal the particle spacing (a).

Consider the average distance between gas particles is a and the *thermal de Broglie wavelength* of the gas particle is given by

$$\lambda = \frac{h}{\sqrt{2\pi m k_B T}} \tag{1.23}$$

where k_B is the Boltzmann's constant, m is the mass of the gas particle and T is the temperature of the gas. With decreasing temperature λ becomes longer and wave functions of the neighbouring particles begin to overlap as λ approaches the separation distance a, as shown in Fig. 1.4b. If these particles are bosons, they condense to the lower energy level. This is what is called a *Bose-Einstein condensate* (BEC). Particles occupying the

same energy level have overlapping wave functions with the same momentum and energy that are represented by a macroscopic wave function. Under the fermionic distribution of particles, the total energy of the system is high relative to that of a BEC system. However, if these fermions can somehow be converted to bosons, the total energy of the system could be lowered. This forms the essence of what is postulated in the BCS theory. Electron pairs or *Cooper pairs* come together to form boson like particles that condense when the temperature is decreased sufficiently below a critical temperature, thereby lowering the total energy of the system. This condensate of Cooper pairs is described by a macroscopic wave function or the order parameter (Eq. 1.9).

1.3.1 Cooper pair formation

In general electrons have a repulsive Coulombic interaction between them. It is imperative to overcome this repulsion energy in order to form an electron pair. This occurs in the form of phonon assisted electron pairing and it is schematically illustrated in Fig. 1.5.

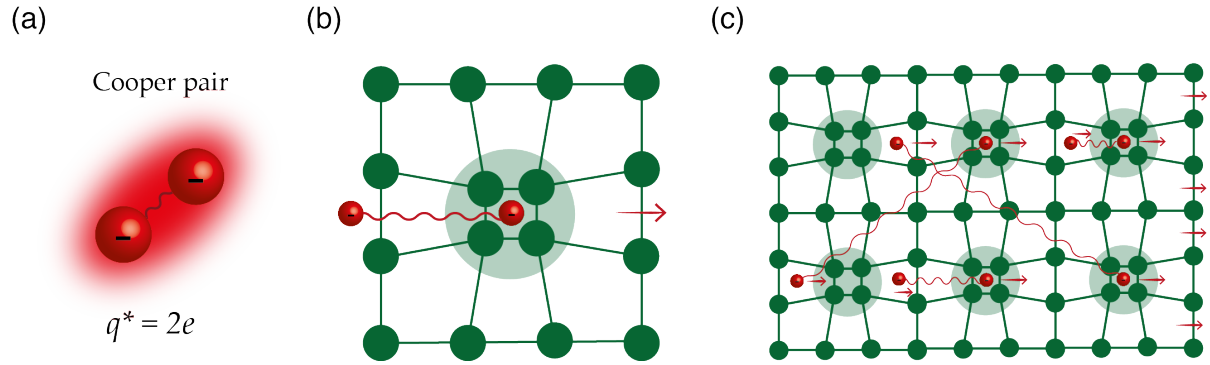

Figure 1.5: **Cooper pairs.** (**a**) A cooper pair comprises of two normal electrons that have a charge of $2e$. (**b**) The two electrons are phonon coupled due to lattice facilitated attractive forces between the electrons. (**c**) The phonon coupling manifests as a cohesive motion of all electrons to form a condensate of Cooper pairs.

The BCS theory assumes that there exists a medium generated attraction force that can overcome the Coulombic repulsion between electrons. A typical free electron travels through the lattice close to the Fermi surface with a velocity $v_F = \hbar k_F/m$. The moving electron attracts surrounding positive ions and they respond slowly, relative to v_F. The shortest response time of the lattice corresponds to the highest possible lattice vibration frequency, the *Debye frequency* ω_D. After a time τ the lattice reaches its maximum deformation creating a local region of positive charge. The initial electron is a distance $\sim v_F\tau$ away, when a secondary electron is attracted to the accumulated positive charge, without feeling the Coulombic repulsion of the initial electron. The net effect of the phonons is then creation of an attractive interaction which connects these electrons to form an antisymmetric spin singlet pairing where the spatial part of the wavefunction is symmetric and nodeless, taking advantage of the attractive interaction. The pairing tends to happen in a zero center of mass state so the two electrons can chase each other unhindered around the lattice. This cohesive motion of Cooper pairs throughout the lattice translates to the macroscopically observed supercurrent.

1.3.2 BCS ground state

Following this heuristic explanation of Cooper pair formation, this interaction has deeper consequences. The phonon mediated binding of two normal electrons to form a Cooper pair results in a lowering of their energy. It can be thought of as two conduction electrons lying above the Fermi surface being inserted into the Fermi sphere. It was then postulated that electrons within the Fermi sphere should also be able to couple themselves via lattice vibrations to lower their energy. However, only a fraction of electrons that lie within a shell thickness of $\mathcal{E}_F \pm \hbar\omega_D$ around the Fermi sphere can be paired, since the highest possible phonon energy is $\hbar\omega_D$. The binding energy is strongest for an antisymmetric spin singlet state, occupying the same quantum state behaving as Bose particles.

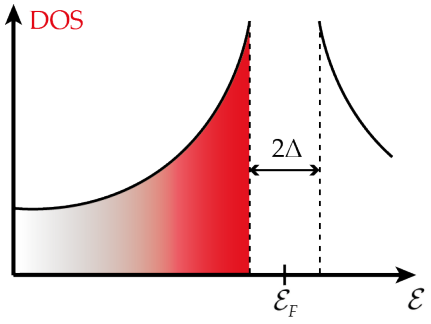

Figure 1.6: **Superconducting energy gap.** Density of states for a superconductor with an energy gap 2Δ separating the ground (paired) and excited (unpaired) state around the Fermi energy $\mathcal{E}_F$.

Since Cooper pairs have lower energy than normal electrons and have a binding energy 2Δ, it follows that there is an energy gap within the density of states that separates the condensed ground state from the excited or unpaired state, shown in Fig. 1.6. The gap straddles the Fermi energy level stabilising the Cooper pairs against breaking apart. Unlike the band gap found in semiconductor systems, the superconducting energy gap is a function of temperature. For temperatures approaching absolute zero the energy gap follows the relation

$$\Delta(0) \approx 1.76 k_B T_c \tag{1.24}$$

where k_B is Boltzmann's constant. While for temperatures $T \approx T_c$, the gap is shown to follow

$$\Delta(T \approx T_c) \approx 1.74\Delta(0)\sqrt{1 - \frac{T}{T_c}} \tag{1.25}$$

1.4 Flux Quantisation

With a microscopic understanding of the superconductivity phenomena, the implications of the phase, $\theta(\mathbf{r})$, in the single-valued macroscopic wavefunction describing the quantum state of the superconducting condensate, $\Psi(\mathbf{r}) = \psi(\mathbf{r})\, e^{i\theta(\mathbf{r})}$, can be examined.

In a superconducting ring, a supercurrent is generated using magnetic induction (H_{app}) as illustrated in Fig. 1.7. The supercurrent should be stable given there is zero dc resistance within the superconductor, creating a stationary state. In principle, arbitrary supercurrents can be generated using this method, however, the quantum mechanical nature of the system should be considered to revise this expectation. The stationary states for electrons are determined by the quantisation condition for orbital angular momentum. This is equivalent to the requirement of a periodic boundary condition.

In the context of the superconducting ring, a stationary state for the supercurrent along the ring can only exist if the single-valued macroscopic wavefunction describing the ensemble of Cooper pairs does not interfere destructively. When a complete turn of the ring is reached, the phase needs to be continuous as shown in Fig. 1.7. In the presence of an external magnetic flux threading the ring, the flux modifies the phase along the ring.

In order for the phase to be continuous and return to its initial value after a complete turn, only certain values of magnetic flux are allowed to go through the ring. This supposition was first proposed by Fritz London and he concluded that the magnetic flux enclosed by a superconducting ring can only have discrete values which are multiples of a flux quantum [11]. He suggested the value of $\Phi_0^L = h/e$, deriving this value assuming single electrons were the supercurrent carriers. With the role of Cooper pairs revealed in BCS theory, the expression for the flux quantum was corrected to $\Phi_0 = h/2e$, accounting for the electron pair.

Using the macroscopic quantum model of superconductivity the quantisation condition can be derived [12]. Assuming a simple homogeneous isotropic superconductor, the supercurrent around a closed path C, similar to the ring, is found by integrating the expression (Eq. 1.13) for the supercurrent density along this contour.

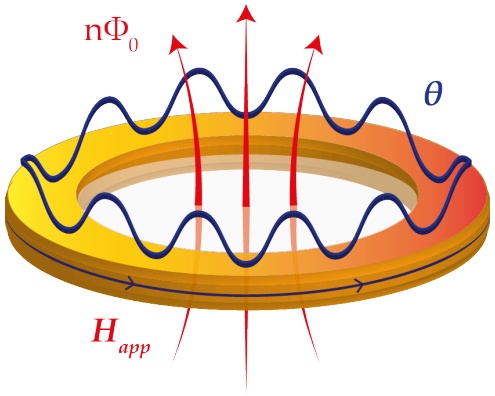

Figure 1.7: **Superconducting ring.** Illustration representing a stationary supercurrent state in a superconducting ring. An applied field (H_{app}) modifies the phase (θ) within the superconducting condensate, but the phase continuity imposes a self-regulation where only flux in steps of $n\Phi_0$ is allowed to thread the ring.

$$\Lambda \mathbf{J}_s = -\mathbf{A} + \frac{h}{q*}\nabla\theta$$

$$\oint_C (\Lambda \mathbf{J}_s)\cdot d\mathbf{l} + \int_S \mathbf{B}\cdot d\mathbf{s} = \frac{h}{q*}\oint_C \nabla\theta \cdot d\mathbf{l} \tag{1.26}$$

While there exists the trivial solution of zero for a closed path integral, however, since there is no defined value for the phase, integer values of n for the expression $\theta_n = \theta_0 + 2\pi n$ are also possible solutions giving the same value for

$$\Psi(\mathbf{r}) = \sqrt{n_s^*}\, e^{i(\theta_0 + 2\pi n)}$$

The phase is specified only within $|2\pi|$ of its principle value θ_0 within a range $[-\pi, \pi]$. The integral on the right hand side (Eq. 1.26) is then simplified to $2\pi n$, giving the quantisation condition:

$$\oint_C (\Lambda \mathbf{J}_s) \cdot d\mathbf{l} + \int_S \mathbf{B} \cdot d\mathbf{s} = n\Phi_0 \tag{1.27}$$

where Φ_0 is the magnetic flux quantum and is officially defined as

$$\Phi_0 \equiv \frac{h}{q^*} = \frac{h}{2e} = 2.067\,833\,636(81) \times 10^{-15}\ T \cdot m^2 \tag{1.28}$$

The left hand side of Eq. 1.27 is denoted as the *fluxoid* and the complete equation is a statement of *fluxoid quantisation*. It included contributions from the applied field and the induced screening supercurrents. The applied magnetic field itself is not quantised, but the net flux threading the ring is modulated by the induced supercurrents to impose the quantisation condition.

1.4.1 Abrikosov vortex

Flux quantisation allows us to revisit the mixed state in *type*-II superconductors. The condition for the Ginzburg-Landau parameter for type-II superconductors, $\kappa > 1/\sqrt{2}$, was investigated mathematically by Abrikosov [13]. His calculations revealed that partial flux penetration occurs when the applied field falls between the lower and upper critical field, $H_{c1}(T) \leq H \leq H_{c2}(T)$. The flux penetration takes the form of stationary infinitesimal nucleation fields and these nuclei order themselves in a periodic lattice with the periodicity depending on the applied magnetic field. The flux at each of the nuclei is a universal constant defined by Φ_0. These came to

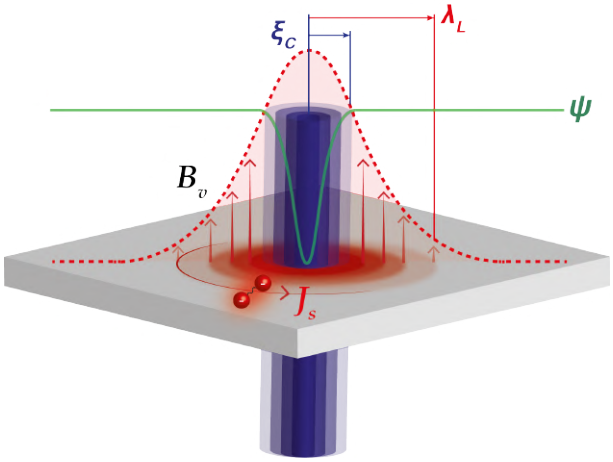

Figure 1.8: **Abrikosov vortex.** The smallest magnetic bit in *type*-II superconductors. The structure is modelled as a normal filament of radius ξ_c, with circulating supercurrent spreading a length λ_L into the superconductor, carrying a magnetic flux quantum Φ_0.

be known as *Abrikosov* vortices. This periodic ordering only occurs in pristine crystalline samples (i.e. ideal superconductors with no pinning potential).

A vortex is better visualised in Fig. 1.8 as a *normal* or non-superconducting filament in the interior of the superconductor, through which a flux quantum traverses. There is circulating screening supercurrent around the vortex which generates the quantum of flux, and spreads into the superconductor on the scale of the penetration depth λ_L. The radius of the vortex or the normal region is determined by the coherence length ξ. The coherence length and penetration depth are both material properties.

Flux can be trapped as vortices within the superconductor by two means: (i) The sample can be field-cooled (FC), with a magnetic field applied while the temperature of the superconductor is $T > T_c$ and then cooled below $T < T_c$, as shown in Fig. 1.2. The field can then be removed and the flux originally penetrating the sample will be trapped as vortices, with the vortex density dictated by $n_{vx} = H_{app}/\Phi_0$. (ii) Vortices can also form by the application of a magnetic field in the range of $H_{c1} < H_{app} < H_{c2}$, while $T < T_c$. Due to the Earth's magnetic field, vortices are often present in superconducting devices and contribute to noise in the system [14]. The relevant properties of the vortex will be further explored below including the magnetic field and supercurrent density, line energy of the vortex, the aforementioned lattice distribution, and pinning forces.

1.4.1.1 Magnetic field & current density

The properties of a vortex as a normal cylindrical core centred along the $\hat{z}$-axis, with a radius ξ_c in an infinite isotropic superconductor (Fig. 1.8) are derived within London theory,providing a practical understanding of vortex properties in the so-called London limit of $\kappa = \lambda_L/\xi_c \gg 1$. This implies that energy gain due to flux penetration dominates the energy cost due to loss of condensation energy, or the negative contribution to surface energy dominates the positive contribution (Eq. 1.21).

Inside the core ($r < \xi_c$), the constitutive relation for ohmic materials applies. In the superconducting region outside the core ($r \geq \xi_c$), the currents and fields are governed by the second London equation (Eq. 1.4), and in this region the magnetic flux density satisfies the Helmholtz equation. Assuming the vortex core is small and considering the order parameter recovers to 1 in a distance $\sim \xi_c$, it can be approximated by a delta function $\delta(\boldsymbol{r})$. Due to the cylindrical symmetry of the vortex centred along the $\hat{z}$-axis, the flux expression is expected to be $\mathbf{B} = B_z(r)\ \hat{\mathbf{z}}$, and we have a scalar Helmholtz equation.

$$\nabla^2 B_z - \frac{1}{\lambda^2} B_z = 0 \tag{1.29}$$

The solution to this equation is found by the technique of separation of variables into distinct modified Bessel function of r and θ [15] and leads to a solution: $\mathbf{B}(\mathbf{r}) = \frac{\Phi_0}{2\pi\lambda^2} K_0(r/\lambda_L)\hat{\mathbf{z}}$, where K_0 is the zeroth modified Bessel function. Qualitatively, $K_0(r/\lambda_L)$ decays as $\exp^{-r/\lambda_L}$ at large distances and diverges logarithmically with $\ln(\lambda_L/r)$ as $r \to 0$. In reality the cutoff is at $r \sim \xi_c$ as the order parameter tends to 0 moving into the center of the core. Then the solutions in the two regions is given by

$$\mathbf{B}(\mathbf{r}) \approx \begin{cases} \frac{\Phi_0}{2\pi\lambda_L^2}\sqrt{\frac{\pi}{2}\frac{r}{\lambda_L}}\exp[-r/\lambda_L]\,\hat{\mathbf{z}}, & \text{for } r \geq \lambda_L \\ \frac{\Phi_0}{2\pi\lambda_L^2}\left[\ln\frac{\lambda_L}{r} + 0.12\right]\,\hat{\mathbf{z}}, & \text{for } \xi_c < r < \lambda_L \end{cases} \tag{1.30}$$

and the supercurrent density associated with this flux is subsequently found using Ampère's law ($\nabla \times \mathbf{B} = \mu_0\mathbf{J}$):

$$\mathbf{J}_s(\mathbf{r}) \approx \begin{cases} \frac{\Phi_0}{2\pi\mu_0\lambda_L^3}K_1(\frac{r}{\lambda_L})\,\hat{\boldsymbol{\theta}}, & \text{for } r \geq \xi_c \\ 0, & \text{for } r < \xi_c \end{cases} \tag{1.31}$$

K_1 is the first order modified Bessel function.

The field distribution found in Eq. 1.30 corresponds to the field at the surface of the superconductor. To model the stray field above the surface, a rigorous solution for all field contributions has been calculated [16]. However, a more simplified treatment of the stray fields can be obtained by approximating the vortex as a magnetic monopole of charge $2\Phi_0$, centred at $r = 0$ and lying at z = z_0 = -1.27λ_L below the surface z=0. The scalar potential from a single vortex is given by:

$$\Phi_{vx}(r,z) = \frac{\Phi_0}{2\pi}\frac{1}{\sqrt{r^2 + (z - z_0)^2}} \tag{1.32}$$

The magnetic flux density B_{vx} from a single vortex is obtained by taking the gradient of the scalar potential $-\boldsymbol{\nabla}\Phi_{vx}(r,z)$, and is shown in Fig. 1.9.

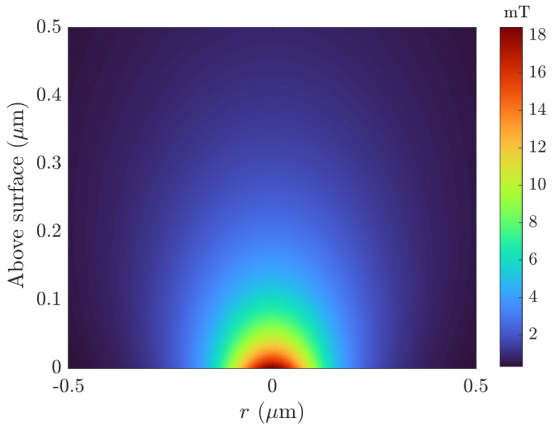

Figure 1.9: **Vortex magnetic flux density.** Flux distribution from a single vortex above the surface of the superconductor. The λ_L corresponds to 100 nm, the penetration depth of Nb. The flux decays rapidly above the surface of the superconductor.

1.4.1.2 Line energy

The energy per unit length of an isolated vortex corresponds closely to the lower critical field, within a multiplicative factor, in type-II superconductors. This is the energy cost to insert one flux quantum in the form of a vortex into the body of the superconductor, effectively transitioning from the Meißner state to the mixed state. It is given by the following integral

$$\epsilon_l = \frac{1}{2\mu_0}\int_0^\infty (B^2 + \lambda_L^2\mu_0^2 J^2)2\pi r dr \tag{1.33}$$

where the terms show explicit contributions from the magnetic field energy and kinetic energy due to supercurrent, respectively. In the London limit ($\lambda_L/\xi_c \gg 1$) energetic

contributions are dominated by the region $\xi_c \leq r \leq \lambda_L$, then the approximate value for vortex line energy is given by

$$\epsilon_l = \frac{\Phi_0^2}{4\pi\mu_0\lambda_L^2}\ln(\kappa) + \epsilon_c \tag{1.34}$$

where ϵ_c is the correction factor accounting for the condensation energy of the vortex core. The energy cost of vortex formation is dominated by the kinetic energy of Cooper pairs, while costs due to the magnetic field and loss of condensation at the core are relatively small in the London limit. The lower critical field is simply $H_{c1} = \epsilon_l/\Phi_0$.

1.4.1.3 Forces

There are several forces that a vortex can be subjected to, including but not limited to inter-vortex forces, Lorentz force, pinning force, and thermal force. A flowing supercurrent $\mathbf{J}_s$ can cause vortex motion as per $\mathbf{F}_L = \mathbf{J}_s \times \mathbf{\Phi}_0$, as shown in Fig. 1.11.

For vortices trapped in a pristine crystalline sample, cooled in a field larger than H_{c1} where the spacing between individual vortices approaches λ_L, the distribution of vortices tends to be influenced by vortex-vortex interaction [18]. Taking two vortices aligned along the $\hat{z}$ direction placed at positions $\mathbf{r}_1$ and $\mathbf{r}_2$. The magnetic field distribution (Eq. 1.4) is given as

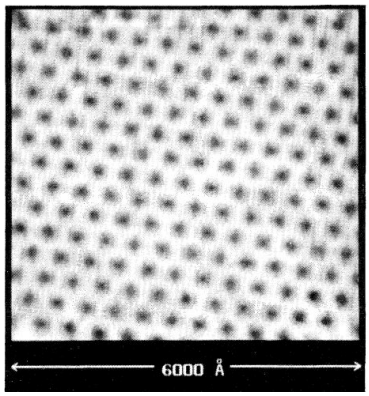

Figure 1.10: **AV lattice.** Scanning tunnelling image of AV lattice in $NbSe_2$. The vortex spacing in the triangular lattice is measured to be ~47.9 nm [17]

$$\nabla^2\mathbf{B} - \frac{\mathbf{B}}{\lambda^2} = -\frac{\Phi_0}{\lambda^2}\hat{z}[\mathbf{B}(\mathbf{r}-\mathbf{r}_1) + \mathbf{B}(\mathbf{r}-\mathbf{r}_2)] \tag{1.35}$$

The solution $\mathbf{B}(\mathbf{r})$ is a superposition of the fields of the individual vortices $\mathbf{B}(\mathbf{r}) = \mathbf{B}_{vx1} + \mathbf{B}_{vx2}$. Using Eq. 1.30 for $\mathbf{B}(\mathbf{r})$ we obtain an interaction energy per unit length of the two vortices

$$\epsilon_{int} = \frac{\Phi_0^2}{2\pi\mu_0\lambda_L^2}K_0\left(\frac{|\mathbf{r}_1 - \mathbf{r}_2|}{\lambda_L}\right) \tag{1.36}$$

This energy is repulsive and decreases as $(1/\sqrt{r_{12}}\exp^{-r_{12}/\lambda_L})$ at large distances and diverges as $\ln(|\lambda_L/r_{12}|)$ at short distances. The force exerted by vortex 1 on vortex 2 is given by taking the derivative of the interaction energy

$$\mathbf{f}_{vx,12} = -\nabla\epsilon_{int} = -\frac{\Phi_0}{\mu_0}\frac{\delta B_{v1}}{\delta r_{12}}\frac{\mathbf{r}_{12}}{r_{12}} = \Phi_0 J(r_1 - r_2)\frac{\mathbf{r}_{12}}{r_{12}} \tag{1.37}$$

This corresponds to the Lorentz force where one vortex's circulating current acts on the magnetic field of the other, and vice versa.

We can extend Eq. 1.35 to include interaction between N vortices as a superposition of their respective fields. The repulsive interaction energy can be minimised for a periodic arrangement of vortices. In this case the most favourable configuration is that of a triangular or square lattice. However, a triangular lattice is more commonly observed as it is more stable and generally has lower energy with a nearest neighbour separation distance of $a = \sqrt{\frac{2\Phi_0}{\sqrt{3}B}}$ with magnetic flux density B .

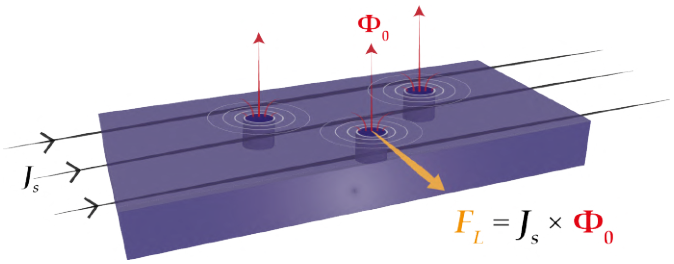

Figure 1.11: **Lorentz force.** Vortices driven by the Lorentz force $\mathbf{F}_L$, either via inter-vortex interaction, due to a applied supercurrent $\mathbf{J}_s$ or conversely by an applied magnetic field.

In real materials vortex motion is prevented due the phenomenon of *pinning*. This refers to sites that exert an attractive or *pinning* force, f_p, over the vortex lattice. These pinning centers can be defects like impurities, vacancies, dislocations or microholes. Pinning is directly related to the condensation energy of a vortex, the energy cost of creating a normal volume within the superconductor. The presence of the normal vortex core raises the free energy of the superconductor by the condensation energy of the core volume. The condensation energy is given by

$$\epsilon_c = \frac{1}{2}\mu_0 H_c^2 \pi \xi_c^2 L_z \tag{1.38}$$

where L_z is the length of the vortex line and H_c is the critical magnetic field $H_c = \frac{\Phi_0}{2\sqrt{2}\pi\mu_0\lambda_L\xi_c}$. The system can lower its energy by having the vortex in a normal region or where the condensation energy is already lost, rather than having to create a normal core. The effective length of the vortex is reduced resulting in a smaller loss in condensation energy, so it is favourable for the vortex to sit at the defect. Then the pinning force per unit length (f_p) of the vortex can be obtained by considering a normal region in close proximity to a vortex that has an attractive force which effectively minimizes the free energy difference to give [15]

$$|f_p| = \frac{\Phi_0^2}{32\pi\mu_0\lambda^2\xi} \tag{1.39}$$

In a Nb film the average pinning force per unit length of the vortex tends to be on the order of 10^{-8}-10^{-7} N/m. [19, 20]. In order to achieve vortex motion the applied force must be larger than the pinning force, $f_{app} > f_p$. There exists a depinning current density $\mathbf{J}_c$ that must be reached to observe any vortex motion, which in turn results in the appearance of finite resistance. The depinning can be achieved by applying a sufficiently large current where $F_L > f_p$, and is then given by $J_c = f_p/\Phi_0$.

A thermal force can also be used to move a single or an ensemble of vortices [21]. All superconductive properties are temperature dependent, even the line energy of a vortex grows linearly as $(T_c - T)$, as T is reduced below T_c. Therefore a temperature

gradient that can be created using a focused laser spot will generate a thermal force per unit length on the vortex such as [20, 22]

$$f_{th} \approx \frac{\Phi_0^2}{4\pi\mu_0\lambda_0^2} \ln\left(\frac{\lambda_0}{\xi_0}\right) \frac{\nabla T}{T_c} \tag{1.40}$$

where λ_0 and ξ_0 are the penetration depth and coherence length at zero temperature. The force will drive vortices towards the high temperature area, the sharper the gradient is the larger the force exerted. This mechanism is used as the basis of our optical tweezers technique which will be further elaborated upon in the Section 2.3.1.

1.5 Josephson effect

The Josephson effect is another important consequence of the macroscopic quantum coherent nature of the superconducting state. The effect can be observed when two superconductors ($S_{1/2}$) are weakly coupled to each other via a constriction. The constriction can be established either by conventional means with the use of tunneling barriers made from non-superconducting materials (insulator, ferromagnet or normal metal) (Fig. 1.12), or through the use of physical constrictions and contact points. The microbridge is an example of a weak link structure which locally weakens superconductivity to create an impedance in the structure via a physical constriction. These structures can be realised into various geometries [23]. The states of the superconducting condensate in the electrodes are described by their respective wave functions: $\psi_1(\theta_1)$ and $\psi_2(\theta_2)$. The coupling of these two states can be viewed as the overlap of these wave functions in the region of the barrier (Fig. 1.12).

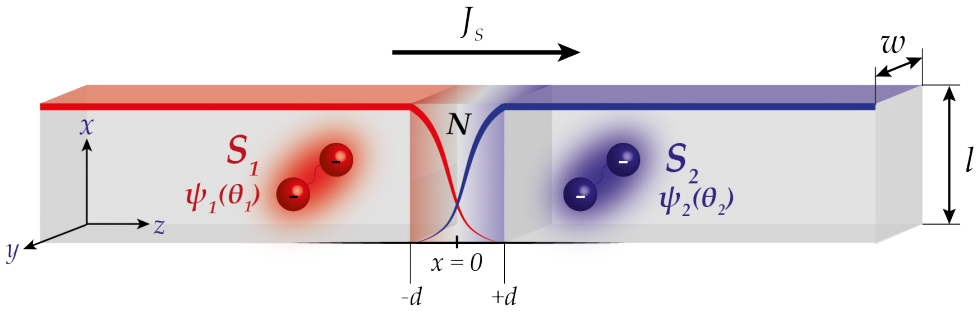

Figure 1.12: **Josephson junction.** **(a)** Schematic illustration of a conventional Josephson tunnel junction structure with two superconducting electrodes ($S_{1/2}$) coupled by a tunneling barrier. The supercurrent density (J_S) traverses the junction from S_1 to S_2. The coupling of the superconducting wave functions $\psi_{1/2}(\theta_{1/2})$ is shown as decay and overlap in the barrier region.

Conventional tunneling phenomenon dictates that electrons can tunnel across a sufficiently low barrier potential with the tunneling current density decaying exponentially with increasing barrier thickness. In the case of a superconductor junction, there are no normal electrons at the Fermi level at zero temperature, and we expect no tunneling current as long as the applied voltage is smaller than twice the energy gap voltage of Cooper pairs $2\Delta/e$. Once the Cooper pairs are broken, the normal electrons can tunnel through the barrier as usual. The tunneling probability of a single electron p_t decays exponentially with increasing barrier thickness, then the probability of a Cooper pair tunneling (two electrons) is more improbable. However, Brian Josephson proposed that the probability of a Cooper pair tunneling is indeed the same as that of a single electron because the tunneling of Cooper pairs is a coherent process, rather than considering this as two incoherent electron waves leaking through the barrier. It is the macroscopic wave function that describes the condensate of Cooper pairs which is tunneling through the barrier, a consequence of the macroscopic quantum nature of the superconducting state [24].

1.5.1 Josephson relations

Consider the tunnel junction shown in Fig. 1.12 where a current density ($\mathbf{J}_s$) is driven across the insulating barrier from region S_1 to S_2. The supercurrent density is described by the supercurrent equation Eq. 1.13. We need to find a relationship between the current density and the value of the phase of the wavefunction at each boundary ($x = \pm d$). To do so two simplifying assumptions are made: (1) the area (wl) is small such that the current density is considered uniform through this cross-section, and (2) there is no external magnetic potential ($\mathbf{A} = 0$).

The phase evolution across the junction can be analysed by considering the superconducting state wave functions or order parameters $\psi_1 = \sqrt{n_1}e^{i\theta_1}$ and $\psi_2 = \sqrt{n_2}e^{i\theta_2}$ in region S_1 and S_2, respectively. These represent the probability amplitudes of Cooper pairs on either side of the junction, and by applying the Schrodinger equation $i\hbar\,\partial\psi/\partial t = \mathcal{H}\psi$ to the amplitudes, the coupling of the electrode wave functions through the barrier can be extracted [25].

$$i\hbar\frac{\partial}{\partial t}\begin{bmatrix}\sqrt{n_1}e^{i\theta_1}\\ \sqrt{n_2}e^{i\theta_2}\end{bmatrix} = \begin{bmatrix}\mathcal{E} & \mathcal{K}\\ \mathcal{K} & -\mathcal{E}\end{bmatrix}\begin{bmatrix}\sqrt{n_1}e^{i\theta_1}\\ \sqrt{n_2}e^{i\theta_2}\end{bmatrix} \tag{1.41}$$

Here $\mathcal{K}$ represents the effect of the Cooper-pair coupling or transfer interaction across the barrier. It is a measure of the leakage of ψ_1 into the region of S_2, and vice versa for ψ_2 and S_1. For two isolated superconductor electrodes the energy terms $\mathcal{E}$ are given as $\mathcal{E}_{1/2} = 2\mu_{1/2}$ where $\mu_{1/2}$ are the respective chemical potentials.

Expanding the equations we obtain

$$\frac{\partial\psi_1}{\partial t} = -i\frac{\sqrt{n_1}}{2}e^{i\theta_1}\dot{n_1} + \psi_1\dot{\theta_1} = \frac{\mathcal{E}}{\hbar}\psi_1 + \frac{\mathcal{K}}{\hbar}\psi_2 \tag{1.42}$$

$$\frac{\partial\psi_2}{\partial t} = -i\frac{\sqrt{n_2}}{2}e^{i\theta_2}\dot{n_2} + \psi_2\dot{\theta_1} = -\frac{\mathcal{E}}{\hbar}\psi_2 + \frac{\mathcal{K}}{\hbar}\psi_1 \tag{1.43}$$

where $\dot{n} \equiv \partial n/\partial t$. Multiplying these expressions with their respective complex conjugates, Eq. 1.42 $\times\ \psi_1^*$ and Eq. 1.43 $\times\ \psi_2^*$ gives

$$\frac{-i}{2}\dot{n_1} + n_1\dot{\theta_1} = \frac{\mathcal{E}}{\hbar}n_1 + \frac{\mathcal{K}}{\hbar}\sqrt{n}e^{i\Delta\theta} \tag{1.44}$$

$$\frac{-i}{2}\dot{n_2} + n_2\dot{\theta_2} = -\frac{\mathcal{E}}{\hbar}n_2 + \frac{\mathcal{K}}{\hbar}\sqrt{n}e^{-i\Delta\theta} \tag{1.45}$$

Here $\sqrt{n} = \sqrt{n_1 n_2}$ and $\Delta\theta = \theta_2 - \theta_1$. Equating the real and imaginary parts of Eq. 1.44-1.45 leads to

$$\dot{n_1} = \frac{2}{\hbar}\mathcal{K}\sqrt{n}\sin\Delta\theta \tag{1.46}$$

$$\dot{n_2} = -\frac{2}{\hbar}\mathcal{K}\sqrt{n}\sin\Delta\theta \tag{1.47}$$

$$\dot{\theta_1} = \frac{\mathcal{K}}{\hbar}\sqrt{\frac{n_2}{n_1}} + \frac{\mathcal{E}}{\hbar}\cos\Delta\theta \tag{1.48}$$

$$\dot{\theta_2} = \frac{\mathcal{K}}{\hbar}\sqrt{\frac{n_1}{n_2}} - \frac{\mathcal{E}}{\hbar}\cos\Delta\theta \tag{1.49}$$

The Cooper pair current density **J** is given by

$$\mathbf{J}_s \equiv \dot{n_1} = -\dot{n_2} = \frac{2}{\hbar}\mathcal{K}\sqrt{n}\sin\Delta\theta \tag{1.50}$$

For identical superconductors $n_1 = n_2 = n_{1/2}$, the above relation is simplified to the first Josephson relation or the dc Josephson effect.

$$\boxed{J_s = J_c \sin(\Delta\theta)} \tag{1.51}$$

and J_c is the critical current density of the junction given by $2\mathcal{K}n_{1/2}/\hbar$. The critical current density pertains to the maximum supercurrent that can traverse through the junction before the breakdown of the superconductive state. The first Josephson relation tells us that the supercurrent density through a Josephson junction is sinusoidally varying with the phase difference $\theta_2 - \theta_1$ in the absence of any external potentials. This is also known as the ***current-phase relation*** (***CPR***).

The relationship between the voltage and phase of the supercurrent is derived by using Eq. 1.48 and 1.49 to take the time derivative of the phase difference. With a d.c. potential difference V across the junction, a Cooper pair experiences a potential difference of $-2eV$ as it traverses the barrier. For symmetry purposes the zero energy can be taken at the center of the barrier ($x = 0$) and the energy terms are $\pm\mathcal{E} = \pm eV$.

$$\frac{\partial(\Delta\theta)}{\partial t} = \dot{\theta_2} - \dot{\theta_1} = \frac{-2\mathcal{E}}{\hbar} = \frac{-2eV}{\hbar}$$

$$\boxed{V = \frac{\Phi_0}{2\pi}\frac{\partial(\Delta\theta)}{\partial t}} \tag{1.52}$$

yields the second Josephson equation or the ***voltage-phase relation***. Integrating this expression

$$\int \partial(\Delta\theta) = \int \frac{-2eV}{\hbar}\partial t \tag{1.53}$$

$$\Delta\theta(t) = \Delta\theta_0 + \frac{2\pi}{\Phi_0}V \cdot t \tag{1.54}$$

Inserting this equation into the current-phase relation reveals oscillations of the supercurrent at the Josephson frequency

$$\boxed{\frac{1}{\Phi_0} \simeq 483\,597.9\,\frac{GHz}{mV}} \tag{1.55}$$

The Josephson junction acts as a voltage controlled oscillator that is capable of generating very high frequencies. The Josephson frequency is the intrinsic value, independent of physical artifacts, which forms the basis for global voltage standards. The fundamental equations governing Josephson transport are the current-phase relation, the gauge-invariant phase relation, and the voltage-phase relation.

1.5.2 External magnetic field

By using a macroscopic quantum wave function to describe superconductivity, there inherently exist some interference effects. Spatial changes in the gauge-invariant phase gradient ($\nabla\theta$) due to an external magnetic field leads to interference of the wave functions, called the *Fraunhofer diffraction pattern*. The experimental observation of this pattern was important to prove the Josephson tunneling of Cooper pairs, and is essential to establish operation in the Josephson regime. This phenomenon is physically analogous to the *Aharonov-Bohm effect*, where a vector potential **A** affects the complex phase of a charged particle's wave function moving in an electric field, in an area where the magnetic field is zero. While in classical physics there is no observable effect of this, the shifted phase of the quantum particles is observed via an interference pattern. The equation describing the coupling of the vector potential to the phase is similar to the expression for the gauge-invariant phase gradient we derived earlier (Eq. 1.14) [26].

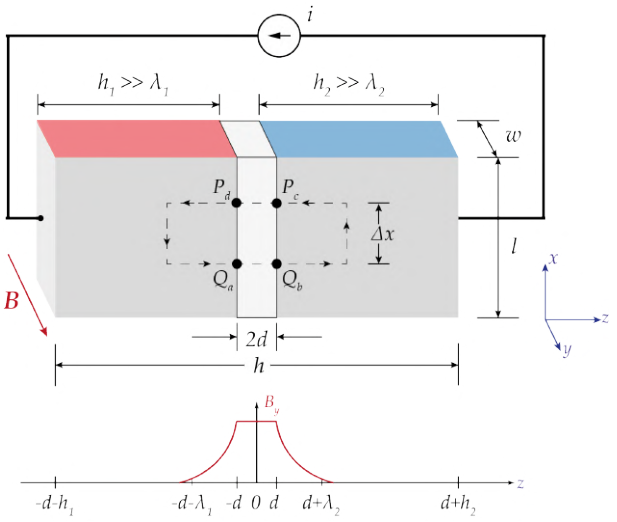

Figure 1.13: **Cross section of a Josephson junction.** The current flows in the x- direction, the magnetic field is applied in y- direction. The dashed line indicates the closed contour of integration. At the bottom, the decay of the magnetic field in the junction electrodes over the penetration depth is illustrated.

The gauge-invariant phase gradient ($\nabla\theta$) can be simplified to the gauge-invariant phase *difference* ($\Delta\theta$) by assuming the homogeneity of the current density across the cross-section of the barrier and in the electrodes. Then the gauge invariant phase difference is given by

$$\begin{aligned}\Delta\theta(\mathbf{r},t) &= \int_{-d}^{+d}\left(\nabla\theta(\mathbf{r},t) - \frac{2\pi}{\Phi_0}\mathbf{A}(\mathbf{r},t)\right)\cdot d\mathbf{l} \\ &= \theta_2(\mathbf{r},t) - \theta_1(\mathbf{r},t) - \frac{2\pi}{\Phi_0}\int_{-d}^{+d}\mathbf{A}(\mathbf{r},t)\cdot d\mathbf{l}\end{aligned} \tag{1.56}$$

with integration path $-d \rightarrow +d$ is taken across the insulation barrier from the $S_1 \mid N$ interface with phase θ_1 to the $N \mid S_2$ interface with phase θ_2.

A cross section schematic of a Josephson junction with the relevant dimensions is shown in Fig.1.13. The superconducting electrodes of length h_1 and h_2, are separated by an insulating barrier of width $2d$. The junction extends lengths w and l in the $y-$ and $x-$direction, respectively. In general, $w, l \gg 2d$, and $h_{1/2} \gg \lambda_{L1/2}$. The applied magnetic field is in the $y-$direction such that $\mathbf{B} = (0, B_y, 0)$ is a constant. The field must

penetrate the superconductor on the scale of the London penetration depth λ_L, so an effective magnetic thickness can be defined for the junction $t_B = 2d + \lambda_{L1} + \lambda_{L2}$.

Consider points $Q_{a/b}$ and $P_{c/d}$ shown in Fig. 1.13 that are separated by a infinitesimal distance Δx. The change $\Delta\theta(Q) - \Delta\theta(P)$ of the gauge-invariant phase difference can be determined by taking the line integral along the contour shown in the figure. The phase evolution around the contour is found by integrating $\Delta\theta$ Eq. 1.56, around the closed contour where the phase change must be an integer n multiple of 2π.

$$\begin{aligned}\oint_C \Delta\theta \cdot d\mathbf{l} &= 2\pi n \\ &= (\theta_{Qb} - \theta_{Qa}) + (\theta_{Pc} - \theta_{Qb}) + (\theta_{Pd} - \theta_{Pc}) + (\theta_{Qa} - \theta_{Pd}) + 2\pi n\end{aligned} \tag{1.57}$$

The first and third term in the equation above concern the phase difference across the junction, dictated by the gauge invariant phase difference. The second and fourth terms concern the phase difference inside the superconducting material dictated by the supercurrent equation Eq. 1.13. Explicitly substituting these expressions into Eq. 1.57 gives

$$\Delta\theta(Q) - \Delta\theta(P) = -\frac{2\pi}{\Phi_0}\left[\oint_C \mathbf{A} \cdot d\mathbf{l} + \int_{Qb}^{Pc} \Lambda \mathbf{J}_s \cdot d\mathbf{l} + \int_{Pd}^{Qa} \Lambda \mathbf{J}_s \cdot d\mathbf{l}\right] \tag{1.58}$$

The first integral term denotes the total enclosed flux within the loop, Φ. The latter two terms concern the supercurrent density around the loop excluding the junctions, and can be neglected when the superconducting material of the electrode arms are thicker than λ_L so the current density induced by the applied field is exponentially small. Then the contour can be taken deep inside the electrodes where $\mathbf{J}_s$ is zero. The phase difference simplifies to

$$\Delta\theta(Q) - \Delta\theta(P) = \frac{2\pi\Phi}{\Phi_0} \tag{1.59}$$

It is clear that the change $\Delta\theta(Q) - \Delta\theta(P)$ in the gauge invariant phase difference is given by the magnetic flux Φ/Φ_0 threading the junction within the contour. The total flux enclosed in the contour is given by $\Phi = B_y t_b \Delta x$, since magnetic fields decay exponentially into each of the superconducting electrodes. In the form of a differential this expression is written as

$$\frac{\partial(\Delta\theta)}{\partial x} = \frac{2\pi}{\Phi_0} B_y t_B$$

or more generally

$$\Delta\theta(\mathbf{r}, t) = \frac{2\pi}{\Phi_0} t_B [\mathbf{B}(\mathbf{r}, t) \times \hat{\mathbf{z}}] \tag{1.60}$$

the unit vector $\hat{\mathbf{z}}$ points in the direction perpendicular to the junction cross section. Integration of the differential leads to

$$\Delta\theta(x) = \frac{2\pi}{\Phi_0} B_y t_B x + \Delta\theta_0 \tag{1.61}$$

where $\Delta\theta_0$ is a constant and is the phase at the origin. Inserting this phase difference into the current-phase relation (Eq. 1.51) and integrating over the cross-section of the junction gives

$$I_s(B_y) = \int_{-l/2}^{l/2}\int_{-w/2}^{w/2} J_c(y,z)\ \sin[kx + \Delta\theta_0]\ dx\ dy \tag{1.62}$$

Here $k = \frac{2\pi}{\Phi_0} B_y t_B$ and I_s is the supercurrent flowing across the junction. Assuming spatial homogeneity of the maximum Josephson current density $J_c(x,y)$ in the direction of the applied field B_y and over the barrier height $-l/2 \leq x \leq l/2$, and zero outside yields the form of a diffraction pattern from a slit of width l with a constant transmission i_c

$$i(\Phi_J, \Delta\theta_0) = i_c \frac{\sin(\frac{\pi\Phi_J}{\Phi_0})}{\frac{\pi\Phi_J}{\Phi_0}} \sin(\Delta\theta_0) \tag{1.63}$$

The flux through the junction is $\Phi_J = B_y t_B l$ and the maximum supercurrent I_s^m that can be put through the junction occurs when $\sin(\Delta\theta_0) = \pm 1$, such that

$$I_s^m(\Phi_J) = i_c \left| \frac{\sin(\frac{\pi\Phi_J}{\Phi_0})}{\frac{\pi\Phi_J}{\Phi_0}} \right| \tag{1.64}$$

The Fraunhofer oscillation pattern modelled by Eq. 1.64 is illustrated in Fig. 1.14.

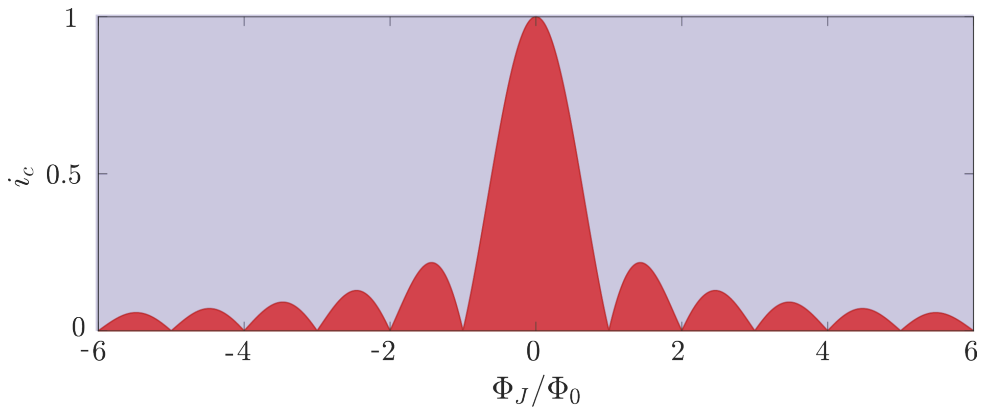

Figure 1.14: **Fraunhofer oscillations.** Dependence of the maximum supercurrent of a JJ on the applied magnetic field. The period is a flux quantum Φ_0.

This oscillation pattern is a signature of the Josephson transport to establish operation in Josephson regime. With all the theory presented in this section the JJ can be understood and characterised in a fundamental manner.

1.5.3 Superconducting quantum interference device (SQUID)

A superconducting quantum interference device (SQUID) can be formed by placing Josephson junctions within a superconducting loop. There are two main types of SQUIDs, RF and DC SQUIDs, which are formed by one or two JJs in a loop, respectively. In this work we only use a DC SQUID with two JJs in parallel, illustrated in Fig. 1.15. This configuration forms the basis of extremely sensitive detection of magnetic flux.

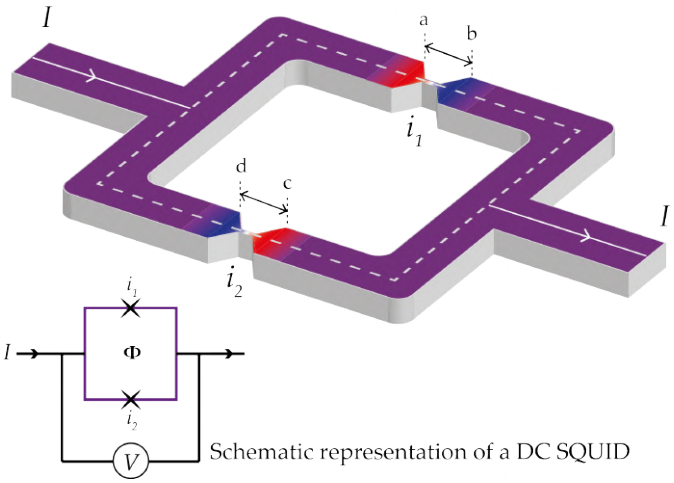

Figure 1.15: **SQUID.** Two Josephson junctions connected in parallel by a superconducting loop. The supercurrents across junctions $a \to b$ and $c \to d$ are labelled $(i_{1/2})$. The enclosed flux threading the loop is given by Φ. The path of integration $\boldsymbol{C}$ is shown by the dashed line.

The basic current relations for this device can be derived building upon what was presented in Section 1.5.1. As before we consider the junctions in a *lumped* circuit framework, which is to say that the gauge-invariant phase difference and current density are uniform over the cross-section of the junction.

The supercurrent across the first and second junction is given by the current phase relation Eq. 1.51, $I_{1/2} = I_c \sin(\Delta\theta_{1/2})$. Here $\Delta\theta_{1/2} = \theta_{b/c} - \theta_{a/d}$ refers to the phase difference across the respective junctions. The total current across the loop is then given by

$$\begin{aligned} I &= i_1 + i_2 = i_c \sin(\Delta\theta_1) + i_c \sin(\Delta\theta_2) \\ &= 2i_c \cos\left(\frac{\Delta\theta_1 - \Delta\theta_2}{2}\right) \sin\left(\frac{\Delta\theta_1 + \Delta\theta_2}{2}\right) \end{aligned} \tag{1.65}$$

The phase evolution around the loop is found by integrating the gauge invariant phase difference $\Delta\theta$ found in Eq. 1.56, around a closed contour $\boldsymbol{C}$ where the phase change must be an integer n multiple of 2π. Similar to what was shown in Section 1.5.2. The phase difference simplifies to

$$\Delta\theta_2 - \Delta\theta_1 = 2\pi n + \frac{2\pi\Phi}{\Phi_0} \tag{1.66}$$

This new expression for coupled phase differences can be substituted back into Eq. 1.65 to obtain the total current through the loop[15]

$$I = 2i_c \cos\left(\frac{\pi\Phi}{\Phi_0}\right) \sin\left(\Delta\theta_1 + \frac{\pi\Phi}{\Phi_0}\right) \tag{1.67}$$

In general, the superconducting loop also has an inductance L from the flowing currents that contribute to the total flux. Therefore, the contributions due to an external

applied flux Φ_{ext} and due to induction LI_{cir} must be considered. The currents can be written as

$$i_{1/2} = I' \pm I_{cir} \tag{1.68}$$

where $I' = (i_1 + i_2)/2$ is the average current common to both junction elements and generate no net flux through the loop. However, the circulating current $I_{cir} = (i_1 - i_2)/2$ generates a flux LI_{cir}, giving an expression for the total flux

$$\begin{aligned} \Phi &= \Phi_{ext} + LI_{cir} \\ &= \Phi_{ext} + Li_c \sin\left(\frac{\pi\Phi}{\Phi_0}\right) \cos\left(\phi_1 + \frac{\pi\Phi}{\Phi_0}\right) \end{aligned} \tag{1.69}$$

Equations 1.67 and 1.69 describe the behaviour of the SQUID and must be solved self-consistently. An important device parameter is the maximum driving current i_{max} that can be sent through the SQUID such that each junction does not exceed its critical current. The relative contributions of Φ_{ext} and LI_{cir} create limiting cases that can be aptly analysed with a *screening parameter* β_L defined as

$$\beta_L \equiv \frac{2Li_c}{\Phi_0} \tag{1.70}$$

The parameter represents the ratio of the maximum inductive flux and $\Phi_0/2$.

For the case of $\beta_L \ll 1$, the induction flux due to circulating current is small compared to the external flux. Then I_{max} for a given Φ_0 for the device is found by maximising Eq. 1.67 with respect to Φ_1, by imposing $di/d\Phi_1 = 0$. From this we obtain

$$I_{max} \simeq 2i_c \left|\cos\left(\frac{\pi\Phi_{ext}}{\Phi_0}\right)\right| \tag{1.71}$$

This is the maximum supercurrent allowed for two equivalent junctions placed in parallel and is a periodic function of the external flux.

For the case of $\beta_L \gg 1$ or a large inductance L, the inductive flux tends to compensate the applied flux and the device characteristics start to resemble that of a single superconducting loop. Therefore, the total flux will tend to the familiar quantisation condition

$$\Phi = \Phi_{ext} + LI_{cir} \simeq n\Phi_0 \tag{1.72}$$

$$I_{cir} \simeq \frac{\Phi_{ext} - n\Phi_0}{L} \tag{1.73}$$

From this it is clear that $I_{cir} \to 0$ for large L. The applied current splits equally in each of the SQUID arms and maximum supercurrent is found to be

$$I_{max} \simeq 2i_c - \frac{2\Phi_{ext}}{L} \tag{1.74}$$

We can also extract a relationship for the maximum change in the critical current of the SQUID (ΔI_c) or the modulation depth, and the screening parameter β_L

$$\Delta I_c \approx \frac{2}{\beta_L} i_c, \frac{1}{\beta_L} \ll 2i_c \tag{1.75}$$

The modulation of the maximum supercurrent of the SQUID by Φ_{ext} is roughly proportional to $1/\beta_L$ [12].

1.6 Conclusion

In this chapter the foundational theories and models of superconductivity are presented. Following the first experimental observation of zero resistance by Onnes in 1911, and the subsequent observation of perfect diamagnetism by Meißner and Ochsenfeld in 1933, new models had to be developed to explain the observations. The London theory tried to explain this state under an electrodynamical formulation but was unable to reconcile certain nuances. Ginzburg and Landau proposed a phenomenological model that exploited Landau's theory of continuous phase transitions, introducing an order parameter to describe the normal-to-superconducting phase transition capturing the macroscopic quantum nature of superconductivity. This theory is still reliable today as it provides an intuitive understanding of the observable properties of a superconductor. Despite its robust framework, the theory attracted tentative acceptance and scepticism since it lacked information regarding the underlying mechanisms leading to the macroscopic observations. The introduction of BCS theory provided a microscopic theory connecting the macroscopic properties, providing a widespread validation of the pheomenological models. The quantum theory explains the origin of superconductivity by the existence of an attractive interaction between two electrons via a lattice phonon. The formation of these *Cooper* pairs constitutes a macroscopic quantum state, with a unique value of the superconducting phase as described by Ginzburg and Landau's order parameter. The Ginzburg-Landau theory is indeed a limiting case of the BCS model close to the critical temperature ($T \approx T_c$).

The observation and control of quantum phenomena at a macroscopic scale holds immense power for applications. The exploration of type-II superconductivity, flux quantisation, Abrikosov vortices and the Josephson effect produced strides in expanding the understanding and possibilities of this unique state of matter. The discovery of superconductors with high critical temperatures in 1986 created more accessible possibilities for the implementation of superconducting technology since the equipment and energy requirement for cryogenic operation could be drastically reduced. Some applications of these effects include the development of sensitive magnetometers (SQUID), Josephson junction based digital circuits, particle detectors, powerful magnets for numerous applications, and several novel applications such as Abrikosov vortex driven superconducting electronics. The latter application is the driving force behind the work presented here. Complete optical control of the creation and manipulation of Abrikosov vortices, and the application of these techniques to control Josephson transport provides a scalable and dynamic path to the development of low-cost superconducting electronics. The presentation of these ideas and concepts allows the reader to put the work produced here in context. While this chapter presented a general survey on superconductivity and touched on certain relevant concepts, more specific background information will be provided within the chapters.

Bibliography

[1] H. K. Onnes. The resistance of pure mercury at helium temperatures. *Commun. Phys. Lab. Univ. Leiden*, 12, 1911.

[2] H. London & F. London. The Electromagnetic Equations of the Supraconductor. *Proceedings of the Royal Society A*, 149, 1935.

[3] J. G. Daunt, A. R. Miller, A. B. Pippard, & D. Shoenberg. Temperature Dependence of Penetration Depth of a Magnetic Field in Superconductors. *The Physical Review*, 74, 1948.

[4] M. Tinkham. *Introduction to Superconductivity: Second Edition*. Dover Publications, 2004.

[5] C. J. Gorter & H. Casimir. On supraconductivity I. *Physica*, 1, 1934.

[6] V. L. Ginzburg & L.D. Landau. On the Theory of superconductivity. *Zh .Eksp. Teor. Fiz.*, 20, 1950.

[7] L. D. Landau. On the Theory of Phase transitions. *Zh .Eksp. Teor. Fiz.*, 7, 1937.

[8] A. C. Rose-Innes & E. H. Rhoderick. *Introduction to Superconductivity*. Pergamon, 1978.

[9] D.R. Tilley & J. Tilley. *Superfluidity and Superconductivity*. CRC Press, 1990.

[10] J. Bardeen, L. N. Cooper & J. R. Schrieffer. Theory of Superconductivity. *Physical Review*, 108, 1957.

[11] F. London. *Superfluids*. Wiley, New York, 1950.

[12] Gross R., Marx A. & Deppe F. *Applied Superconductivity: Josephson Effect and Superconducting Electronics*. De Gruyter Textbook Series. Walter De Gruyter Incorporated, 2016.

[13] A. A. Abrikosov. On the magnetic properties of superconductors of the second group. *Journal of Experimental and Theoretical Physics*, 5, 1957.

[14] G. J. van Gurp. Flux-transport noise in superconductors. *Revue de Physique Appliquee*, 5, 1970.

[15] T. P. Orlando & K. A. Delin. *Foundations of Applied Superconductivity*. Addison-Wesley, 1991.

[16] G. Carneiro & E. H. Brandt. Vortex lines in films: Fields and interactions. *Physical Review B*, 61, 2000.

[17] H. F. Hess, R. B. Robinson, R. C. Dynes, J. M. Valles Jr. & J. V. Waszczak. Scanning-Tunneling-Microscope Observation of the Abrikosov Flux Lattice and the Density of States near and inside a Fluxoid. *Physical Review Letters*, 62, 01 1989.

[18] P. G. deGennes. *Superconductivity of metals and alloys*. Advanced Book Classics, Westview Press, 1966.

[19] J. Sok. Elementary Pinning Force on a Single Abrikosov Vortex in a Nb Film. *Journal of the Korean Physical Society*, 47, 09 2005.

[20] J. Sok & D. K. Finnemore. Thermal depinning of a single superconducting vortex in Nb. *Physical Review B*, 50, 11 1994.

[21] R. P. Huebener. *Magnetic Flux Structures in Superconductors*. Springer, Berlin, Heidelberg, 2001.

[22] I. S. Veshchunov, W. Magrini, S. V. Mironov, A. G. Godin, J. -B. Trebbia, A. I. Buzdin, Ph. Tamarat & B. Lounis. Optical manipulation of single flux quanta. *Nature Communications*, 7, 2016.

[23] A. Barone & G. Paterno. *Physics and Applications of the Josephson effect*. Wiley, 1982.

[24] B. D. Josephson. Possible new effects in superconductive tunnelling. *Physics Letters*, 1, 1962.

[25] C. Kittel. *Introduction to Solid State Physics, 8th Edition*. Wiley, 2004.

[26] Y. Aharonov & D. Bohm. Significance of Electromagnetic Potentials in the Quantum Theory. *The Physical Review*, 115, 08 1959.

Chapter 2

Experimental Methods

In this chapter we explore the various experimental methods and measurement set-ups used in this thesis. The details include the working principles, advantages and limitations of the techniques, and modifications made to our classic system to fit our new measurements.

The first section presents the operational principles of the cryogen free/closed cycle optical cryostation.

The second section focuses on the fundamental tool used through the course of this work, imaging of single vortices using magneto-optical imaging (MOI). There are several other methods to image single vortices that can provide excellent resolution and sensitivity, but MOI provides a unique avenue as a far-field optical technique that enables the combination of several other optical methods that allow the generation and manipulation of these fluxons. This section elucidates the imaging principle of MOI which is based on the Faraday effect. Details on the magneto-optical indicator, imaging contrast and the imaged vortex intensity profile will also follow.

The third section of the chapter focuses on optical manipulation which requires precise spatial control of a focused laser spot using a galvanometric mirror. A detailed characterisation and sample specific parameters are given, which will be used in our experiments.

The final section focuses on the set-up required to perform electrical transport measurements on a superconducting device within our cryostation. This section presents the instruments and tools required to perform these measurements, in addition to conceiving and designing the four-point probe measurement system. The handling and preparation of the device sample is also focused upon in greater detail. The ability to image and manipulate vortices while performing transport measurements is key to optical manipulation of Josephson transport.

2.1 Cryostation

A cryostation or cryostat is a system that is used to maintain low cryogenic temperatures of a particular sample or device under test. The cooling can be accomplished by different refrigeration methods. There are four primary types of cryostats namely bath, continuous-flow, multistage and closed-cycle. A bath cryostat contains a coldplate which is in contact with a cryogen (liquid helium or nitrogen) bath inside a vacuum flask. The cryogen needs to be manually refilled as it boils away. Similarly, a continuous-flow cryostat is also cooled using a cryogen bath but the cryogen is replenished continuously from a storage dewar. The temperature is controlled by controlling the flow rate of the cryogen. A multistage cryostat can reach cooler temperatures by assembling multiple cooler stages. Temperatures down to 1K can be reached by attaching the coldplate to a helium-4 isotope container, while temperatures below 300 mK can be achieved by using a rare helium-3 isotope, and temperatures of 1 mK are reached by using a dilution refrigerator. For our purposes, we use a commercially purchased closed-cycle optical cryostation that is capable of reaching temperatures of $\sim 3K$ within a cooling time of 4 hours. The refrigeration scheme used in this cryostation is the Gifford-McMahon (GM) refrigeration cycle, shown in Fig. 2.1 [1]. This method will be elucidated upon below.

2.1.1 Gifford-McMahon refrigeration cycle

The primary cooling components of a closed-cycle cryostation are the expander or cold head, and the compressor. The expander houses the regenerator and displacer cylinder where the refrigeration cycle takes place and it is connected to the compressor by two gas lines. One gas line supplies high pressure helium to the displacer controlled by the high pressure valve (HPV). The other gas line returns low pressure helium gas from the displacer and is controlled by the low pressure valve (LPV). The compressor provides the required helium gas flow rate to achieve the desired refrigeration capacity, and is also responsible for removing the heat of helium compression. The GM cooling cycle can be broken down into four stages [2] and is schematically illustrated in Fig. 2.1. The following stages also describe the process shown (a-d) in the inset Pressure-Volume plot.

1. The displacer is at the bottom of the cylinder, the LPV is closed while the HPV is opened. (a) Compressed helium initially at ambient temperature is introduced into the cylinder through the regenerator where the heat from the gas is given off into the regenerator material.

2. The pressure rises from P_L to P_H under the displacer, denoting the low temperature volume. While above the displacer the temperature rises due to adiabatic compression, denoting the high temperature volume. (b) The displacer is moved up either mechanically or pneumatically allowing the cooled gas to fill up the low temperature volume.

3. The low temperature volume achieves maximum volume as the displacer is in the top position. The HPV is closed and the LPV is opened. (c) With the opening of the LPV, the pressure falls in the low temperature volume as part of the gas will

flow through the regenerator towards the low pressure line of the compressor. This loss in volume allows the gas to expand and subsequently cool. Here the cooling capacity W of the cryostation is created.

4. The displacer moves down to its bottom position. (d) The cooled gas is pushed through the regenerator to the compressor to the cold finger where heat is extracted from the sample. This cycle is then repeated continuously.

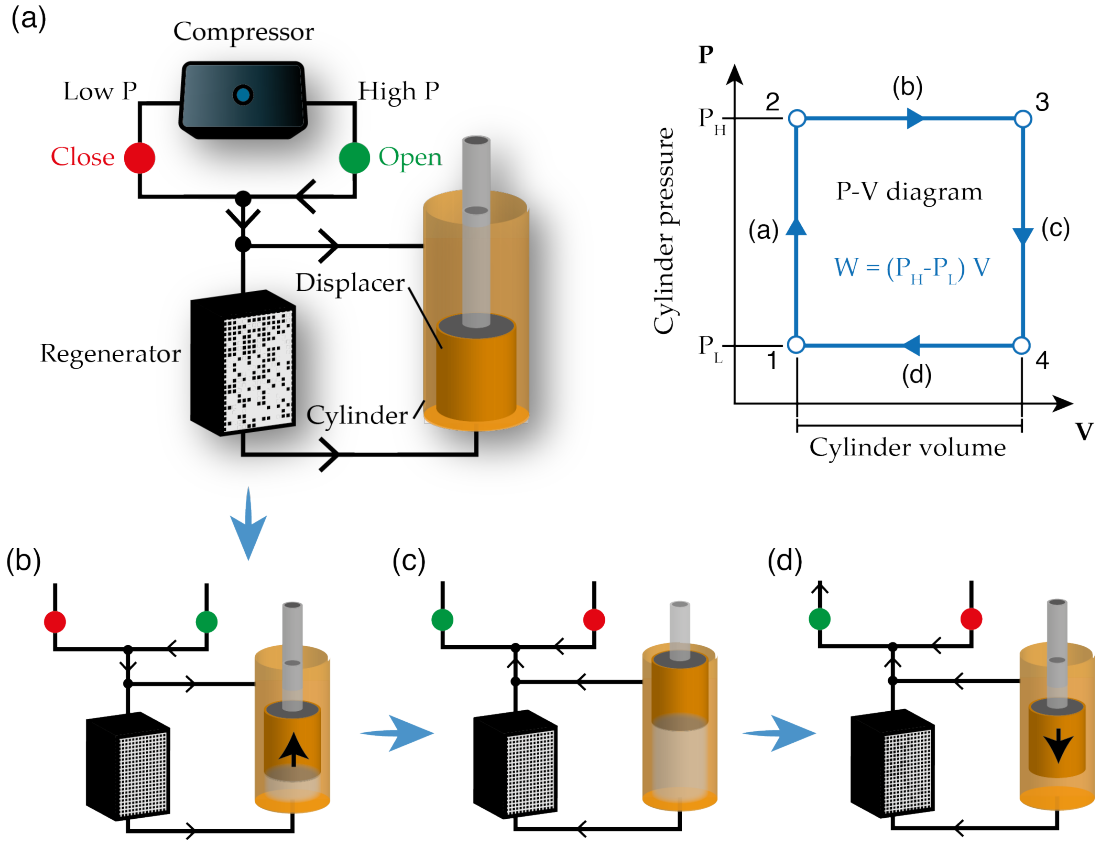

Figure 2.1: **Gifford-Mcmahon refrigeration scheme.** The four stages of the GM cooling cycle. The inset illustrates a Pressure-Volume plot that follows the thermodynamic cycle. The useful cooling power W is the product of change in pressure $(P_H - P_L)$ and volume V.

The widespread use of the GM refrigeration scheme stems from low vibration of the cold parts since the compressor and expander are decoupled and operate at different frequencies, namely the power-line frequency for the compressor and about $\sim$1 Hz for the expander. The low operating frequency results in less wear and tear of the components. Multi-staging in the scheme is also relatively facile. In order to cool down to lower temperatures $(\sim 3K)$, the refrigeration cycle occurs at two stages. As per convention, the *second* stage is cooled lower than the *first* stage and the sample is thermalised to the second stage. The vacuum shield surrounds the cold end of the expander in vacuum, limiting the heat load on the expander due to conduction and convection. The radiation shield is cooled by the first stage of the expander and insulates the second

stage from the room temperature thermal radiation. The optical cryostation used is illustrated in Fig. 2.2.

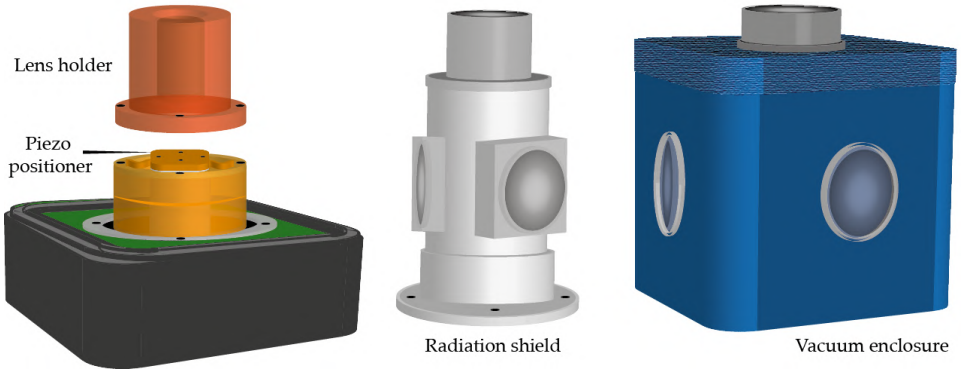

Figure 2.2: **Optical cryostation.** The outer components of the optical cryostation is illustrated. The sample platform is mounted on a piezo positioned with thermal link cables connected to the brass cylinder thermalised to the second stage ($\sim 3K$). The lens is held by a copper holder mounted on the brass cylinder. The radiation shield is then fixed, followed by the vacuum enclosure. Optical access is enabled through glass windows on the top and all four sides.

2.2 Magneto-optical imaging (MOI)

Several techniques have been used to investigate the properties of Abrikosov vortices in superconductors, exploiting various properties of the fluxon to obtain spatial and dynamical information. Techniques such as bitter decoration [3], electron microscopy [4, 5, 6], magnetic force microscopy [7], scanning SQUID microscopy [8], nitrogen-vacancy (NV) magnetometry [9], and magneto-optical imaging [10] directly probe the magnetic fields and resolve individual vortices. Prior to delving into the focus of this section which is magneto-optical imaging, it is important to briefly present some information about the other techniques with respect to spatial resolution, magnetic field sensitivity and image scan time [11].

Bitter decoration was the first technique used to image individual vortices in 1967 [3] and has been used ever since because of its relatively straightforward operational protocol. Fine ferromagnetic particles are scattered on the superconducting surface at low temperatures and the particles settle in patterns dictated by the magnetic fields emanating from the flux structures. The decorated pattern is then imaged under a scanning electron microscope at room temperature. Vortex localisation is maximised with the use of small particles (<10 nm) and with materials that have relatively shorter penetration depths resulting in high field gradients around the vortex. The technique can be used to localise vortices over large areas of hundreds of microns under low fields, but offers no dynamic bandwidth since the sample must be cleaned after every decoration.

Transmission electron microscopy allows imaging of magnetic vortices by analysing the phase shifts induced in incident electron wavefunctions by the vortex's magnetic field. Lorentz microscopy [4] and electron holography [5, 6] are two electron microscopy techniques that provide complementary information about vortex physics. This method offers high spatial resolution on the order of 10s nm in vortex localisation, with a modest field sensitivity ($\frac{1mT}{\sqrt{Hz}}$). Since the technique gives the position and polarity of the vortex in real-time, it is capable of high-speed imaging since no post-processing is required.

Magnetic force microscopy uses a small ferromagnetic tip to interact with the sample surface to obtain topographical information. High sensitivity requires a strong magnetic moment of the ferromagnetic tip which can potentially disturb the sample's magnetic domains due to the proximity of the tip to the surface [7]. High spatial resolution ($\sim$50 nm) can be reached with a smaller tip, but at the cost of field sensitivity. Scanning SQUID microscopy has been used to directly probe the fluxon magnetic fields in superconductors [8]. This technique possesses high field sensitivity, below $\frac{1pT}{\sqrt{Hz}}$, and sub-micron spatial resolution [12].

A relatively new method introduced to image vortex structures is based on performing magnetometry using NV centers in a scanning diamond tip [9]. NV centers are point defects in the diamond lattice that have magnetic-field-dependent energy-level splitting, which can be driven by resonant microwaves read out optically by laser excitation and fluorescence collection. This technique is highly sensitive, provides high spatial resolution, is applicable in a wide range of temperatures, and is capable of determining the magnitude and orientation of the magnetic field.

Magneto-optical imaging (MOI) offers a far-field optical method to imaging mag-

netic fields on the surfaces of superconductors. The strength of MOI lies in the fast acquisition times, while offering sub-micron spatial resolution [13] and field sensitivity of $\frac{1mT}{\sqrt{Hz}}$. The technique will be elucidated upon in great detail in the following sections.

2.2.1 Faraday effect

Conventional MOI of flux structures is based on the magneto-optical *Faraday effect*. It describes the rotation, $d\theta_F$, of linearly polarised light going through an infinitesimal thickness of a Faraday rotator medium $d\mathbf{r}$, in a magnetic field $\mathbf{B}(\mathbf{r})$. In general $\mathbf{B}(\mathbf{r})$ is not uniform in the direction of propagation. The rotation of the polarisation vector is described by the relation

$$d\theta_F = \mathcal{V}\mathbf{B}(\mathbf{r}) \cdot d\mathbf{r} \tag{2.1}$$

where $\mathcal{V}$ is the *Verdet constant* that quantifies the rotation power for a medium and varies both with frequency and temperature.

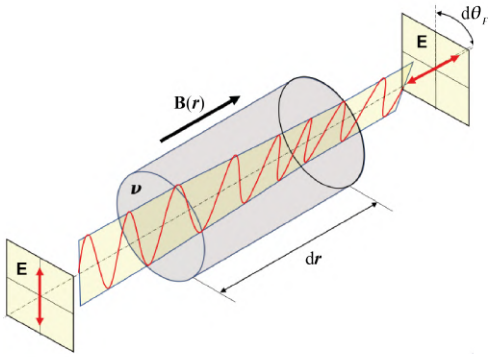

Figure 2.3: **Faraday effect.** The rotation of linearly polarised light induced by a magnetic field $\mathbf{B}(\mathbf{r})$.

The optical rotation effect can be understood in terms of circular birefringence, which refers to the refractive index of a material being different for right circular polarised light (RCP) and left circular polarised light (LCP). The effect can be understood by considering an electromagnetic wave linearly polarised along the x-axis, which can be decomposed into a superposition of two circularly polarised components

$$\begin{aligned} \mathbf{E} &= E_o \cos(kz - \omega t)\hat{\boldsymbol{x}} \\ \mathbf{E} &= \frac{1}{2}\mathbf{E}_L + \frac{1}{2}\mathbf{E}_R \end{aligned} \tag{2.2}$$

where ω and k are the angular frequency and wave vector, respectively. The LCP and RCP components decompose as

$$\mathbf{E}_L = E_o \cos(k_L z - \omega t)\hat{\boldsymbol{x}} + E_o \sin(k_L z - \omega t)\hat{\boldsymbol{y}} \tag{2.3}$$

$$\mathbf{E}_R = E_o \cos(k_R z - \omega t)\hat{\boldsymbol{x}} - E_o \sin(k_R z - \omega t)\hat{\boldsymbol{y}} \tag{2.4}$$

In a refractive medium $k_{L/R} = n_{L/R}\omega/c$, where $n_{L/R}$ is the refractive index for the respective polarisation directions and c is the speed of light. The average refractive index is given by $n = \frac{1}{2}(n_L + n_R)$. In this case the refractive index will be different for LCP and RCP light. Therefore after traversing a distance, z, through the medium the wave will acquire a phase delay between the two components ($\Delta n \equiv n_L - n_R$) and become

$$\mathbf{E} = E_0 \left(\cos\left(\frac{\Delta n \pi z}{\lambda}\right)\hat{\boldsymbol{x}} + \sin\left(\frac{\Delta n \pi z}{\lambda}\right)\hat{\boldsymbol{y}} \right) \cos\left(nkz - \omega t\right) \tag{2.5}$$

The beam is still linearly polarised but the polarisation has been rotated by an angle

$$d\theta_F = \frac{\Delta n \pi}{\lambda} dz \tag{2.6}$$

It is clear that the rotation of the polarisation is directly related to the birefringence of the medium (Δn), the distance travelled in the medium (dz) and the wavelength of light (λ) in vacuum.

Having described the optical rotation in terms of refraction, the role of an applied magnetic field on this effect can now be included [14]. In the classical model, the interaction of an electromagnetic wave with a dielectric material occurs via perturbations to the electron cloud which will become polarised according to the electric permittivity, ϵ, of the medium. The displacement vector $\mathbf{r}$ describes the transverse motion of the electron. The force on an electron due to electric and magnetic fields is given by the Lorentz force. The restoring force constant of the electron is given by $\omega_0^2 m_e$, where ω_0 is the natural oscillation frequency of the electron and m_e is the electron mass. For completeness there is also a damping factor present which is proportional to $d^3\mathbf{r}/dt$, but since the optical frequency is selected to be far from resonance $\omega \ll \omega_0$, it can be neglected. The equation of motion can be written as

$$m_e \frac{d^2\mathbf{r}}{dt^2} + \omega_0^2 m_e \mathbf{r} = -e(\mathbf{E} + \frac{d\mathbf{r}}{dt} \times \mathbf{B}) \tag{2.7}$$

Equations 2.3 & 2.4 can be inserted into the equation of motion to obtain displacement vectors for LCP and RCP waves

$$\mathbf{r}_{L/R} = -\frac{e/m_e}{\omega_0^2 - \omega^2 \mp \omega_B \omega} \mathbf{E}_{L/R} \tag{2.8}$$

where $\omega_B = eB/m_e$ is the cyclotron angular rotation frequency.

The distortion of the electron cloud is characterised by the polarisation vector $\mathbf{P}$ = -*Ne***r**, where *N* is the atomic number density. We can further define the plasma frequency, $\omega_p^2 = 4\pi N e^2/m_e$. Subsequently dipole moments for LCP and RCP light are given as

$$\mathbf{P}_{L/R} = \frac{\omega_p^2}{\omega_0^2 - \omega^2 \mp \omega_B \omega} \mathbf{E}_{L/R} \tag{2.9}$$

Given the constitutive relation $\mathbf{P} = (\epsilon - \epsilon_0)\mathbf{E} = \epsilon_0 \chi \mathbf{E}$ and $n^2 = 1 + \chi$, refractive indices for the two circular polarisations are

$$n_{L/R}^2 = 1 + \frac{\omega_p^2}{\omega_0^2 - \omega^2 \mp \omega_B \omega} \tag{2.10}$$

From this we see that $n_L \neq n_R$, so the LCP and RCP waves will travel at different phase velocities. Following that, given $\omega, \omega_0 \gg \omega_B$, n and Δn can be explicitly determined as

$$n = \frac{1}{2}(n_L + n_R) \approx 1 + \frac{\omega_p^2}{(\omega_0^2 - \omega^2)} \tag{2.11}$$

$$\Delta n = n_L - n_R \approx \frac{\omega_p^2 \omega \omega_B}{(\omega_0^2 - \omega^2)^2} \tag{2.12}$$

These expressions are valid when the detuning $(\omega_0 - \omega)$ is far from resonance. Inserting these into the expression for Faraday rotation found earlier (Eq. 2.6), and substituting the expressions for ω_B and $\omega = 2\pi c/\lambda$ gives

$$d\theta_F = \frac{\Delta n \pi}{\lambda} dz = \frac{e}{2m_e c} \frac{\omega_p^2 \omega^2}{(\omega_0^2 - \omega^2)^2} B dz \tag{2.13}$$

We can extract an explicit expression for the Verdet constant $\mathcal{V}$ revealing the dependence on microscopic parameters and frequency.

$$\mathcal{V} = \frac{e}{2m_e c} \frac{\omega_p^2 \omega^2}{(\omega_0^2 - \omega^2)^2} \tag{2.14}$$

In the general case, the total Faraday rotation acquired in a non-uniform field with a medium of thickness dz is obtained by integrating the expression [15]

$$\theta_F = \mathcal{V} \int B(z) \cdot dz \tag{2.15}$$

2.2.2 Magneto-optical indicator

In a typical MOI geometry, light passes through the Faraday rotator or magneto-optical indicator, is reflected at the sample surface passing through the indicator a second time, acquiring a rotation angle $2\theta_F$. There are a few critical parameters that must be considered in choosing a magneto-optical indicator for single-vortex imaging. An indicator with a large Verdet constant is ideal, but the total acquired rotation is also proportional to the thickness of the indicator. However, thicker films will inherently absorb more light and most MO indicator materials tend to have a high absorption coefficient α, therefore, the indicator thickness should be a maximum of $1/\alpha$. From this, the optimum condition for the effect can be achieved by maximising the figure of merit $\mathcal{V}/\alpha$ [16]. Another parameter to consider is that the magnetic field of a vortex decays very quickly above the surface of the superconductor ($\sim$ 100s nm), and with a fast diverging field the effective Faraday rotation is diminished if the indicator-superconductor interface distance is not minimised. This can be done by physically pressing the indicator or directly depositing the indicator on top of the superconductor. Due to the application of these indicators to superconductors, the indicators should also be functional at low temperatures.

The inception of MOI saw the use of cerium salts as the MO indicator on type-I lead, which had a small absorption and a reasonable Verdet constant, but with a spatial resolution limited to 250 μm due to the large indicator thickness required to fulfill the contrast condition [17]. This is to say that a thick indicator was required to acquire sufficient Faraday rotation that the signal was above the noise of the imaging system. To overcome the low spatial resolution, thin MO indicators with high Verdet constants were realised with the use of europium chalkogenides EuS and EuSe. These materials are paramagnetic above transition temperatures of 2.8 and 4.6K, respectively, after which they undergo ferromagnetic or antiferromagnetic transitions at temperatures. These transition temperatures can fall above the T_c of some superconductors. The working temperature range is further limited by decreasing Verdet constants with

increasing temperature. These compounds also tend to have low magnetic sensitivity ($\sim$ 10 mT). Although challenging, the direct deposition of a 40 nm film of EuSe has been achieved to perform single vortex imaging, above its antiferromagnetic transition, with a resolution of 0.8 μm in Nb [13].

In contrast to europium chalkogenides, bismuth, lutetium and yttrium based ferrite garnet films (FGF) have also been successfully employed as MO indicators. The doping concentration of these elements determines the magneto-optical properties of the garnet [18]. FGFs with in-plane ($\mathbf{M}_{\parallel}$) magnetisation allow sensitive detection ($\sim 10\mu$T) of magnetic fields normal to the in-plane magnetisation vector ($\mathbf{B}_{\perp}$). The observation of magnetic flux is indirect since one observes the changing of the magnetisation ($\mathbf{M'}$) of the indicator's domains due to an external field. The domains can be observed to have a distinct saw-tooth structure. These films are typically grown on a transparent gadolinium-gallium-garnet (GGG) $Gd_3Ga_5O_{12}$ garnet substrate with a mirror on top of the FGF. The mirror layer was traditionally fabricated as a means to protect the garnet face, but also for maximising the reflection of light as sample surfaces were not particularly reflective. With metallic superconductors the reflection from the sample surface is high so the mirror is generally omitted to minimise the distance at the superconductor-indicator interface [19].

In the course of this work, the MO indicator used is a 2.5 μm-thick Bi:LuIG garnet of composition $Bi_xLu_{3-x}Fe_{5-z}$ Ga_zO_{12} with $x \sim 0.9$ and $z \sim 1.0$, grown on a GGG substrate for a total thickness of $\sim$451 μm. The Verdet constant is determined by placing the indicator between a pair of coils that can generate up to $\sim$ 180 mT, and recording the extinction $\epsilon = P_{min}/P_{max}$ at a series of applied fields for a diode laser at λ = 532 nm. The equivalent Faraday rotation is $\theta_F = \sin^{-1}(\sqrt{\epsilon})$. A Verdet constant of $\sim 0.06°$ $mT^{-1}\mu m^{-1}$ is obtained by fitting the linear part of the plot prior to saturation, shown in Fig. 2.4a. In Fig. 2.4b the Verdet constant is similarly measured over a range of optical wavelengths, plotted along with a transmission spectrum [20]. The imaging is performed at 550 nm, which is a spectral maxima for the Verdet constant and provides a modest 43% transmission for the garnet [21, 22].

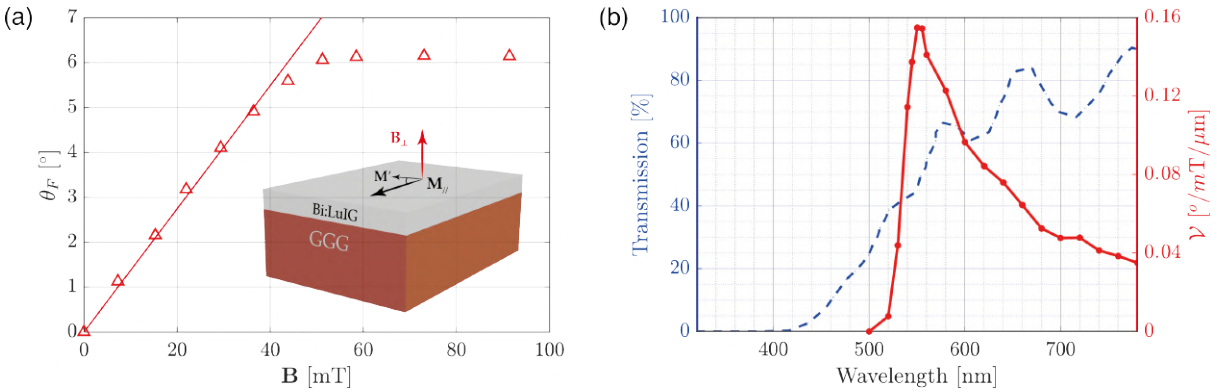

Figure 2.4: **Bi:LuIG magneto-optical characterisation.** **(a)** Faraday rotation for a 2.5 μm Bi:LuIG MO indicator at 532 nm. The magnetisation ($\mathbf{M}_{\parallel}$), applied magnetic field ($\mathbf{B}_{\perp}$) and the local disordered magnetisation ($\mathbf{M'}$) vectors are illustrated in the inset. **(b)** The wavelength dependence of the Verdet constant and transmission are plotted to illustrate an optimal measurement wavelength of 550 nm.

2.2.3 Vortex imaging

2.2.3.1 Optical set-up

In our measurements we use niobium of thickness ∼100 nm in various structural configurations (films, devices, strips, etc.) grown on a sapphire substrate (500 μm) using magnetron sputtering, unless specified otherwise. The MO indicator Bi:LuIG is placed on top of the superconductor. Wide-field imaging is then performed by focusing the incoherent white light filtered at 549 nm, on the back focal plane of an aspherical lens placed inside the cryostat with a numerical aperture NA = 0.49. The NA is further diminished to 0.215 mainly due to the aperture of the bracket holding the MO indicator in place. Light traverses through the MO indicator and is then reflected from the surface of the superconductor passing through the MO indicator again, doubling the Faraday rotation [23]. The full MOI setup is illustrated in Fig. 2.7 and a conventional sample is shown in the inset.

2.2.3.2 Imaging contrast

The quality of incident polarisation subsequent extinction by the analyser determines the contrast obtained in MOI. The sample is placed between two polarisers in a nearly-crossed configuration with an offset angle ϕ, as illustrated in Fig. 2.5. After passing through the MO indicator, the light returns with the polarisation plane rotated by $2\theta_F$. The electric field **E** of the reflected light can be decomposed into components parallel, $|\mathbf{E}|\sin(2\theta_F)$, and perpendicular, $|\mathbf{E}|\cos(2\theta_F)$, to the direction of the transmission of the analyser [24]. The condition for MO contrast is obtained by taking the intensities $|\mathbf{E}|^2$ for the two components after the offset analyser as

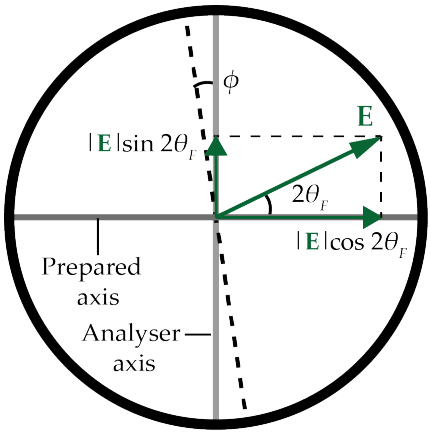

Figure 2.5: **Magneto-optical contrast.** Schematic of the polarisation axes and light polarisation as it arrives at the analyser with a rotation θ_F relative to the incident light polarisation.

$$T_{||}|\mathbf{E}|^2\sin^2(\phi+2\theta_F) > T_{\perp}|\mathbf{E}|^2\cos^2(\phi+2\theta_F),$$

where $T_{||}$ and $T_{\perp}$ denote the light transmittance parallel and perpendicular to the analyser axis. An extinction coefficient for the analyser can be defined as $\epsilon = T_{||}/T_{\perp}$ or for practical purposes $\epsilon = P_{min}/P_{max}$, where $P_{min/max}$ refers to minimum and maximum power obtained through the analyser, respectively. For small angles, the contrast condition is given as $2\theta_F > \sqrt{\epsilon}$.

There is an optimal value for ϕ which depends on the finite extinction of the polarisers. Consider the expressions for light intensities received by the detector before (I_1) and after (I_2) the application of the magnetic field, where I_0 is the incident light intensity. These expressions are given as

$$I_1 = I_0 \left[\sin^2(\phi) \cdot T_{||} + \cos^2(\phi) \cdot T_{\perp}\right] \tag{2.16}$$

$$I_2 = I_0 \left[\sin^2(\phi + 2\theta_F) \cdot T_{||} + \cos^2(\phi + 2\theta_F) \cdot T_{\perp}\right] \tag{2.17}$$

Expanding I_2 in the first order of θ_F, one obtains

$$I_2 = I_0 \left[\sin^2(\phi) \cdot T_{||} + \cos^2(\phi) \cdot T_{\perp} + 2\theta_F \cdot \sin(2\phi) \cdot (T_{||} - T_{\perp})\right] \tag{2.18}$$

Only the third term has information (θ_F) regarding the flux distribution, while the other terms are parasitic. For small values of ϕ the second term will dominate, while for large values of ϕ the first term will dominate. The optimum value for ϕ is found by maximising $\Delta I = I_2 - I_1$ compared to the unrotated light, $C = \Delta I / I_1$. Since small rotation angles are observed in experiment, a simplified relation for contrast is obtained as $C = 4\theta_F/\phi$, with maximal contrast achieved when $\phi = \sqrt{\epsilon}$ [25].

2.2.3.3 Image acquisition scheme

The vortex image is acquired under a background subtraction scheme which is necessary to exclude the significantly higher contribution of the incident light due to the offset ϕ in the signal passed through the analyser. Here I_1 refers to the intensity pertaining to the background image taken above T_c when the flux structures have not formed, while I_2 is the image taken below T_c when the vortices have formed. For low-T_c superconductors like Nb films ($T_c \sim 8.6K$), the imaging is performed at the lowest platform temperature of $\sim 4K$, while the background is taken at $\sim 10K$. The difference in temperature is not significant, therefore the there is limited thermally induced movements of the mechanical components of the cryostat, like expansion and contraction of the metal. This results in minimal image misalignment between the images taken above and below T_c, and the subtraction scheme works. For high-T_c superconductors ($T_c \sim 86K$), the imaging ideally also has to be performed as close to the platform base temperature as possible because the size of the vortex will be smaller and subsequently the concentration of the flux quantum will be denser. This makes the flux structures easier to detect. However, the large difference in background and imaging temperatures inherently creates sufficient thermally induced mechanical misalignment where the background image is no longer aligned and flux structures cannot be discerned.

2.2.3.4 Vortex intensity profile

The magnetic field distribution of a single vortex is derived in Section 1.4.1.1 and recalling the magnetic monopole model, the magnetic flux density is obtained by taking the gradient of the scalar potential $B_{vx} = -\nabla\Phi_{vx}(r, z)$. The flux $B_{vx}(r, z)$ needs to penetrate the MO indicator, which leads to the perturbations in the in-plane magnetisation. However, in practice there is a space z_g between the indicator and the surface of the superconductor where the vortex flux is lost. This lowers the signal and the resolution of the imaging system. The expression for the Faraday rotation angle in Eq. 2.1 can be modified to include the effect of the gap.

$$\theta_F = 2\mathcal{V} \int_{z_g}^{z_g+d} B_{vx}(r, z) \cdot dz = 2\mathcal{V} \left[\Phi_{vx}(r, z_g + d) - \Phi_{vx}(r, z_g)\right] \tag{2.19}$$

where dz is the thickness of the MO indicator. This expression can be inserted back into Eq. 2.17 to obtain a full expression for the intensity. In addition to this, the limited resolution of the optical system also must be taken into account.

The final image obtained is indeed a convolution of the intensity profile and the point spread function (PSF) of the diffraction limited laser spot. A PSF is described as the response of an imaging system to a point source, or in other words, given the fundamental limitations of diffraction, what is the imaging system able to ideally resolve. In Fig. 2.6a. a standard image obtained using the MOI set-up is shown. In Fig. 2.6b. the intensity profile of one of the vortices is provided. The full width half maximum (FWHM) of this vortex is $\sim$1.7 μm. In general, the size of the imaged vortex is dependent on the distance z_g and also the temperature. As $T \to T_c$, the physical size of the vortex grows larger, therefore the imaged size also grows larger [22].

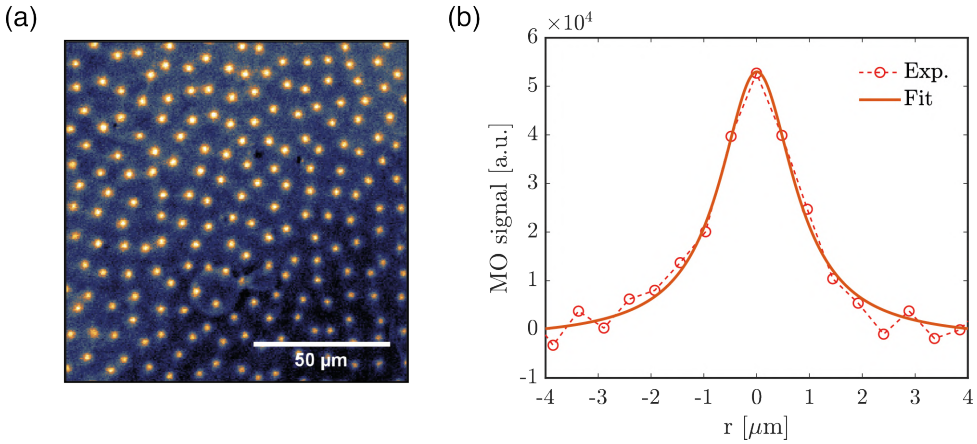

Figure 2.6: **Vortex imaging.** (a) An image of single vortices resolved using the MOI set-up in a Nb film of 100 nm, taken at 4.5K in a field of $\sim$ 30 μT. (b) Intensity profile of a single vortex with a FWHM size of $\sim$1.7 μm.

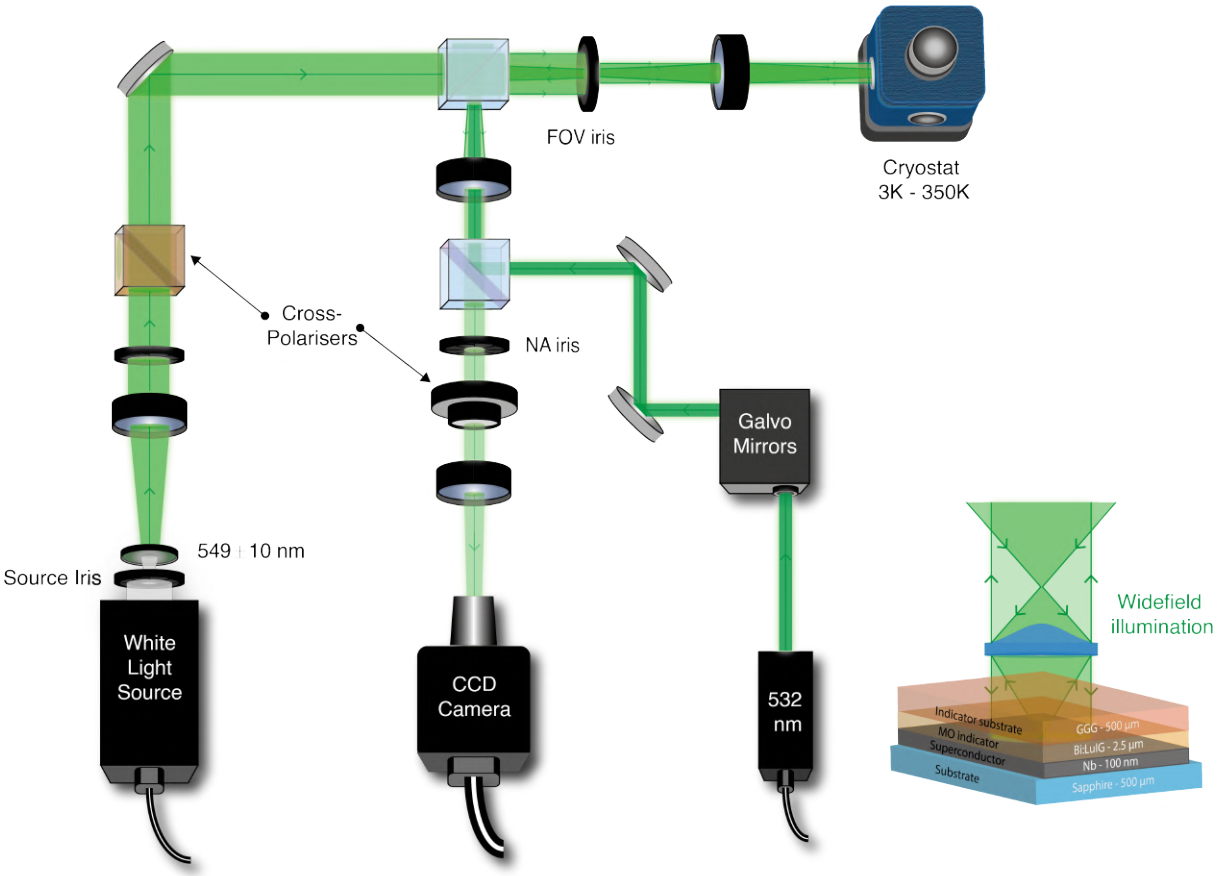

Figure 2.7: **MOI setup.** Schematic illustration of the conventional magneto-optical setup. The sample is placed between two near-crossed polarisers with an offset angle, where the offset is taken from the cross Nicol condition. The optimal offset angle (ϕ) in radians is determined by the value of the extinction ratio ϵ of the polariser. MOI is realized with illumination from an incoherent white light source filtered at $\lambda = 549$ nm $\pm$ 10 nm. The filter's central wavelength corresponds to a local maximum in the MO indicator's rotational power. The second arm of the set-up couples a 532 nm cw laser via galvanometric mirrors to allow laser scanning or independent movement of the laser spot. Vortices are imaged on reflection by a CCD (charge-coupled device) camera. The CCD camera is 512 $\times$ 512 pixels with an area of 13 $\times$ 13 μm^2, having a 16-bit resolution and a quantum efficiency greater than 80% between 450 and 650 nm. In accordance with Köhler configuration, an aperture diaphragm is placed in front of the lamp (source iris). Additional diaphragms to control the field of view (FOV iris) and to control the NA (NA iris) are also shown. (inset) The sample consists of a magneto-optical indicator placed in close contact with the superconductor surface.

2.3 Vortex manipulation

Vortex flow in superconducting devices is what is responsible for loss of dissipationless supercurrent, thus limiting the range of operation. Pinning forces due to local defects play a key role in limiting the movement of vortices. Consequently controlled defect implantation to create strong pinning centers is a common means of engineering enhanced critical currents [26, 27, 28]. The drawback of implantation or fabrication of defects is that this configuration cannot be altered further and there is no dynamic control of vortex distribution.

In contrast, there are several techniques that allow real-time control and manipulation of flux structures. Moving Bloch walls of a ferrite MO indicator can be used to move or sweep the vortex landscape [29] shown in Fig. 2.8a. Single vortex manipulation can be achieved by means of a local probe such as those used in various probe microscopy techniques. These include the use of magnetic force microscopy tip [30, 31] shown in Fig. 2.8b., a SQUID on a tip [32, 33, 34] shown in Fig. 2.8c., and a scanning tunneling microscopy probe [35]. A combination of well located microholes, low vortex density and electrical pulses have also been used to displace single vortices [36]. While a proof of concept for vortex manipulation has been shown with these techniques, they are not as straightforward to implement in cryogenic environments and tend to be slow, lacking the capability of fast in-situ vortex manipulation and imaging over large areas.

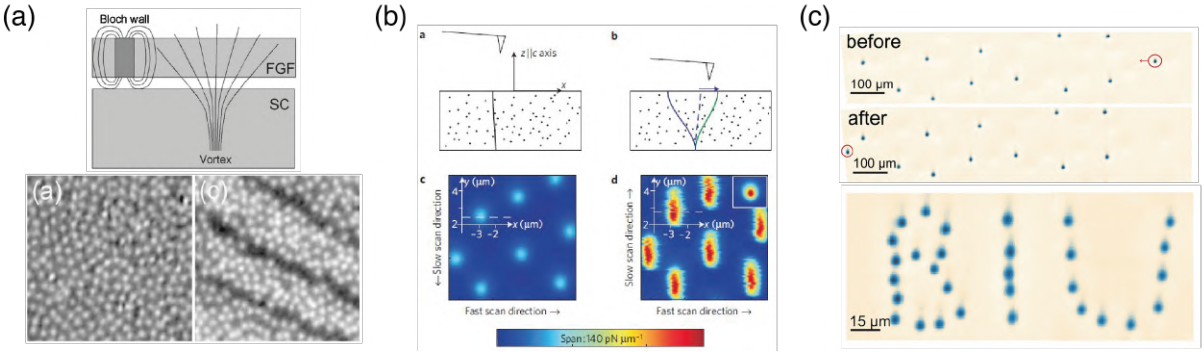

Figure 2.8: **Vortex manipulation.** (**a**) With an initial vortex distribution, vortex free channels can be created at the turning point of the domain wall [29]. (**b**) Using an MFM probe the tip's magnetic field displaces a single vortex in YBCO from its columnar axis [**?**]. (**c**) The applied field from a SQUID mounted on a cantilever can also be used to manipulate single vortices into arbitrary formations [33]

To this end, in our group we have developed a far-field optical method based on local heating of the superconductor using a focused laser spot to create optical tweezers that is able to perform fast and precise manipulation of individual Abrikosov vortices [21, 37]. This technique plays a critical role in the realisation of the goal of this project as it couples with the MOI set-up and the optical generation of vortex pairs [22, 38], creating an arsenal of self-sustained optical methodology to control Josephson transport.

2.3.1 Optical manipulation

As examined in Section 1.4.1.3, a thermal force created by locally heating the superconductor is capable of displacing a vortex [39]. The thermal force per unit of vortex length is given by

$$f_{th} \approx \frac{\Phi_0^2}{4\pi\mu_0\lambda_0^2} \ln\left(\frac{\lambda_0}{\xi_0}\right) \frac{\nabla T}{T_c} \tag{2.20}$$

As seen from the expression the magnitude of the force is directly dependent on the thermal gradient. A focused laser spot in conjunction with minimal lateral heat diffusion can create a strong gradient capable of overcoming the pinning force, $f_{th} > f_p$. The heating can be easily controlled by modulating the power of the laser.

The study performed in Ref. [37] characterises this technique completely. A local hot spot is created by focusing a laser beam down to a diameter of $\sim 1\mu$m causing a rise on the order of a Kelvin in temperature without surpassing T_c. The temperature gradient attracts the vortex to the center of the laser spot and as the laser is moved the vortex follows the laser as with the optical tweezers. When the laser is cut, the vortex remains trapped in the last position it was moved to. The laser beam can be spatially driven to follow a path or in a scanning mode with the use of galvanometric mirrors placed in a telecentric configuration (shown in Fig. 2.7). Single vortex manipulation and scanning vortex removal are shown in Fig. 2.9.

This technique has practical implications for use in superconducting devices. Since vortices tend to be a source of noise, this method can be used to clean out the superconductor of flux structures. The precision and speed of the laser scanning is limited by the galvanometric mirrors. An area of 70×70 μm^2 can be cleared in 350 ms which corresponds to a speed of 6 mm/s. Faster scan speeds can be accessed by exploring the ratio of the laser spot size and the thermal response of the sample ($\sim$ ns), working up to a maximum speed dictated by the speed of vortex travel ($\sim$ km/s).

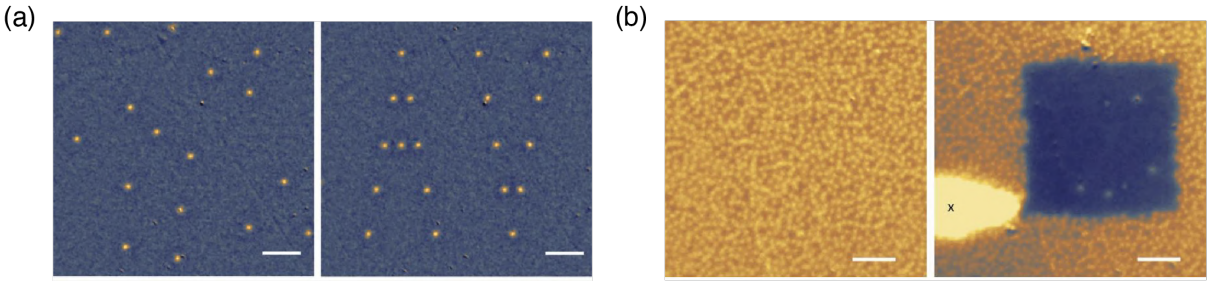

Figure 2.9: **Optical vortex manipulation.** (**a**) MO image of vortices in a low field-cooled condition. After which the vortices are displaced one at a time to form the letters 'AV'. (**b**) Sample field-cooled in a higher field to have a denser distribution of vortices. A vortex-free region can be formed by displacing vortices in mass by scanning the laser, like a vortex broom. Scale bars are 20 μm [37]

The sample used for this study was a ~90 nm Nb thin film on silicon. It must be clear that the pinning strength in the sample is completely dependent on the particular

sample's morphology and defect landscape. There is a minimum absorbed power that is required to overcome the pinning of single vortices and in this sample there is a large distribution of the input power reinforcing the dependence of sample morphology on pinning potentials. By placing the laser spot 1.1 μm from a vortex and calculating the absorbed power required to displace the vortex, a thermal gradient of 1.4 K/μm is estimated. This gives a maximal pinning force per vortex unit length of $f_p \sim 14pN/\mu$m. As expected the pinning force also depends on the base temperature and follows the empirical power law $f_p \propto (1 - T/T_c)^\gamma$ where $\gamma = 3.4$. In addition to that, the ability of a sample to create a high thermal gradient depends on the choice of substrate and its thermal conductivity. In fact, the higher thermal conductivity of sapphire should provide a larger thermal gradient due to its better heat evacuation capability, limiting lateral spread of heat.

2.4 Transport measurements

When characterising the electrical behaviour of superconductors, it is the current-voltage relationship, or I-V curve, that is primarily measured, and all other quantities are derived from it. The key parameter derived from this measurement is the critical current (I_c), which is further determined as a function of temperature and magnetic field. This section provides an overview of the equipment, techniques and procedures implemented for the first time in our group, to perform transport measurements on superconducting devices.

2.4.1 Instrumentation

The transport measurements are acquired using a current source and a nanovoltmeter. The leads of the 4-terminals from the device under test (DUT) inside the cryostation are connected to the measurement instruments. The output from the cryostation is facilitated using a magnetically shielded cable which terminates at a connector terminal, separating the input/output from the individual pins. The connector terminal has individual grounding switches for each of the pins. The transport measurements are run programmatically using a Python and LABVIEW code, while the instruments are connected to the computer using a GPIB connection.

The current source is programmable for output currents from 100 fA to 100 mA, while the nanovoltmeter has a 1 nV sensitivity with a range of 1nV-100V. The combination of these two instruments allows for fast and low noise conductance measurements in a single measurement pass. The two instruments are connected with the use of a trigger link. In the case of a simple I-V measurement, a range of currents can be swept as a trigger signal is sent from the source to the voltmeter. The instruments can also be used for single shot measurements for specific measurement conditions.

The speed of the measurement is determined by the integration time of the Analog/Digital converter, or the period of time the signal is measured. The integration time affects the amount of reading noise that will appear in the measurement. The integration time can be be set from 166.7 μs to 83.33 ms, per single reading, and can be chosen as a power line cycle (PLC) setting. In general the 2182A has a parabolic relationship between the speed and noise characteristics, with an optimal rate between 16.67 ms to 83.33 ms which has the lowest noise.

The measurements are performed in a four-point probe configuration. The device design contains two electrode leads per side to accommodate separate connections for current application and voltage reading, as shown in Fig. 2.10. Compared to a two-point probe configuration, the four-point set-up eliminates contact resistance stemming from the lead resistances of the source that can be added to the voltage measurement across the DUT. This is the case since the voltage is not just read across the DUT but along the entire line including the lead resistance of the source. For measurements involving variations of small resistances, as in the case with superconductive devices, this contact resistance can be a source of error since lead resistances can range from 10 $m\Omega$ to 1 Ω.

We use home-built solenoid copper coils to generate magnetic flux along the optical axis and perpendicular to the sample plane. The copper wire used for the coils has

a resistance of $<1\ \Omega$ and can only sustain a maximum voltage of $1V$ before there is noticeable heating of the wires. Rather than using a single set of coils, the use of a pair of coils in the Helmholtz configuration is more common and can generate larger fields. However, given the limitation of size and space around the cryostation, the single coil configuration is used to generate maximum flux of 10 mT, measured at the sample plane.

2.4.2 Sample preparation

Combining transport measurements with MOI is a key aspect of the device design and sample preparation. At the minimum, MOI requires space over the device for the MO-indicator and a holding apparatus. Therefore, the electrode lines have to run outwards to the connection pads far longer than a standard device. In addition to that, due to the limited space in the cryostat, a commercial four-point probe set-up cannot be integrated. Therefore, all sample holders, wiring and connections have to adhere to the tight limitations. The previous method of adhering the terminal wires with silver paste did not fare well because the adhesion only lasted one or two cool-down cycles. The fragile connections also made it difficult to reproduce data and reuse devices. These are well-known issues with using silver paste for this purposes, and due to the electrically sensitive nature of the device, this was a major source of problems.

2.4.2.1 Probes

The problems pertaining to connecting the device in a safe and reproducible manner was addressed by the conception and fabrication of home-built probes. The design was relatively straightforward to follow the model of a sharp tip that would make contact with the device pads, while being large enough that it could be manipulated by hand. The prepared device sample is shown in Fig. 2.10. The probes have a triangular shape with the larger back-end being held firm by a polymer screw. The probe also has an arched shape to further ensure that only the sharp tip makes contact with the device pads. The probe is isolated from the base copper plate using an insulating tape and the polymer screw. The probe material is berrylium-copper (BeCu), while the wire connecting to the probe is made of manganin. Both materials have low resistance, are non-magnetic, and retain their strength and thermal conductivity at cryogenic temperatures.

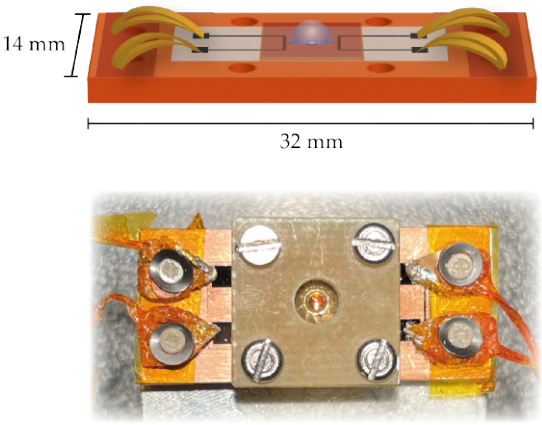

Figure 2.10: **Device sample.** A device prepared for transport and imaging measurements. The probes are isolated from the copper sample holder using polymer screws and tape.

2.4.2.2 Handling

Improper handling of the device has also been a major contributor to the loss of device functionality. In this work two types are devices are used, those based on a *Dayem* bridge constriction and the other based on a SNS (superconductor-normal metal- superconductor) design. The details of the devices will be provided in the relevant chapters. These devices are ESD (electrostatic discharge) sensitive devices, and care must be taken when handling them. Permanent damage such as physical breakage of the weak links may occur on devices subjected to high-energy electrostatic discharges. A shunt or a lower resistance material in the normal state, can be added fabricated in parallel to the device as a means of ESD protection, but general good handling practices are ideal. In order to avoid this the device is grounded starting from the moment that the probes are connected using the grounding switches at the connector terminal. In addition to that, the handling personnel also wears an ESD bracelet minimising human error. It is also important that unnecessary large currents are not applied to the device especially at room temperature. At low temperature, monitoring the maximum applied current is also critical and is controlled by the compliance voltage of the current source. Sudden charge or discharge of current can result in damage to the device. A uniform rate of current ramping up and down is ideal during a measurement. To this end the output is always kept ON at the current source, and the instruments are only manipulated when the device is grounded from connector terminal switches.

2.4.3 Acquisition protocol

Thus far we have considered the necessary instrumentation, proper material, probe set-up, sample preparation and handling guidelines. There are several factors that must be considered during data acquisition on superconducting devices. While this is not the case for the materials used here, the cooling rate of the cryostation can also be pertinent to avoid thermal shock and contamination of the superconductor. We will focus on the specifics data acquisition and guidelines that we followed to ensure the safety of the devices.

Superconducting properties vary with applied magnetic fields, the history of the applied fields, and even the rate of change of the field. It is important to consider the sequences of measurements when interpreting data. In some cases a stabilisation period after a field change is necessary to allow the dissipation of induced eddy currents. For I-V measurements, the determination of the I_c is affected by several factors including the current supply limit, the voltage range required to observe the transition, and the maximum tolerable power dissipation in the sample to maintain thermal control or to avoid sample damage.

In order to illustrate these aspects of measurement guidelines, Fig. 2.11 illustrates a standard current-voltage data set for a SQUID. Here the current is ramped from -0 mA to 60 mA and then back from 60 mA to 0, scanning a range where two transitions are observable. The first transition (blue) occurs at 41.5 mA as the system transitions from a superconducting to normal state at the critical current I_c, while the second transition occurs at the retrapping current I_r when the system goes from a normal to superconductive state at 12 mA. In principle, the system should be symmetric but due to the direction of the current scan, there is a hysteretic behaviour. The re-trapping current

characterises the system condensing into a superconducting state, which is lower than the I_c because the system needs to diffuse heat to condense. The degree of hysteresis is characterised by the difference between I_c and I_r. The direction of scanning is important and can lead to an incorrect characterisation of the I_c.

The discretisation scheme used to acquire the data can be detrimental in isolating the transition. The step sizes in the transition region must be fine, while in the trivial portion of the scan (green), larger step sizes can be taken. This is implemented in the data acquisition scheme by separating the trivial and non-trivial portions of the data sets by defining these two current application regions. There are also many different ways to ramp the current, namely linear, step or pulsed ramp. In general, a step ramp is ideal because it gives the system time to stabilise upon the application of current before a measurement is taken. It is also important to ramp the current slowly for ESD sensitive devices as sudden large currents can damage the device.

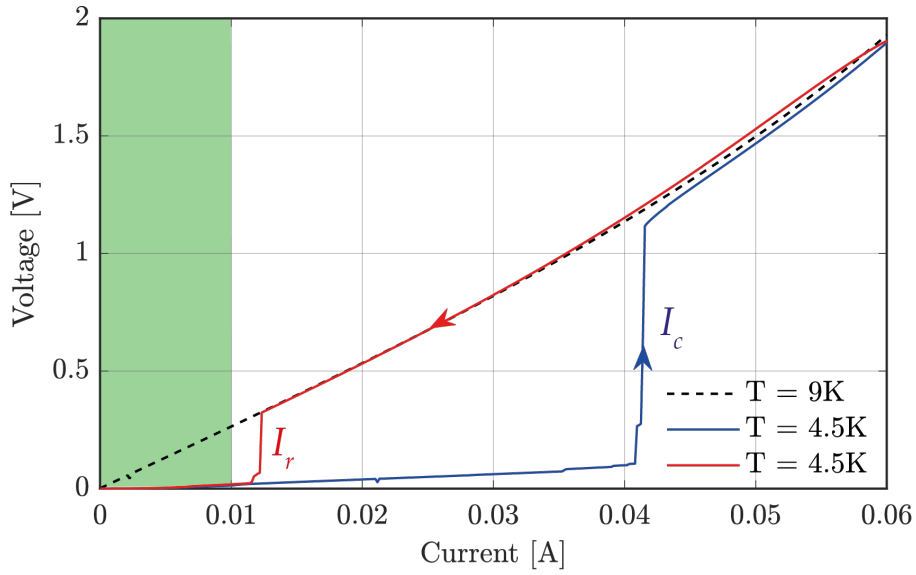

Figure 2.11: **Critical transition measurements.** A standard I-V measurement for a superconducting device is shown. The acquisition is performed by applying a current from 0 to 60 mA and then from 60 mA to 0, as indicated by the arrows. The transition from super conduction to normal behaviour at the critical current I_c and the transition from normal to super conduction is shown in blue at the retrapping current I_r. The green area illustrates the *fast* acquisition regime which is outside of our region of interest.

2.5 Conclusion

In this chapter, the various experimental methods, techniques, equipment, instruments and tools required for the work produced in this thesis are detailed. The fundamental technique of magneto-optical imaging, key to visualising single vortices in superconductive systems, was presented. A thorough understanding of the resolution limiting parameters of the imaging technique is important. Since the goal of this project integration of optical techniques to drive Josephson transport, the current resolution of MOI is a limiting factor. In the subsequent chapter we present the integration of a solid immersion lens (SIL) to address the problem of resolution. Details of the transport measurement were also outlined, focusing on protocols and guidelines that are integral in the measurement and safety of superconductive devices. The final product is the integration the SIL integrated MOI, optical tweezers technique, and transport measurements to allow the simultaneous visualisation and manipulation of single vortices in superconducting devices to drive the system's behaviour.

Bibliography

[1] H. O. McMahon & W. E. Gifford. A New Low-Temperature Gas Expansion Cycle part I. *Advances in Cryo. Eng.*, 5, 1960.

[2] A. T. A. M. de Waele. Basic Operation of Cryocoolers and Related Thermal Machines. *Journal of Low Temperature Physics*, 164, 2011.

[3] U. Essmann & H. Träuble. The direct observation of individual flux lines in type II superconductors. *Physics Letters A*, 24, 1967.

[4] K. Harada, T. Matsuda, J. Bonevich, M. Igarashi, S. Kondo, G. Pozzi, U. Kawabe & A. Tonomura. Real-time observation of vortex lattices in a superconductor by electron microscopy. *Nature*, 360, 1992.

[5] J. E. Bonevich, K. Harada, T. Matsuda, H. Kasai, T. Yoshida, G. Pozzi & A. Tonomura. Electron holography observation of vortex lattices in a superconductor. *Physical Review Letters*, 70, 1993.

[6] P. A. Midgley & R. E. Dunin-Borkowski. Electron tomography and holography in materials science. *Nature Materials*, 8, 2009.

[7] O. Kazakova, R. Puttock, C. Barton, H. Corte-León, M. Jaafar, V. Neu & A. Asenjo. Frontiers of magnetic force microscopy. *Journal of Applied Physics*, 125, 02 2019.

[8] F. S. Wells, A. V. Pan, X. R. Wang, S. A. Fedoseev & H. Hilgenkamp. Analysis of low-field isotropic vortex glass containing vortex groups in $YBa_2Cu_3O_{7-x}$ thin films visualized by scanning SQUID microscopy. *Scientific Reports*, 5, 8 2015.

[9] Y. Schlussel, T. Lenz, D. Rohner, Y. Bar-Haim, L. Bougas, D. Groswasser, M. Kieschnick, E. Rozenberg, L. Thiel, A. Waxman, J. Meijer, P. Maletinsky, D. Budker, & R. Folman. Wide-Field Imaging of Superconductor Vortices with Electron Spins in Diamond. *Pysical Review Applied*, 10, 2018.

[10] P. E. Goa, H. Harald, M. Baziljevich, E. Il'yashenko, P. L. Gammel & T. H. Johansen. Real-time magneto-optical imaging of vortices in superconducting $NbSe_2$. *Superconductor Science and Technology*, 14, 09 2001.

[11] S. J. Bending. Local magnetic probes of superconductors. *Advances in Physics*, 48, 1999.

[12] J. R. Kirtley, L. Paulius, A. J. Rosenberg, J. C. Palmstrom, C. M. Holland, E. M. Spanton, D. Schiessl, C. L. Jermain, J. Gibbons, Y.-K.-K. Fung, M. E. Huber, D. C. Ralph, M. B. Ketchen, G. W. Gibson & K. A. Moler. Scanning SQUID susceptometers with sub-micron spatial resolution. *Review of Scientific Instruments*, 87, 09 2016.

[13] D. Golubchik, E. Polturak, G. Koren & S. G. Lipson. A high resolution magneto-optical system for imaging of individual magnetic flux quanta. *Optics Express*, 17, 2009.

[14] A. Sommerfeld. *Optics : Vol:IV*. Academic Press, 1964.

[15] H. Becquerel. Sur une interprétation appligarle au phénomène de faraday et au phénomène de zeeman. *J. Phys. Theor. Appl.*, 6, 1897.

[16] H. Habermeier. Paving the way for the success of magneto-optics. In T. H. Johansen & D. V. Shantsev, editor, *Magneto-Optical Imaging. NATO Science Series* (*Series II: Mathematics, Physics and Chemistry*), volume 142. Springer, Dordrecht, 2004.

[17] P. B. Alers. Structure of the Intermediate State in Superconducting Lead. *Physical Review*, 105, 01 1957.

[18] L. E. Helseth, A. G. Solovyev, R. W. Hansen, E. I. Il'yashenko, M. Baziljevich & T. H.Johansen. Faraday rotation and sensitivity of (100) bismuth-substituted ferrite garnet films. *Physical Review B*, 66, 2002.

[19] M.R. Koblischka & R.J. Wijngaarden. Magneto-optical investigations of superconductors. *Superconductor Science and Technology*, 8, 1995.

[20] Mohammad Nur-E-Alam, Mikhail Vasiliev & Kamal Alameh. Optical constants of rare-earth substituted amorphous oxide-mix-based layers deposited to enable synthesis of magneto-optic garnets. *Optical Materials*, 98, 2019.

[21] W. Magrini. *Manipulation optique de vortex d'Abrikosov individuels*. PhD thesis, University of Bordeaux, 2017.

[22] A. Rochet. *Manipulation optique de vortex d'Abrikosov individuels dans les supraconducteurs et applications*. PhD thesis, University of Bordeaux, 2019.

[23] A. Polyanskii; V. Beilin; M. Feldmann; M. Roth M; E. Hellstrom; D. Larbalestier. Magneto-optical investigation of superconducting materials. In T. H. Johansen; D. V. Shantsev, editor, *Magneto-Optical Imaging. NATO Science Series* (*Series II: Mathematics, Physics and Chemistry*), volume 142. Springer, Dordrecht, 2004.

[24] H. Kirchner. A high-resolution magneto-optical process to investigate the kinematics of magnetic structures in superconductors. *physica status solidi* (*a*), 4, 02 1971.

[25] S. Flament, D. W. Bloyet, C. Cordier, L. Méchin & C. Gunther. Magneto Optical Imaging of Vortex Penetration in Patterned YBCO Thin Film Near Tc. In T. H. Johansen; D. V. Shantsev, editor, *Magneto-Optical Imaging. NATO Science Series* (*Series II: Mathematics, Physics and Chemistry*), volume 142. Springer, Dordrecht, 2004.

[26] I. A. Sadovskyy, A. E. Koshelev, W. Kwok, U. Welp & Andreas Glatz. Targeted evolution of pinning landscapes for large superconducting critical currents. *PNAS*, 21, 2019.

[27] T. Ozaki, L. Wu, C. Zhang, J. Jaroszynski, W. Si, J. Zhou, Y. Zhu & Q. Li. A route for a strong increase of critical current in nanostrained iron-based superconductors. *Nature Communications*, 7, 2016.

[28] S. Ishida, A. Iyo, H. Ogino, H. Eisaki, N. Takeshita, K. Kawashima, K. Yanagisawa, Y. Kobayashi, K. Kimoto, H. Abe, M. Imai, J. Shimoyama & Michael Eisterer. Unique defect structure and advantageous vortex pinning properties in superconducting $CaKFe_4As_4$. *npj Quantum Materials*, 4, 2019.

[29] P. E. Goa, H. Hauglin, Å. A. F. Olsen, D. Shantsev & T. H. Johansen. Manipulation of vortices by magnetic domain walls. *Applied Physics Letters*, 82, 2003.

[30] O. M. Auslaender, L. Luan, E. W. J. Straver, J. E. Hoffman, N. C. Koshnick, E. Zeldov, D. A. Bonn, R. Liang, W. N. Hardy & K. A. Moler. Mechanics of individual isolated vortices in a cuprate superconductor. *Nature Physics*, 5, 2008.

[31] E. W. J. Straver, J. E. Hoffman, O. M. Auslaender, D. Rugar & K. A. Moler. Controlled manipulation of individual vortices in a superconductor. *Applied Physics Letters*, 93, 2008.

[32] B. W. Gardner, J. C. Wynn, D. A. Bonn; R. Liang, W. N. Hardy, J. R. Kirtley, V. G. Kogan & K. A. Moler. Manipulation of single vortices in $YBa_2Cu_3O_{6.354}$ with a locally applied magnetic field. *Applied Physics Letters*, 80, 2002.

[33] A. Kremen, S. Wissberg, N. Haham, E. Persky, Y. Frenkel & Beena Kalisky. Mechanical Control of Individual Superconducting Vortices. *Nano Letters*, 16, 2016.

[34] J.-Yi Ge, V. N. Gladilin, J. Tempere, C. Xue, J. T. Devreese, J. Van de Vondel, Y. Zhou & V. V. Moshchalkov . Nanoscale assembly of superconducting vortices with scanning tunnelling microscope tip. *Nature Communications*, 7, 2016.

[35] L. Embon, Y. Anahory, A. Suhov, D. Halbertal, J. Cuppens, A. Yakovenko, A. Uri, Y. Myasoedov, M. L. Rappaport, M. E. Huber, A. Gurevich & E. Zeldov. Mechanical Control of Individual Superconducting Vortices. *Scientific Reports*, 5, 2015.

[36] T. Golod; A. Iovan; V. M. Krasnov. Single abrikosov vortices as quantized information bits. *Nature Communications*, 6, 10 2015.

[37] I. S. Veshchunov, W. Magrini, S. V. Mironov, A. G. Godin, J. -B. Trebbia, A. I. Buzdin, Ph. Tamarat & B. Lounis. Optical manipulation of single flux quanta. *Nature Communications*, 7, 2016.

[38] A. Rochet, V. Vadimov, W. Magrini, S. Thakur, J. -B. Trebbia, A. Melnikov, A. Buzdin, Ph. Tamarat & B. Lounis. On-Demand Optical Generation of Single Flux Quanta. *Nano Letters*, 9, 2020.

[39] R. P. Huebener & A. Seher. Nernst Effect and Flux Flow in Superconductors. I. Niobium. *Physical Review*, 181, 1969.

Chapter 3

Solid immersion magneto-optical imaging

As a technique for observing magnetic flux structures, magneto-optical imaging has several advantages, including imaging speed, relatively simple implementation and compatibility with other optical techniques. However, the major drawback of this technique is the low spatial resolution. Currently, MOI is insufficient in its resolution to image single vortices on the scale of Josephson junction devices, therefore, the problem of spatial resolution must be addressed.

The resolution of an optical system is fundamentally limited by diffraction. The maximum resolution is dictated by $0.61\lambda/n\sin\alpha$, where λ is the wavelength of light, and $NA = n\sin\alpha$ is the numerical aperture of the imaging system with n being the refractive index of the medium and α is the half angle of the collection cone. Considering our light source filtered at wavelength $\lambda = 549$ nm and a NA of 0.215 in air (n=1), a diffraction-limited resolution of $\sim$1.558 μm is expected. MO indicators like bismuth (Bi:LuIG) and yttrium (YIG) based ferrite garnets have been used to achieve a resolution of 1.3 μm [1, 2], with the use of a larger NA. The resolution is limited to the micron scale due to factors that stem from the methodology of technique itself. The magnetic flux of a vortex is imaged using the Faraday effect by integrating the rotation of light polarisation over the thickness of a MO indicator placed on top of the superconductor. Since the indicator is pressed on top of the superconductor, the presence of an air gap at the interface leads to broadening of the MO signal. This is due to fast divergence of the magnetic field emanating from the vortex above the surface of the superconductor. This minimises the effective Faraday rotation as the AV magnetic field doesn't end up penetrating the indicator. A secondary factor that results in reduced imaging quality stems from the indicators having a high-refractive index. This results in a significant amount of MO signal being lost as the exiting light either suffers total internal reflection or is refracted out of the collection cone as it traverses back from the high-refractive index garnet into air. It is estimated only $1/2n^2$ or $\sim 13\%$ of photons, where $n = 1.97$ is the refractive index of the GGG, leave the surface [3]. Consequently the information in the marginal rays is lost and we acquire a reduced MO signal, affecting the speed and contrast of the vortex image. Using a high-NA objective can help collect more light to reduces the optical losses but this introduces severe aberrations and depolarisation effects that will reduce the imaging quality as the technique is sensitivity to polarisation

distortions. Therefore, optimal conditions with respect to indicator optical properties and NA must be found to obtain the best resolution, contrast and speed.

To eliminate the problem of the air gap, it has been proposed to directly deposit an indicator on the film as demonstrated with EuSe, leading to the current lowest MOI vortex resolution of 800 nm [4]. Fabricating thin superconductor films on ferrite garnets is not trivial due to severe lattice mismatch of the two compounds. In general, the method of immersion microscopy is a technique that is used to increase the resolving power of a microscope. This can be achieved by introducing a high-refractive index medium between the sample and collection lens or objective, which shrinks the wavelength of light by a factor of the refractive index, enhancing the effective NA. Use of a high-refractive index oil is a common means of altering the intermediate medium. We can implement this methodology in our system in a novel manner by introducing a high-refractive index solid immersion lens (SIL) placed on top of the MO indicator/superconductor structure. We can also address the optical losses due to the high-refractive index interface by using the SIL. This photon extraction problem is similarly remedied using a SIL in several systems where light must be collected from quantum dots grown in a high-refractive index substrate [5, 3]. The sphercity and the high-refractive index of the SIL works to effectively improve the numerical aperture and collection efficiency of the system [6, 7].

In this chapter we present the SIL integrated MOI technique implemented to improve the resolution of single vortex imaging. Rather than trying to optimise the MO indicator properties or attempt difficult deposition processes, we propose to address the fundamental optical limitations by coupling a Bi:LuIG/GGG indicator to a refractive index matched SIL. The geometry of the lens, specifically the curved dielectric surface combined with its high-refractive index enhances the NA by refracting the light into a suitable collection mode, leading to an improved optical resolution and faster imaging speed. A detailed examination of the advantages, disadvantages and limitations of the two SIL configurations, namely hemisphere and super-hemisphere, are outlined. Following that, the effective super-SIL for MOI is characterised. We present the enhanced resolving power of the SIL-MOI system, along with numerical simulations analysing aberrations and potential configurations optimising the resolution and contrast.

3.1 Solid immersion lens (SIL)

SILs are truncated dielectric spheres made from high-refractive index materials. The concept of the SIL originates from the theory of Born and Wolf [8], which states that light can be focused aberration-free at only two points within a high-refractive index sphere. These focal points are known as the *aplanatic* points and are exploited by two distinct geometries, namely the hemisphere (hSIL), and the super-hemisphere (sSIL) or *Weierstrass* configuration. SILs were originally implemented in optical microscopes to achieve higher optical resolutions [6], and have subsequently been used in quantum optics to improve light extraction efficiency of single photon sources, e.g., quantum dots embedded in high-refractive index materials [3, 5]. The SIL will be similarly utilised in enhancing the MOI of single vortices, focusing on the resolution and light collection efficiency. In this section the two SIL configurations are presented, focusing on the advantages and limitations, as each configuration finds its use in a specific applications.

3.1.1 Hemisphere

A hemispherical SIL (hSIL) is a truncated half sphere of radius r and height h, illustrated in Fig. 3.1. In practice $h \neq r$, since the polishing process used to truncate the sphere introduces a deviation of h from r. The object to be imaged is placed directly under the lens. The center of the object or the object plane S coincides with the coupling lens' virtual image plane S', which has a focal length of f_0. This is due to the fact that with a long working distance objective light rays always enter (leave) the hemisphere along its radial normal with negligible refraction, $\theta_i \approx \theta_r$.

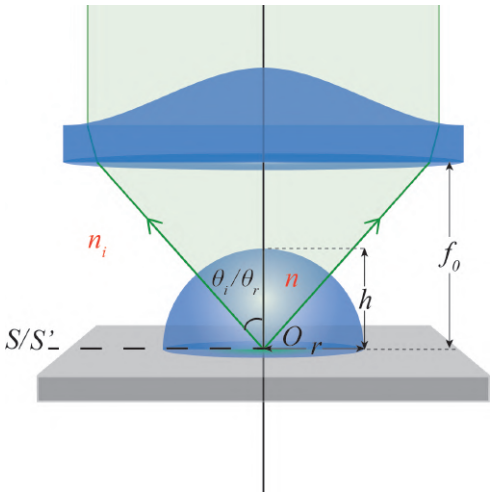

Figure 3.1: **Hemisphere SIL (hSIL).** Hemispherical solid immersion lens with a radius r and height h. The object S and image S' plane coincide at the bottom of the lens on the optical axis at point O.

The transverse magnification M_{hSIL} of the hSIL can be simply derived by considering the Abbe *sine* condition which is given by

$$\frac{\Delta x}{\Delta x'} = \frac{n_i \sin(\theta_i)}{n \sin(\theta_r)} \tag{3.1}$$

where Δx and $\Delta x'$ are the transverse sizes of the object and the image, respectively. While $n \sin(\theta_r)$ and $n_i \sin(\theta_i)$ correspond to the numerical apertures on the object and image side, respectively. In the case of the hSIL, since $\sin(\theta_r) = \sin(\theta_i)$ and $n_i = 1$, the transverse image magnification factor is given by $\frac{\Delta x'}{\Delta x}$, which is equal to n, the index of refraction of the hSIL. Thus, $M_{\text{hSIL}} = M_0 \times n$. Similarly, the maximum achievable enhancement in NA is also $NA_{\text{eff}} = NA_0 \times n$. Therefore, to maximise the capability of the hSIL, a high NA_0 coupling lens is required.

By calculating the wave aberrations within the SIL system, we can obtain analytical expressions for aberration tolerances. We will simply present the derived expressions but the details of the calculations are presented in Ref. [9]. By examining the aberrations due to field curvature for the hSIL, a field of view (FOV) can be determined that tolerates a field curvature of $\lambda/4$ resulting in a phase error of $\pi/2$ between the marginal and paraxial rays. The FOV for the hSIL is then given by the relation

$$\Delta d_{\text{max}} = \sqrt{\frac{2r\lambda}{n(n-1)\sin^2(\theta_0)}} \tag{3.2}$$

Here $NA_{\text{air}} = \sin(\theta_0)$ is the numerical aperture of the coupling lens or objective in air. The manufacturing tolerances is comparatively large for the hSIL. If the height of the SIL varies due to any reason, the input beam can still be focused on the correct plane given the variations are less than the axial tolerance Δh_{max}, as such

$$\Delta h_{\text{max}} = \sqrt{\frac{2r\lambda}{n(n-1)\sin^4(\theta_0)}} \tag{3.3}$$

Due to the hSIL's large axial tolerance, this geometry does not have axial chromatic aberrations, as neither the height of the SIL nor the position of the image plane is wavelength dependent [10, 11].

3.1.2 super-Hemisphere (*Weierstrass*)

The super-hemisphere (sSIL) is formed by truncating the sphere with an additional thickness below the center as illustrated in Fig. 3.2. The physical parameters of the SIL now include the additional height $a = \frac{r}{n}$, and the virtual image plane S' is located a distance $l = r + rn$ from the top of the SIL. Consequently, $\theta_r \neq \theta_i$.

Similar to the hSIL, the transverse magnification of the sSIL M_{sSIL} can also be derived by satisfying the Abbe *sine* condition. In this case where the object and virtual image lie in different planes, $\sin(\theta_r) \neq \sin(\theta_i)$. The transverse magnification for the sSIL is shown to increase by a factor of n^2. The NA_{eff} is similarly enhanced by a factor of n^2. However, the maximum achievable NA_{eff} for the sSIL geometry is still a factor of n. This limit exists because the input beam must be incident on the surface of the SIL, above the sphere's center where $\theta_r < \pi/2$ is imposed. Thus the maximum angle of incidence θ_i is given by $\sin\theta_i = 1/n$ and NA_{eff} is limited to n [11].

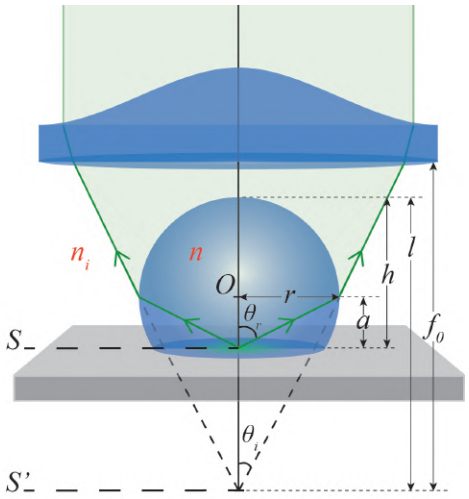

Figure 3.2: **super-Hemisphere SIL (sSIL).** A super-Hemisphere requires an additional thickness a for a total SIL height h. The object S and virtual image S' planes appear at the bottom of the SIL and a distance l from the top of the SIL, respectively.

A key advantage of the sSIL is that due to the $NA_{\text{eff}} = n$ limit, a high resolution can be achieved with a low $NA_0 = 1/n$ coupling lens. However, the sSIL is disadvantageous with respect to longitudinal chromatic aberrations because both the total height $(h+a)$ of the SIL and the position of the image plane are dependent on n, and SIL materials can be highly dispersive. The chromatic aberrations can be eliminated or balanced by reducing the size of the SIL, using a narrow band pass filter, applying a diffractive element, or by choosing a suitable combination of SILs i.e. diverging and converging lenses, or glasses with different refractive indices [10, 12].

With similar constraints of an allowed field curvature of $\lambda/4$, the acceptable tolerance in height variation of the sSIL is given by

$$\Delta h_{\text{max}} = \frac{n}{n^2 - 1} \cdot \frac{\lambda}{2 \sin^2 \theta_0}, \tag{3.4}$$

Since the tolerance tends to be very tight, it can be moderately compensated for with the axial position of the coupling lens which has a tolerance of $n^3 \cdot \Delta h_{\text{max}}$. The FOV for the sSIL configuration is equivalent to the case of the hSIL (Eq. 3.2).

Given that microscope objectives are subjected to non-negligible mechanical strains and phase changes at cryogenic temperatures, performing low temperature imaging with a low NA aspherical lens coupled to a SIL is a powerful tool to increase the effective NA of an optical system.

3.2 SIL integrated MOI

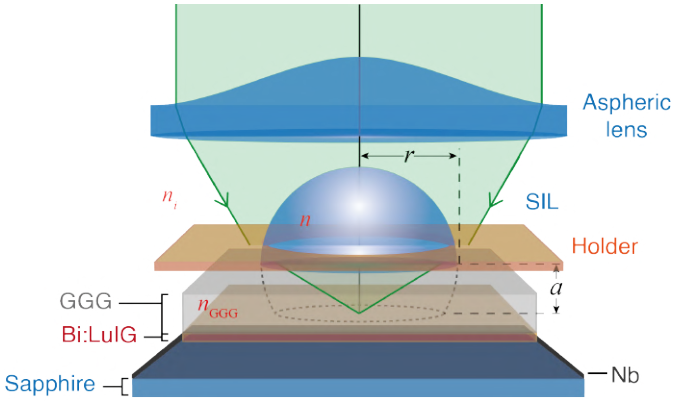

Figure 3.3: **Effective sSIL.** A hemisphere lens imposed on the MO indicator creates an effective sSIL geometry. A holder is used to maintain the SIL and indicator.

In our SIL integrated MOI system we use a modified sSIL configuration, since the flux structures to be imaged do not lie directly under the lens, but below the MO indicator at the superconductor surface. In this geometry the GGG substrate, which comprises most of the indicator thickness, is utilised as the additional thickness a, seen in Fig. 3.3. The radius r of the SIL is then chosen as a function of a so that the SIL combined with the indicator operates in the sSIL geometry. The measured thickness of the MO indicator is 451 μm and the condition $r = na$ gives a SIL radius of 902 μm. Since commercially available SILs only comes in discrete radii, the requirement is nearly fulfilled with the choice of r = 1 mm. The SIL is a half ball lens made of S-LAH79 glass with a reported radial tolerance of +0/-1.5 μm and a height tolerance of $\pm$50 μm due to the polishing process. The measured height is 1.015 mm. The SIL has a refractive index of 2.011, while GGG has a refractive index of 1.97, both at 549 nm. The implementation of the SIL within the MOI sample is not straightforward since the axial and lateral tolerances for the sSIL geometry can be quite tight. It is then important to characterise the SIL integrated sample to understand the limitations of the set-up, and to optimise it accordingly. Through the course of the study several different SILs were characterised and the lens displaying the best imaging capability was utilised.

3.2.1 Numerical aperture

Since our system is not ideal, characterising the new effective NA is important to understand the limits of our system. A facile method to determine the NA is to image an object that is small relative to the wavelength of light. The image of this pseudo point source reflects the diffraction-limited NA of the imaging system. Here we use gold nanoparticles $\sim$ 100 nm as point source scatters to extract the NA for the system. In our set-up there are several aspects that limit the NA. The aspherical lens holder designed for low temperature measurements acts as a back diaphragm to the collection lens. Furthermore, the apparatus used to press the garnet on the superconductor also acts as an aperture, further reducing the NA. We measured the NA using the incoherent light source, and the NA without the SIL is NA_0 = 0.215. With the SIL we obtain an image of $\sim$ 493 nm with a corresponding NA_{SIL} = 0.68, shown in Fig. 3.4. The measured NA falls below the maximum theoretical enhancement of the SIL, $NA_0 \times n^2$= 0.86.

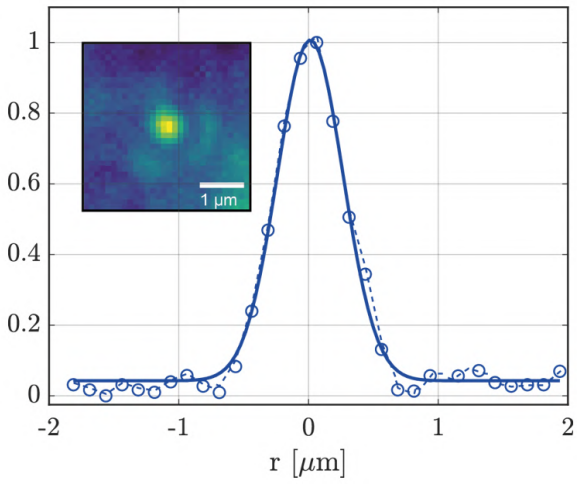

Figure 3.4: **Numerical aperture in effective sSIL system.** Scattering from ∼100 nm gold nanoparticle using incoherent light in wide-field has a spot size of ∼ 493 nm.

3.2.2 Magnification

The two SIL geometries hSIL and sSIL have a n and n^2 enhancement in magnification, respectively. The magnification is characterised by imaging a device with features of known dimensions, shown in Fig. 3.5.

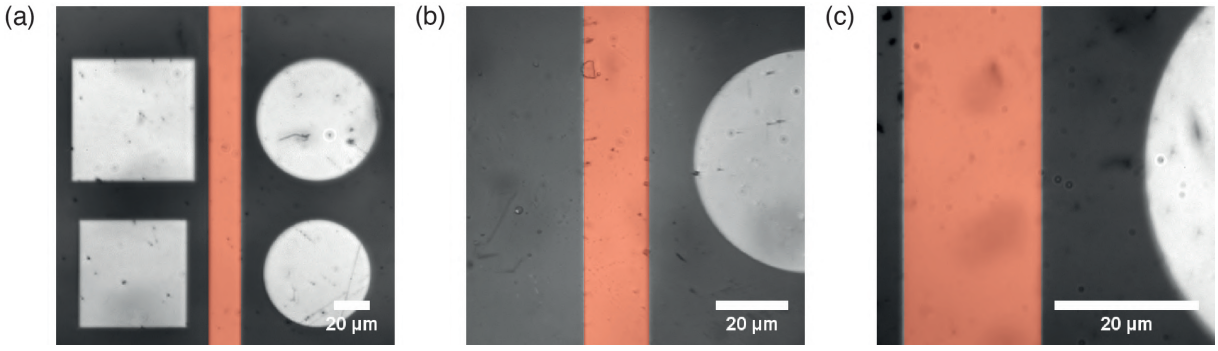

Figure 3.5: **SIL magnification.** Images taken of features on a device. All images show an area of 450 × 450 pixels, with the shaded orange feature having a physical width of 20 μm. (**a**) Without the SIL and GGG, (**b**) in the hSIL geometry and (**c**) with the GGG in the sSIL geometry.

The feature taken for the purposes of characterisation is a Nb strip of width 20 μm. The physical size per pixel of the CCD camera is 13 μm. Without the SIL the pixel size is 0.482 μm with a magnification of 27×. To achieve the hemispherical geometry, the SIL is simply placed directly on the sample structure to obtain a magnification of 53× and a pixel size of 0.245 μm. For the sSIL configuration, the SIL is placed on top of GGG to obtain a magnification of 104× and a pixel size of 0.125 μm. Given that $n = 2$, the magnifications for the respective configurations show minimal deviation from the theoretical expectation.

3.2.3 Tolerances

For an ideal sSIL configuration with the parameters of the half-ball lens, the FOV and axial tolerance can be calculated using Eq. 3.2 and 3.4. Using $r = 1$ mm as the radius of the SIL, $\sin\theta_0 = 0.215$ as the numerical aperture of the coupling lens in air, $\lambda = 549$ nm and $n = 2.011$, the FOV is $\sim 77\mu$m, while the axial tolerance is $\Delta h_{max} \sim 4\mu$m. The measured height for the SIL is 1.015 mm, while the MO indicator has a thickness of 451 μm, which gives a total height of $h = 1.466$ mm. There is a 34 μm offset in height which is an order of magnitude larger than the calculated axial tolerance. The tolerance for the axial position of the coupling lens is $n^3 \cdot \Delta h_{\text{max}} \approx 32$ μm, so the offset in height can be compensated for reasonably by moving the lens to an optimal distance. The residual refractive index mismatch between the SIL (2.011) and GGG ($\sim$ 1.97) produces negligible spherical aberrations (Strehl ratio greater than 0.989) and a small longitudinal displacement ($\sim$15 μm) of the imaging plane.

3.2.4 Image acquisition

Since light passed by the analyser comprises primarily of incident light, the Faraday signal lies within this background. The background subtraction scheme, where we take a background image above T_c and subtract it from the image of the vortices below T_c, ensures that the Faraday signal can be isolated. The thermally induced misalignment due to temperature variation can be detrimental in isolating the Faraday signal. However, since the temperature variation is about 6K, the misalignment is negligible. In order to improve the signal-to-noise (SNR) of the images, multiple background images are acquired and averaged.

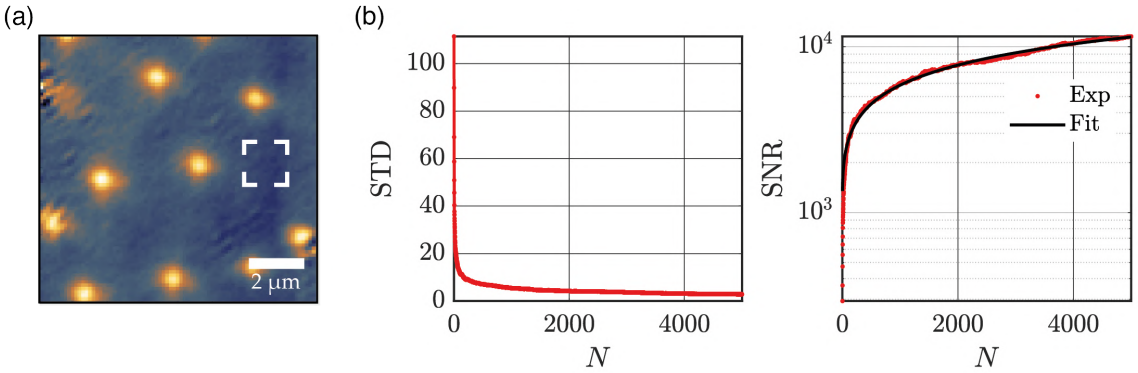

Figure 3.6: **SNR.** (**a**) Vortex image taken with 10000 acquisitions. Box indicates area for background noise analysis. (**b**) The STD and SNR for the background noise with increasing acquisitions.

In order to characterise the optimal number of acquisitions, 10000 images are taken at $T = 10$K, above T_c, for the background. Then at $T = 4.5$K when the vortices have formed 10000 images are acquired. The integration time for each image was 40 ms. Averaging over the 10000 images a background image is produced and subtracted from the vortex image, shown in Fig. 3.6a. The standard deviation (STD) and subsequent SNR, taken in the vortex free area indicated by the white box, is calculated for increasing

acquisition images up to 5000 images. The sample SNR is taken as the ratio of the mean to the standard deviation. The plots in Fig. 3.6b-c. show the evolution of the STD and SNR with increasing acquisition images, respectively. The SNR data is fitted to a power model of the form: $y = aN^b + c$. The fitting parameters were found to be $[a, b, c] = [159.6, 0.489, 1189]$, with the parameter b being in agreement with the expected value of 0.5. In practise, a background of 500 acquisitions provides a vortex image with good SNR.

Given the sufficiently integrated background image, individual vortices can be resolved with sub-second image acquisition times. In Fig. 3.7, a series of single-shot images are acquired with integration times of 40 ms, 200 ms, 400 ms and 1 s, and have SNRs of 0.57, 0.73 , 1.23 and 2.45, respectively. Fast imaging is particularly promising in the view of real-time dynamical studies of vortex-vortex interactions.

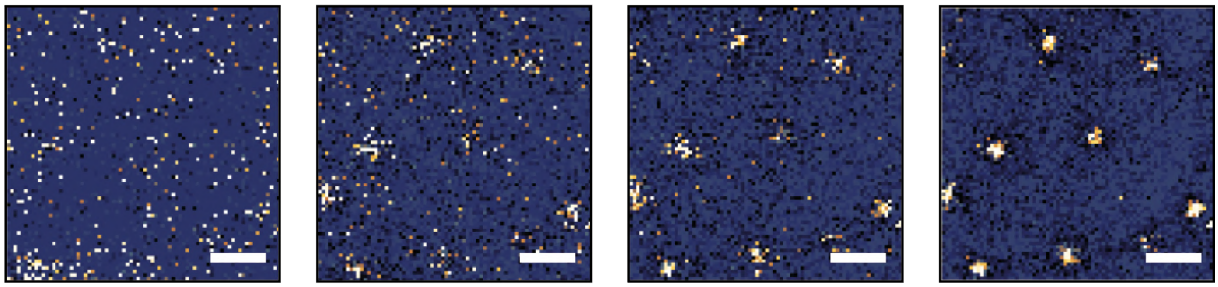

Figure 3.7: **Integration time of single-shot images.** Single-shot images taken at 40 ms, 200 ms, 400 ms and 1 s. Individual vortices can be resolved at a sub-second scale with good SNR. The scale bars are 2 μm.

3.3 Experimental results

Imaging of the vortices is performed at 4.5K. At this temperature, vortices have a physical size of ∼100 nm. Since this study is based on comparing the two cases of MOI namely without and with the SIL, all data posed for comparison is taken under the same conditions.

3.3.1 FWHM

Analysing the resolution of the system, Fig. 3.8a-b show MOI images of a spontaneous vortex distribution for an external magnetic field of 30 μT. The vortices are randomly distributed as dictated by the pinning landscape in the Nb film. For the case without the SIL (Fig. 3.8a), we obtain a full width half maximum (FWHM) of 1.7 μm (Fig. 3.8c), characteristic of the classical method, and consistent with the diffraction-limited spot size for an optical system with $NA_0 \sim 0.2$. The addition of the SIL drastically reduces the vortex size (Fig. 3.8b) with a measured FWHM of 583 nm (Fig. 3.8c), three times less than the case without the SIL. As discussed in the context of tolerances, the dimensional and refractive index mismatches should not significantly affect the imaging quality, but it will contribute to some deviation from the ideal case. In general there is always some space at the indicator-superconductor interface which contributes to loss of resolution. This coupled with the mismatch induced focusing of the input light at a different plane rather than at the superconductor surface, will cause a broadening of the PSF [11].

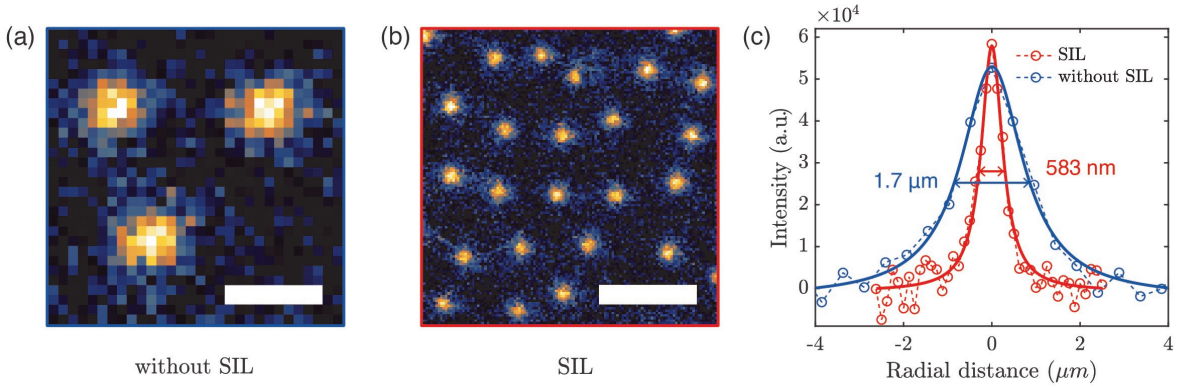

Figure 3.8: **FWHM.** (a) Single vortex imaging using the classic MOI method. (b) Single vortex imaging using the SIL integrated MOI method. (c) Lorentzian fit for the smallest imaged vortices for the two configurations. The vortices are resolved with a FWHM of 1.7 μm and 583 nm without and with the SIL, respectively. The scale bars are 5 μm.

The enhancement due to the SIL is most obvious in the case of high concentration of vortices as shown in Fig. 3.9. While it is impossible to distinguish two vortices with the classical MOI after a certain external magnetic field, the SIL allows us to distinctly resolve individual vortices up to a concentration where the classical method will simply show a saturated FOV.

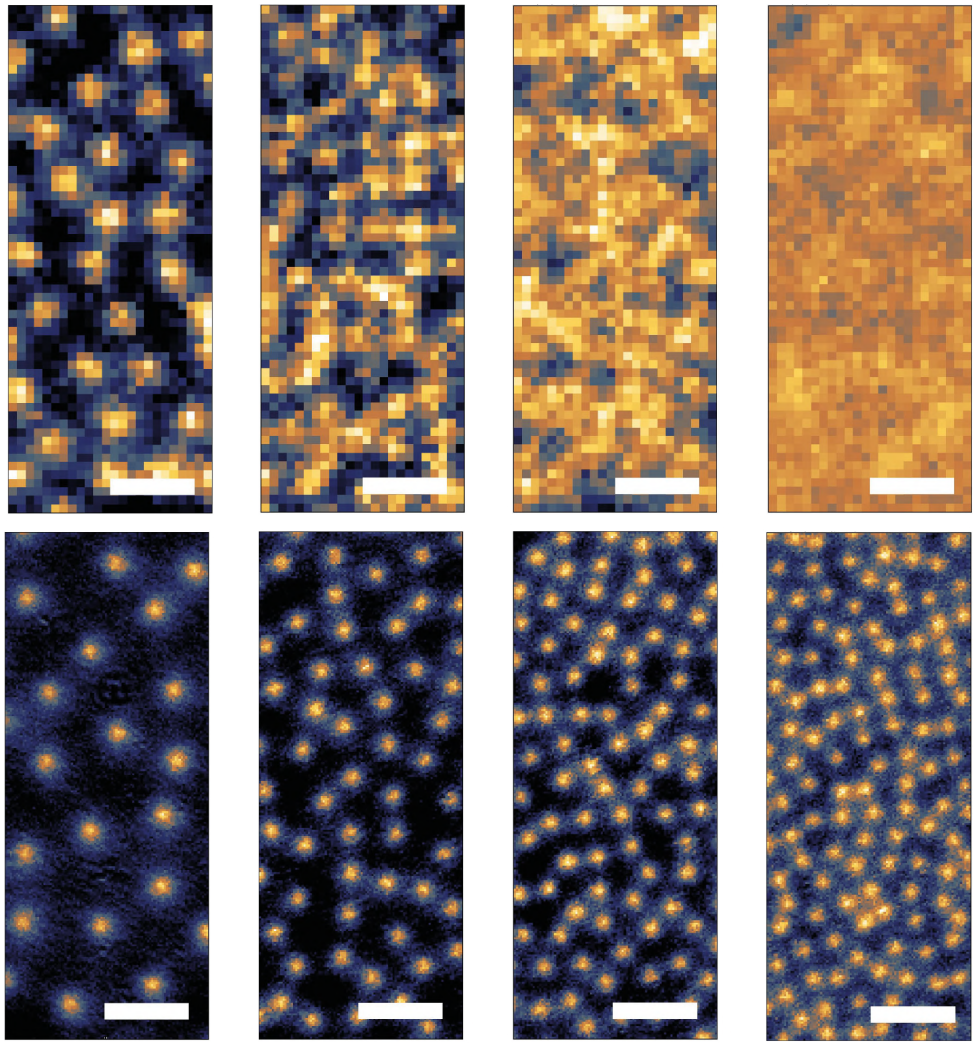

Figure 3.9: **B-field dependent single vortex imaging.** Vortices imaged in a magnetic field of B_{app} = 120 to 710 μT without (top) and with (bottom) the SIL. With the increased resolution previously unresolvable vortices are distinctly isolated. The scale bars are 5 μm.

3.3.2 Polariser extinction

To characterise the quality of the MOI system, we perform a quantitative analysis of the normalised contrast. In Fig. 3.10 the normalised contrast is averaged over ~ 20 vortices in a sample area, with the error bars indicating the variations in amplitude within the data set. MOI contrast is directly linked to the quality of the linear polarisation of light given by the extinction ratio ϵ, between the two cross-polarisers. The measured extinction ratios are $\epsilon = 5{\times}10^{-3}$ and $\epsilon = 4.4{\times}10^{-2}$ for the case without and with the SIL, respectively. In Fig. 3.10 we sweep the offset angle ϕ and plot the resulting normalised contrast for both cases, without and with the SIL.

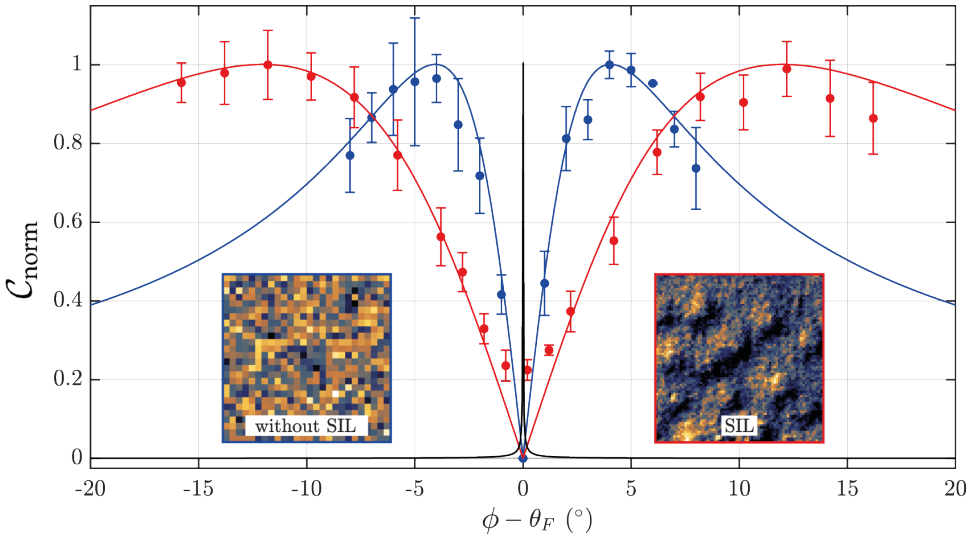

Figure 3.10: **Offset angle contrast.** The averaged, normalised vortex signal contrast as a function of the analyser offset angle for the case without (blue) and with the SIL (red). The error bars indicate signal variations between the individual vortices in the data set. (Inset) Images shown are taken at the cross position, $(\phi - \theta_F) = 0$. The fits are based on the contrast formula in Eq. 3.5. The black line shows the contrast for the case of perfect extinction, $\epsilon \approx 0$.

The data is fitted using the contrast relation [13]

$$\mathcal{C}_{\text{norm}} = \frac{2|\phi - \theta_F|\sqrt{\epsilon}}{(\phi - \theta_F)^2 + \epsilon} \tag{3.5}$$

where $\theta_F \sim 5$ mrad is the Faraday rotation acquired by the linearly polarised light after the double pass through the indicator. The sweep data shows maximal contrast for the two configurations at $(\phi - \theta_F) = \pm 4°$ and $\pm 12°$, for the case without and with the SIL, respectively. This coincides with the offset angles obtained with the formula $\pm \sin^{-1}(\sqrt{\epsilon})$. In an ideal system with a zero extinction ratio, the contrast would be maximal, tending to infinity, at $(\phi - \theta_F) = 0$.

Compared to the configuration without the SIL with the aspheric lens alone, the SIL introduces off-axis projections in the linearly polarised light due to an increase in the NA. Consider an incident beam with a EM field linearly polarised in the $\hat{x}-$direction, shown in Fig. 3.11. The light rays in the xz-plane and yz-plane are shown in green and

red, respectively, and the ray at 45deg between these two planes is shown in purple. The EM field vectors before and after the lens are denoted by E_0 and E', respectively. The refracted light rays located in these planes show different projected polarization components. The rays in the yz-plane retain their original polarisation state, while the light rays located in the xz-plane have a longitudinal $z-$ component. The intermediate ray has components in both the $y-$ and $z-$ axes.

Considering the contributions of these projects from all quadrants, leads to a complex interference effect of all the light rays resulting in a different intensity and polarisation distribution at the focus f. The strength of these projected component become greater when the α angle increases [14, 15].

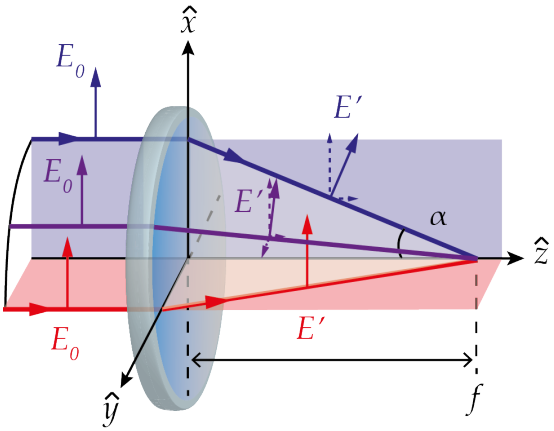

Figure 3.11: **Polarisation in high-NA system.** Focusing linearly polarised light by a high-*NA* lens introduces off-axis projections in the polarisation profile. For MOI, polarisation quality is critical to obtaining image contrast.

This effect is evident in the degradation of extinction with the SIL, also be seen in the inset vortex images in Fig. 3.10, where the image cannot be extinguished at the zero offset angle. Vortices appear as a mix of polarization, half experiencing positive rotation and the other half negative rotation. It reflects non-negligible distortion in the polarisation profile induced by the SIL. This effect is similarly seen in magneto-optic data storage systems, which essentially uses the same principle to store and read data. Degradation of polarisation quality results in errors in the read-out [16].

3.3.3 Effect of numerical aperture

While an increase in NA is conducive to increasing the resolution of an imaging system, in the case of SIL-MOI, this is not as straightforward. An increase in NA inherently results in degradation of polarisation quality as we saw previously, which is critical to the principle of MOI. Additionally, the implementation of the SIL in a sSIL geometry creates tight tolerances for the dimensions of the structure if an ideal enhancement is to be achieved. The analysis thus far has been based on the binary cases of imaging without and with the SIL giving us access to the minimum and maximum NA for SIL-based objective, respectively. In this section the FWHM and contrast are analysed as the NA is varied between the extrema.

The NA is varied by placing a diaphragm on the output beam path at a position corresponding to the Fourier plane, denoted by the NA iris in in Fig. 2.7. By placing a circular optical aperture in a Fourier plane, one can effectively modulate the spatial frequency spectrum. By varying the radius of the aperture one can implement a low-pass filter in *k*-space, transmitting only components with sufficiently low spatial frequencies. The measured radius can be used to calculate the effective numerical aperture of the SIL system. This is similar to modulating the input beam diameter at the entrance pupil of

the aspherical lens.

While vortex sizes of 583 nm and 1.7 μm, with and without the SIL, correspond to the smallest imaged vortices within a sample area, the measurement of FWHM and amplitude as a function of the NA, shown in Fig. 3.12, is obtained for several vortices ($\sim$ 10-30 vortices) averaged over an area. As expected, reduction of the NA corresponds to loss in resolution or PSF broadening. At low NA, deviation from a diffraction limited resolution can be attributed to an air gap and to a misalignment with the optical axis [10]. The SIL/GGG index mismatch and geometrical deviations can contribute further to the loss in resolution, as the deviation from the diffraction limit increases. The sensitivity to the imperfections becomes greater with increasing NA.

The effect of the NA on the vortex imaging contrast is also analysed, shown in Fig. 3.12b. The contrast is given as $\mathcal{C} = (I_{max} - I_{min})/(I_{max} + I_{min})$. Here, I_{max} and I_{min} refers to the maximal and minimal intensities in the vortex images. The data shows an optimal NA around the two data points at 0.39 and 0.53 which gives maximal contrast, while still preserving a reasonable resolution. In comparison, the contrast also does not diminish significantly at $NA = 0.68$, and the high-NA configuration still produces high contrast images. Considering that normalised contrast is proportional to $1/\sqrt{\epsilon}$, we expect to have a contrast three times weaker with the SIL because of its evident depolarising effect. On the other hand, the SIL has a better light collection efficiency due to its enhanced NA. While the classical MOI has a collection angle of $11.5°$, the SIL increases the collection cone up to $20°$. While this simplistic analysis does not account for losses due to internal reflections, a threefold increase in photon flux collection is obtained when using the SIL-based configuration.

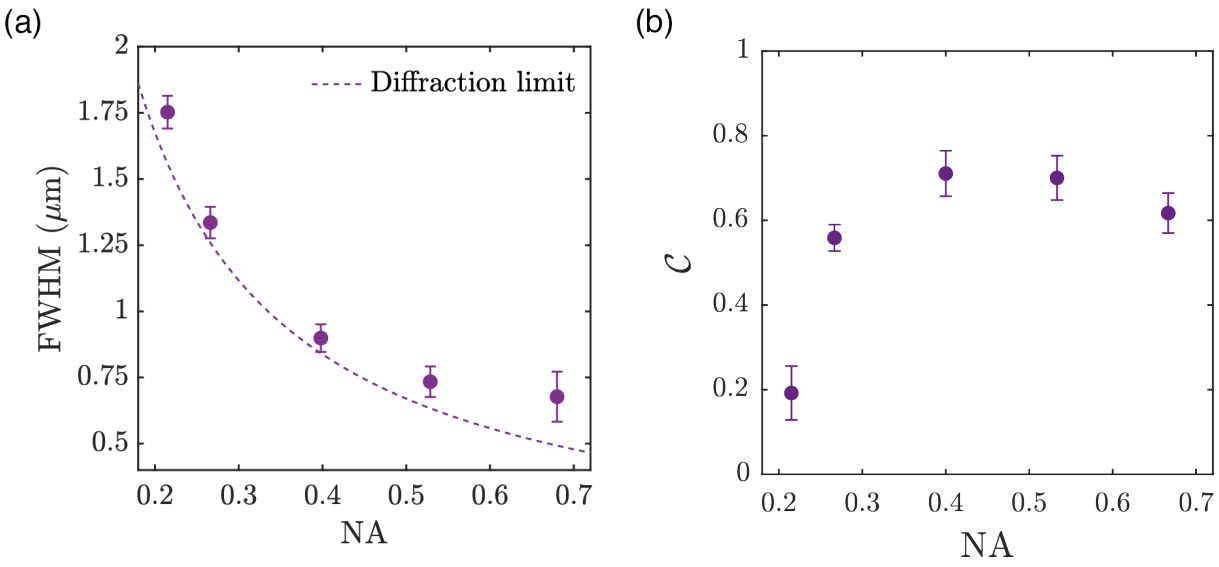

Figure 3.12: NA **dependent FWHM and Contrast.** Error bars translates variations from one vortex to another. (**a**) Vortex FWHM as a function of the effective NA. The diffraction limited FWHM is given by the dashed curve. (**b**) Vortex contrast $\mathcal{C}$ as a function of the effective NA. There is a optimal NA that provides both a reasonable FWHM and contrast.

3.3.4 Source size dependence

The extinction ratio and corresponding vortex image SNR is measured in the SIL configuration as a function of the source diameter, shown in Fig. 3.13. The source diameter corresponds to the diameter of the source iris, refer to Fig. 2.7. With the source iris, we have the capability to control the brightness, profile homogeneity and the size of illumination source.

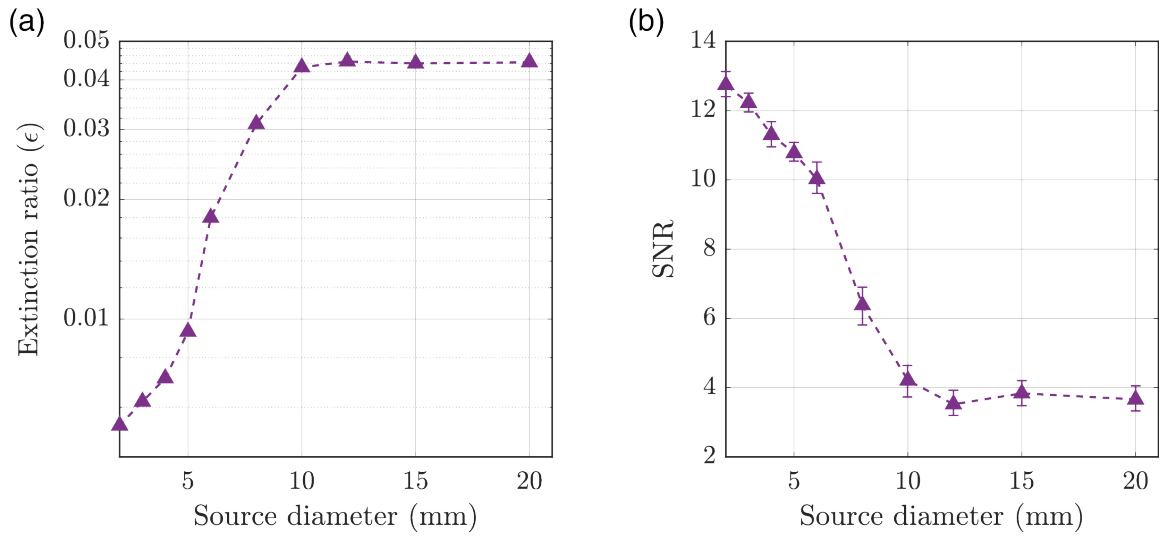

Figure 3.13: **Source diameter dependent SNR.** The source diameter corresponds to the diameter of the source iris. (**a**) The extinction ratio measured in the sSIL configuration as a function of the source diameter. The extinction is constant when the diameter is large, but shows enhancement over an order of magnitude as the diameter is reduced from 10 mm down to 2 mm. (**b**) The SNR is extracted from the vortex images, averaged over ∼30 vortices. Here the SNR is calculated as the ratio of the peak vortex signal and the noise in the background. Error bars correspond to variations of SNR from one vortex to another. The gain in SNR mirrors the enhancement in the extinction ratio.

In the ideal case the illumination is a point source where we transport the image to the back focal plane of the focusing lens to achieve a wide-field illumination. Reducing the size of the source is equivalent to creating a point-like source moving closer to the idealised configuration. Additionally, reducing the size of the iris reduces the polarisation inhomogeneities that are transmitted through the analyser. The extinction quality and consequently the SNR is seen to improve as the source size is reduced below 10 mm down to 2 mm (Fig. 3.13). There is an order of magnitude gain in extinction, with corresponding gain in SNR by a factor ∼3. The enhancement in polarisation quality due to reducing the source diameter would be greater without the SIL, as we remove a critical depolarising optical component. However, a large SNR enhancement can still be attained due to a larger photon collection. The ability to collect more light is particularly important in this case because as the size of the source is reduced, the intensity of the illumination is also reduced, requiring significantly longer acquisition times.

3.4 Numerical simulation

Understanding the contributions to the degradation of imaging quality through the whole vortex imaging setup is crucial to find a trade-off between the signal-to-noise ratio and the acquisition time. There are two main effects leading to deviations of the light polarization from the ideal linear polarization along the optical path. Firstly, the field stemming from a vortex undergoes changes of polarization during its propagation towards the camera. Secondly, in the absence of vortex, the propagation of light from the source to the camera introduces inhomogeneity in the polarization, which degrades the extinction ratio. We simulate these effects using a home made 3D vectorial ray-tracing program. An arbitrary number of rays can be initialised with a selected NA and illumination source diameter. For each surface the program calculates the corresponding intersection points for all rays and subsequently calculates the outgoing rays according to Snell's law of refraction. Furthermore, the polarisation of the outgoing rays' electric field is calculated using the Fresnel coefficients as $E'_s = t_s \cdot E_s$ and $E'_p = t_p \cdot E_p$, where t_s and t_p are the Fresnel amplitude coefficients for s and p polarisations, respectively. Using this formulation optical aberrations occurring at large *NA*s can also be calculated.

3.4.1 Diffraction from a vortex

Due to its very small size, the vortex is treated as a isotropically diffracting point source of light placed at the origin of the coordinate system. The ray trajectories are then calculated moving from the surface of the superconductor, through the garnet experiencing rotation of polarisation, the SIL and finally the aspheric lens. The wavefront error is computed along the optical path towards the camera, and the point spread function (PSF) at the camera plane is obtained from the Fourier transform of the pupil function. The PSF is calculated for the case without the SIL and for the *Weierstrass* configuration with the respective experimental NA of 0.215 and 0.68.

The polarisation is initialised in the x-axis, orthogonal to the ray direction y-axis and the z-axis. The PSFs associated to the intensity components I_x and I_y along the x and y-axes are calculated at the output of the aspheric lens for the case without the SIL (Fig. 3.14 a-b), and with the SIL (Fig. 3.14 c-d). The contribution of I_z is negligibly small compared to the other two axes. In both cases, the aspheric shape of the collecting lens greatly reduces the spherical aberrations and leads to PSFs of the x-polarized field (Fig. 3.14 a-c) very similar to the Airy distribution obtained for a perfect optical system with a circular aperture.

The PSFs for I_y shown in Fig. 3.14 b,d have weak intensities as compared to I_x, a product of the polarisation distortions introduced by light propagation in both configurations. However, for the case of the SIL the I_y component is indeed an order of magnitude larger compared to the case without. In general this is expected as the function of the SIL is to enhance the NA of the optical system, thereby introducing a certain degree of depolarisation.

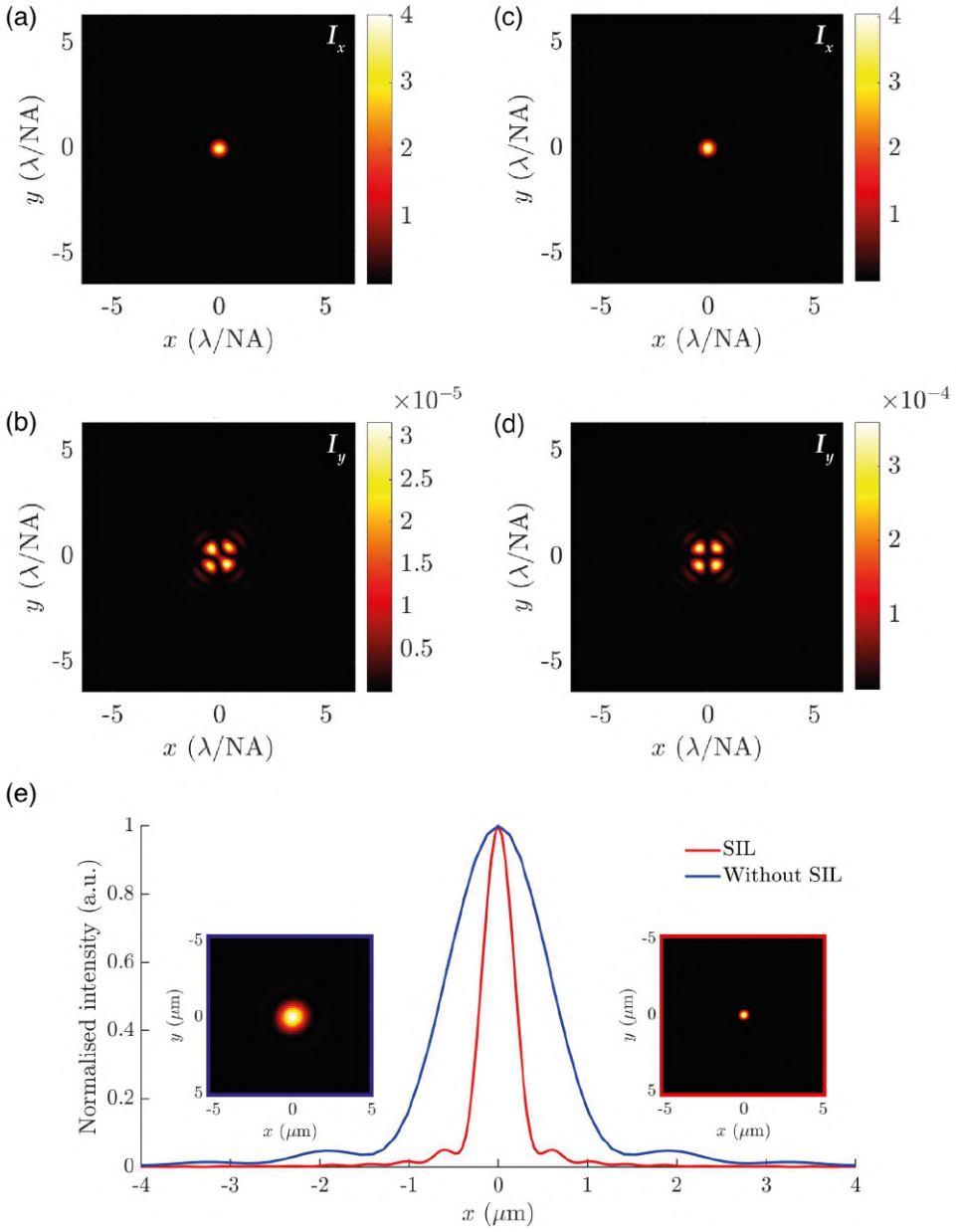

Figure 3.14: **Simulated PSFs.** Contributions of the intensities of individual polarisation directions, namely I_x and I_y, for the case (**a,b**) without the SIL and (**c,d**) with the SIL. The polarisation is intialised along the x-axis. (**e**) Comparison of the PSF for the cases that are accessible in the experiment, i.e. the case without a SIL ($NA = 0.215$) and with a SIL in the *Weierstrass* configuration ($NA = 0.68$). The primary plot shows the distributions for the two cases when integrated along the x-axis with normalised amplitudes, while the inset images visualise the cumulative PSFs.

The experimentally observed image of the vortex is obtained by filtering the light with the analyser, with the experimental offset angles, and taking the projection of the individual PSFs onto the analyser axis. The corresponding image is shown in Fig. 3.14e. The PSF obtained with the analyser is dominated by the contribution of I_x, while the I_y component just adds some residual wings to the distribution. Even with the SIL the

contribution of the I_y component is still four orders of magnitude weaker. This allows us to deduce that the primary reason for loss in resolution in our system does not stem from depolarisation but rather from the usual suspects that contribute to spherical aberrations like the airgap between the indicator and superconductor, and the mismatch between GGG and SIL.

3.4.2 Illumination source

The illumination source, a 3 mm diameter fiber, is modelled by a sum of incoherent, unpolarised and uniformly distributed point sources (100 points). The path from the illumination can be followed in Fig. 2.7. A polariser is placed just after the collimating lens to polarise the electric field along the x-axis. An iris is added afterwards to control the aperture source. This simulation follows the propagation of the field through the SIL system without the presence of a vortex. The three electric field components $(E_{x,y,z})$ are then propagated to the analyser using 10,000 beams launched through the pupil of the system. The fields are then reconstructed and summed incoherently to obtain the intensities $|E_{x,y,z}|^2 = I_x, I_y$ and I_z after the analyser. In the insets of Fig. 3.15, the electric field components are plotted in the case of a single source point.

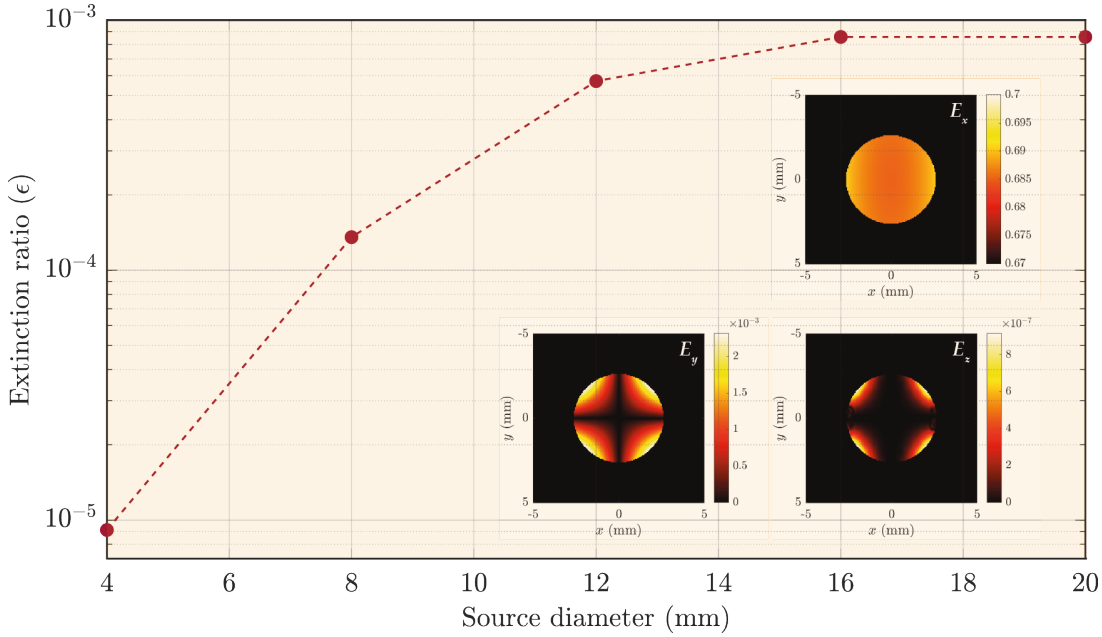

Figure 3.15: **Theoretical contrast.** The extinction ratio is computed in the Weierstrass configuration for various diameters of the source beam. While almost constant at large source apertures, the extinction ratio improves over an order of magnitude as the diameter is reduced from 10 mm down to 2 mm. The inset images show the spatial distribution of the field components along the E_x, E_y and E_z axis associated with the directions of the incident polarization, the orthogonal polarization and the optical propagation axis, respectively.

As expected, the E_y and E_z components are mainly created when propagating the beam through the aspheric lens and the SIL, and take their greatest values at the largest

angles incidence. From these intensity profiles at different diameters, we computed the extinction ratio defined by $\epsilon = \frac{I_y}{I_x}$. Fig. 3.15 shows the evolution of the contrast as a function of the diameter of the source aperture. This resembles the trend observed in Fig. 3.13, albeit the order of magnitude of the extinction ratio appears degraded in the experimental case. A clear degradation of the contrast is obtained when the source diameter is large, with a corresponding decrease of the SNR. Therefore, a compromise must be found between the SNR and the integration time.

3.5 Conclusion

In this chapter we have developed a MOI setup based on a hemispherical SIL operating in the Weierstrass configuration and leading to sub-600 nm optical resolution of single Abrikosov vortices. This represents a three-fold improvement in the resolution with respect to single lens imaging systems. Such performance is combined with a higher efficiency in light collection, which is essential for fast acquisition of vortex images.

Through experimental characterisation and simulations, we are able to understand the limitations of the technique and devise the avenues for improvement of the vortex image quality. Higher contrasts could be achieved using a quasi-point source for aberration-free illumination of the sample. Higher vortex resolutions and faster vortex imaging could also be reached by increasing the effective NA of the SIL, however, care must be taken to ensure that the inherent polarisation distortions in high NA imaging systems is kept to a minimal. As observed from the characterisation data, there exists a region of optimal imaging conditions. Additionally, a thinner indicator and an enlarged SIL holder will both aid the collection of more light, by reducing the absorption thickness and opening up the collection cone.

With our MOI setup it is now possible to perform accurate optical localization and manipulation of single vortices applied to optical operation of Josephson transport, as well as real-time studies of vortex-vortex interactions.

Bibliography

[1] A. J. Qviller. Quantitative magneto-optical imaging with ferrite garnets, 2019.

[2] P. E. Goa, H. Harald, M. Baziljevich, E. Il'yashenko, P. L. Gammel & T. H. Johansen. Real-time magneto-optical imaging of vortices in superconducting $NbSe_2$. *Superconductor Science and Technology*, 14, 09 2001.

[3] W.L. Barnes, G. Björk, J.M. Gérard, P. Jonsson, J.A.E. Wasey, P.T. Worthing & V. Zwiller. Solid-state single photon sources: light collection strategies. *The European Physical Journal D / Atomic, Molecular, Optical and Plasma Physics*, 18, 02 2002.

[4] D. Golubchik, E. Polturak, G. Koren & S. G. Lipson. A high resolution magneto-optical system for imaging of individual magnetic flux quanta. *Optics Express*, 17, 2009.

[5] V. Zwiller, T. Aichele & O. Benson. Quantum optics with single quantum dot devices. *New Journal of Physics*, 6, 07 2004.

[6] Mansfield, S. M. & Kino, G. S. Solid immersion microscope. *Applied Physics Letters*, 57, 1990.

[7] Valéry Zwiller & Gunnar Björk. Improved light extraction from emitters in high refractive index materials using solid immersion lenses. *Journal of Applied Physics*, 92, 2002.

[8] Max Born & Emil Wolf. *Principles of Optics, 7E*. Cambridge University Press, 1999.

[9] Scott Marshall Mansfield. *Solid immersion microscopy*. PhD thesis, Stanford University, 1992.

[10] W. Qiang, L. P. Ghislain & V. B. Elings. Imaging with solid immersion lenses, spatial resolution, and applications. *Proceedings of the IEEE*, 88, 2000.

[11] G. S. Kino, Gordon S. & Y. B. Band. SPIE Proceedings [SPIE Optoelectronics '99 - Integrated Optoelectronic Devices - San Jose, CA (Saturday 23 January 1999)] Optical Pulse and Beam Propagation - Applications and theory of the solid immersion lens. volume 3609, 1999.

[12] L. Wang, M. C. Pitter & Michael G. Somekh. Wide-field high-resolution solid immersion fluorescence microscopy applying an aplanatic solid immersion lens. *Applied Optics*, 49, 2010.

[13] M. Tokunaga, T. Tamegai & T. H. Johansen. Improvement of vortex imaging in magneto-optical technique and Bitter decoration. *Physica C*, 437-438, 2006.

[14] M. Mansuripur. *Classical Optics and its Applications, 2E*. Cambridge University Press, 2009.

[15] Q. Li, I. Ledoux-Rak & N. D. Lai. Influence of incident beam polarization on intensity and polarization distributions of tight focusing spot. *Advanced Device Materials*, 1, 2015.

[16] M. Mansuripur. Effects of high-numerical-aperture focusing on the state of polarization in optical and magneto-optic data storage systems. *Applied Optics*, 30, 1991.

Chapter 4

Optically driven Josephson transport

A Josephson junction (JJ) is the constituent building block of all superconducting electronics. It is formed by a superconductor-normal-superconductor structure which relies on the tunnelling of a supercurrent (described by a macroscopic quantum wavefunction) across the junction barrier. Its quantum state and the throughput current are completely described by the controllable phase difference ($\Delta\theta = \theta_2 - \theta_1$) developed across the barrier as described by the current-phase relation. JJs are an attractive component in quantum electronics due to their high non-linearity and long coherence times for quantum states. Additionally, the presence of an Abrikosov vortex which carries a flux quantum and a circulating supercurrent around the vortex core induces a 2π phase rotation in the superconducting condensate on the scale of the penetration depth away from the vortex core. It has been shown that the presence of an AV in proximity to the junction barrier perturbs the profile of the Josephson phase, thus affecting the ground state [1, 2, 3]. In the simple geometry of a planar JJ with a AV trapped in the electrodes, the vortex currents induce a $0 \rightarrow \pi$ phase difference with the variation of the vortex-barrier distance. This creates a possibility of developing superconducting circuits based on AV driven Josephson transport.

Modern large scale superconducting circuits are based on *rapid single flux quantum* logic, which uses a SQUID as its fundamental building component. The information is stored in the form of a magnetic flux quantum which is read as *single flux quantum* voltage pulses [4]. In comparison, using an AV driven JJ as the fundamental unit of the circuit presents the advantage of using only one JJ, which has the potential for higher density superconducting circuits. Moreover, AVs can be controllably manipulated by magnetic fields [3], current [5, 6] or light [2, 7]. The latter method provides a greater degree of freedom in precise vortex manipulation, pinning [7] and generation [8], giving complete scalable optical control of the device. In addition to that, we also attempt a simple patterning technique to optically create a weak link to shift the operation of the device into the Josephson regime [9].

In this chapter we show that with the application of several previously developed methods of high-resolution MOI and optical vortex manipulation, Josephson transport can be optically modulated in a large dynamic range.

4.1 Light controlled Josephson characteristics

4.1.1 Light-superconductor interaction

The superconducting properties are highly sensitive to external perturbations like electrons, phonons, light and other particles. In this section we delve into the effect of incident light on a superconductor. In our case we are dealing with electromagnetic waves in the visible spectrum where the energy (~ 2eV) is greater than the energy gap 2Δ of a superconductor. As elaborated in Sec. 1.3.2, there is an energy gap within the density of states that separates the condensed ground state from the excited or unpaired state, shown in Fig. 1.6, which is on the order of $\Delta \sim 10^{-3}$ eV.

In Fig. 4.1, an optical photon ($h\nu$) illuminating a superconductor will destroy Cooper pairs, creating "high" energy electrons or quasiparticles at energies much larger than the gap. At such energies, the electrons will decay very rapidly via electron-electron and electron-phonon collisions to create even more quasiparticles in the process. After this rapid decay, there is an excess number of quasiparticles (unpaired electrons) near the energy gap range. These quasiparticles will recombine to form Cooper pairs with the emission of phonons.

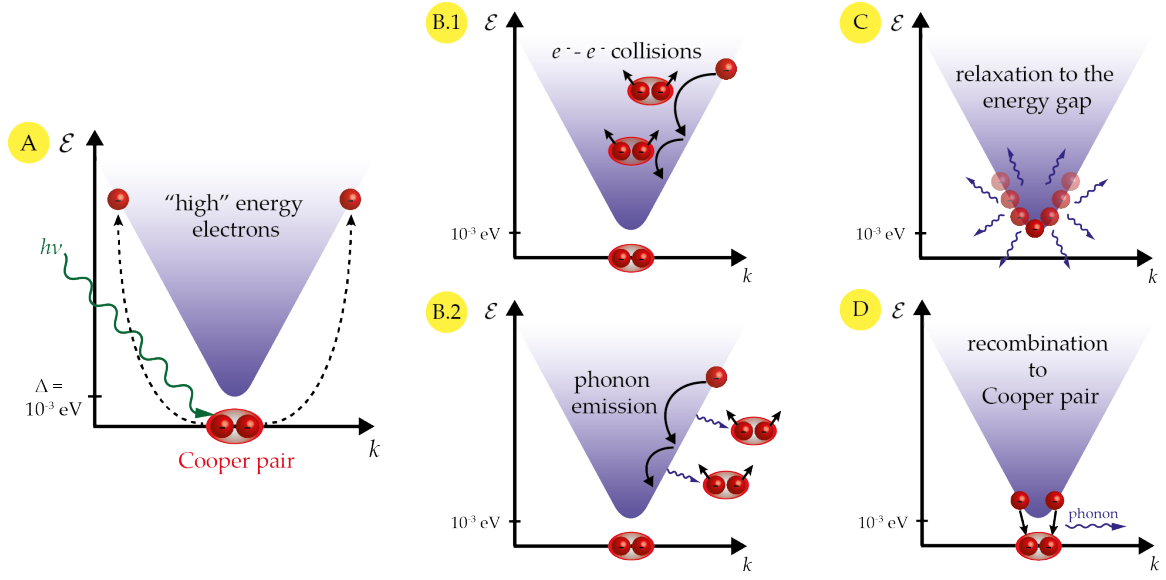

Figure 4.1: **Photon absorption in superconductor [10].** (**A**) Absorption of an incident photon $h\nu$ breaks Coopers and creates high energy electrons, far above the binding energy $\sim 10^{-3}$ eV. Decay process of high energy electrons via (**B.1**) electron-electron collisions or via (**B.2**) emission of phonons, which further break Cooper pairs to create more quasiparticles. (**C**) The decay process of quasiparticles for an absorbed photon occurs very quickly, and there's an excess of quasiparticles and phonons in the gap energy range. (**D**) The quasiparticles recombine with the emission of phonons to form Cooper pairs.

This process of quasiparticle creation and recombination can be described by the Rothwarf-Taylor rate equations.

$$\frac{dN_{qp}}{dt} = I_{qp} + \beta N_{ph} - RN_{qp}^2 \tag{4.1}$$

$$\frac{dN_{ph}}{dt} = I_{ph} + \frac{RN_{qp}^2}{2} - \beta N_{ph} - (N_{ph} - N_{ph}^T)\tau_{es}^{-1} \tag{4.2}$$

where I_{qp} and I_{ph} are the volume rate of creation of quasiparticles and phonons, respectively, by an external mechanism such as light illumination in our case. N_{qp} and N_{ph} are the total number of quasiparticles and phonons with energy $\hbar\omega > 2\Delta$, respectively, and N_{ph}^T is the number of phonons at thermal equilibrium. R is the recombination coefficient, β is the probability of breaking pairs by N_{ph} phonons, and τ_{es} is characteristic time for phonon escape. The factor $1/2$ in the second term of Eq. 4.2 stems from the fact that quasiparticles must be created and annihilated in pairs. The characteristic recombination time $\tau_R = (RN_{qp}^2)^{-1}$ for Nb tends to be on the order of picoseconds. With increasing quasiparticle density, or increasing illumination power, the ratio of quasiparticle and Cooper pair density can be modulated. In the regime of continuous laser excitation, the creation and recombination of quasiparticles reaches a steady-state equilibrium. By setting the left side of the differentials to 0, and solving the two equations self-consistently, a steady-state solution can be found. Under this steady-state a continuous regime of weak coupling can be maintained to produce a Josephson device [10, 11]. This is equivalent to *thinning* the superconductor by optical means.

4.1.2 Controllable Josephson weak links

There have been several studies exploring different external means of altering superconducting properties including light illumination [12, 13, 14, 15, 16, 17], electron injection [18] and application of a magnetic field [19]. The use of light has been of particular interest due to its facile implementation in controlling transport properties.

Exploring the possibility of locally reducing the gap of a superconductor by illumination was first theorised by Volkov in 1971 [20]. The first demonstration of this was shown in lead (Pb) superconducting films [12]. The choice was Pb was deliberate as it has a high temperature coefficient of resistance $(d \ln R/dT)$ just above the T_c of Pb. The change in resistance was used to quantify the change in temperature due to optical heating. They observed clear changes in the resistive transition as the temperature was varied from 4K to above T_c at 7.2K, shown in Fig. 4.2a. Compared to the usual steep onset of normal resistance near T_c, with half the power of their light source a gradual transition starting near 6K is observed, while

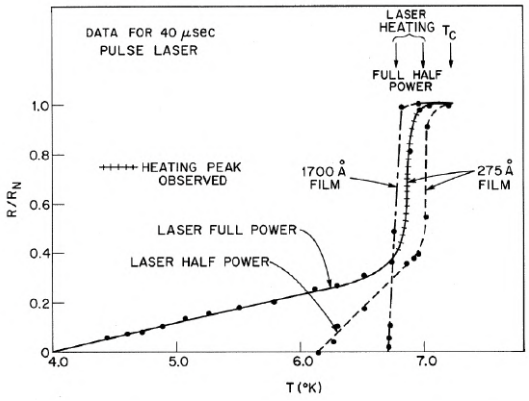

Figure 4.2: **Light induced Josephson characteristics.** Photo-induced changes in the resistive state of a Pb film [12]. The high temperature coefficient of resistance of Pb makes changes due to optical heating easy to detect.

with full power the transition onset be-
gins down from 4K. Comparing this behaviour in films of varying thicknesses, it was noted that only films with thicknesses comparable to the optical penetration depth and coherence length of the material show this photo-induced resistive state. For the thicker films, larger than these characteristic lengths, superconductivity still persists on the unilluminated side since the recombination time of the quasiparticles τ_R is much faster than the diffusion time and the non equilibrium response will be short circuited by the persisting superconductivity.

Following this, there were several reports exploring the possibility of creating weak link structures for superconducting devices. Rather than directly heating the superconductor using a laser, the evanescent field from a 5 μm wide optical wave guide on a 60 nm thick Pb film was used to create a weak-link region. The realisation of the Josephson regime is verified by the appearance of the Fraunhofer oscillations [14]. An important consequence of this study is that the Josephson regime appears only in a small range of illumination power [13], just before superconductivity breaks completely. An illumination method has also been used to modulate the critical current, which is suppressed with increasing illumination intensity [21].

Illuminated tunnel junctions have also been used as a means of studying fundamental aspects of light-superconductor interactions. Light induced excitation in one electrode of a Pb and tin (Sn) overlap tunnel junction [15] and in a Sn-oxide-Sn junction [16] were used to measure the influence of generated excess quasiparticles on the energy gap. Similarly, illumination of Al-PbBi tunnel junctions was used to correlate changes in the current-voltage characteristics to the non equilibrium quasiparticle distribution [17]. To analyse this a bit further we can consider the Ambegaokar and Baratoff relation [22] for the critical current of a tunnel JJ given as

$$I_c = (\pi\Delta/2eR_N) \cdot \tanh(\Delta/2k_BT) \approx \pi\Delta/2eR_N \tag{4.3}$$

where the approximation can be made for $T < T_c/2$. The parameter R_N is the normal state resistance just above T_c. Since there is a change in the energy gap related to the change in the excess quasiparticle density, measuring the change in the I_c gives us access to information regarding the microscopic changes as such $\delta I_c = \pi\delta\Delta/2eR_N$.

The subsequent change in the I-V characteristic of a weak link can be derived by considering the resistively shunted junction (RSJ) model where the voltage of a junction under test is given by $V = R_N \cdot \sqrt{I^2 - I_c^2}$. Illumination of the weak link results in a decrease of the critical current to $I_c - \delta I_c$, with a corresponding change in voltage δV given by

$$\delta V = R_N \left[\sqrt{I^2 - (I_c - \delta I_c)^2} - \sqrt{I^2 - I_c^2}\right] \tag{4.4}$$

The photoresponse of a weak link for $I > I_c$ and $\delta I_c/I \ll 1$ is given as

$$\delta V_{I>I_c} = \frac{R_N I_c \delta I_c}{\sqrt{I^2 - I_c^2}} \tag{4.5}$$

When $I < I_c$, the second term in Eq. 4.4 disappears because of the superconducting state and δV is given by

$$\delta V_{I<I_C} = R_N \left[\sqrt{I^2 - (I_c - \delta I_c)^2}\right] \tag{4.6}$$

Here the δV decreases with the increase of I and reaches zero when $I = I_c - \delta I_c$, below which the junction remains superconductive even when illuminated. As $I \to I_c$, δV reaches its maximum value and is approximated as

$$\delta V_{I=I_C} = R_N \sqrt{2 I_c \delta I_c} \tag{4.7}$$

The voltage shifts δV in an I-V curve due to illumination reveal a remarkable amount of information as the shifts can be correlated to the changes in the quasiparticle density [23].

4.2 Optically created weak link

4.2.1 *Dayem* bridge junction

While the tunnel junction structure, illustrated in Fig. 1.12, is the classic configuration used to demonstrate the Josephson effect, there are other *weak-link* structures or constrictions that exhibit the same properties. These structures are driven by different mechanisms, but still adhere largely to the basic JJ relations derived in Sec. 1.5.1, but they do result in some specific design criteria. A *Dayem* bridge junction is a type of constant-thickness bridge junction, where the weak-link is made from the same superconducting material. Josephson effects are induced by physically reducing the local dimensions of the superconducting strip to form a weak-link area. In general the current-phase relation does follow the sinusoidal relationship as a function of the phase difference, but there is uncertainty regarding which points should the phase difference be taken since there is no physical discontinuity. The design of the bridge allows the length and width of the weak-link area to be relatively large. Early devices of this design had constrictions on the micron scale. With respect to Nb, bridges can be fabricated with dimensions of 100-200 nm [24].

The device used here is a SQUID made from two Dayem bridge constrictions in parallel. The choice of using a SQUID compared to a single junction was made by considering that the SQUID transport measurements would be more sensitive to flux fields. The larger design scheme of the device was an arbitrary choice as per the capabilities and expertise of the collaborators. They have previously fabricated devices with an internal loop area of 1 μm^2 with electrode width of 300 nm using tens of nm Nb. In these devices the critical current is on the order of hundreds of μA. The specific design criteria for optical imaging requires a Nb film of thickness $\geq$ 100 nm, since vortices become physically larger with decreasing Nb thickness, leading to enlarged imaged vortices. Additionally, the electrodes at either side of the weak-link must be wide enough (≥ 1.5 μm) to allow room for imaging and manipulation single vortices. The lines connecting the device to the contact pads also needed to be long (total device span of 20 mm) to allow clearance around the device to perform optical measurements.

4.2.1.1 Fabrication

The SQUID consists of an evaporated niobium film with a thickness of $d \sim 100$ nm on a sapphire substrate. Masks were defined using E-beam lithography and metallic layers were deposited in an electron-beam evaporator. Prior to the deposition of Nb, the sapphire substrate is heated at 660 °C to remove oxygen contamination. In order to protect the Nb film from oxidation, a 5 nm-thick silicon capping layer is evaporated in the same vacuum cycle in order to avoid surface degradation. After that, the Nb-based SQUIDs are realised utilising an Al hard mask on top of the Nb film by E-beam lithography and followed by a lift-off procedure. The unprotected area of Nb with the Al mask is then removed by a reactive ion etching, followed by the removal of the Al by wet etching. An additional step in the later generation of SQUIDs was the addition of a gold shunt in parallel to protect the device from electrostatic discharge, shown in Fig. 4.3a.

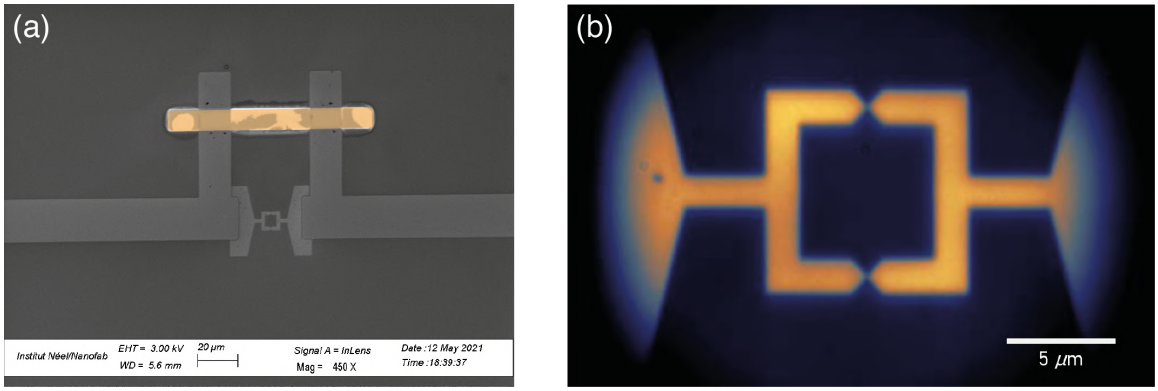

Figure 4.3: ***Dayem* bridge SQUID.** (**a**) SEM image and (**b**) Wide-field optical image of the SQUID. The bridge dimensions in the samples varied from $l \sim 100 - 200$ nm and $w \sim 50 - 70$ nm. The inside of the SQUID loop is 6×6 μm^2 with 1.5 μm wide electrodes. The device has been shunted with a gold line, highlighted in the SEM image, to protect the device from accidental electrostatic damage.

4.2.1.2 Critical transitions

We first characterise the critical resistive and current transitions of the device. The device is based on 100 nm Nb on sapphire and shows a sharp transition at T_c ~8.6K (Fig.4.4a), a normal resistance $R_N \sim 8\Omega$. The critical currents of microbridge style junctions follow the behaviour predicted by the Ginzburg-Landau theory at all temperatures and has been experimentally substantiated [25], and is given as

$$I_c = I_c(0)(1-t^2)^{\frac{3}{2}}(1+t^2)^{\frac{1}{2}} \tag{4.8}$$

where $t = T/T_c$. Near T_c, the relationship simplifies to $(1-t)^{\frac{3}{2}}$. Here, the critical current transition at 4.5 K is $I_c \sim 60$mA (Fig. 4.4b). For devices fabricated in the same manner that have weakly coupled electrodes exhibiting the Josephson effect, the I_c is about two orders lower [26]. The large I_c in these devices can be attributed to the dimensions of the weak-link, $I_c \propto wd$. Indeed, as we characterise the device further, we do not observe Josephson coupling.

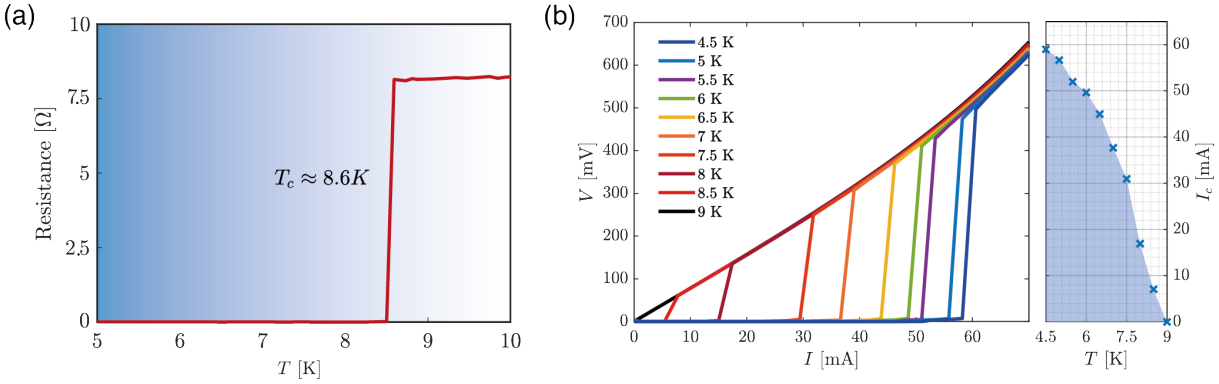

Figure 4.4: **SQUID critical transitions**(**a**) Resistive transition of device with a $T_c \sim$ 8.6K and $R_N \sim 8\Omega$. (**b**) Current transition plotted as a function of temperature. $I_c \sim 60$ mA at 4.5K.

4.2.2 Magnetic field dependence - $I_c(B)$

In order to verify operation of the device in the Josephson regime, we perform a magnetic field dependence of the critical current. The set of SQUIDS that we test (Fig. 4.3) have an inside loop area of 6×6 μm^2. The expected oscillation period can be easily calculated as $T_B = \Phi_0/A_{\text{loop}}$, to find 0.06 mT. It corresponds to having one flux quantum threading the loop area when increasing the field.

To perform this measurement, the field is swept between 0 and 0.3 mT, which would allow about 5 oscillation periods within the scan range. The measurements performed at ∼7K are shown in Fig. 4.5. In Fig. 4.5a, the field is swept from 0 to 0.3 mT and then from -0.3 mT to 0, taking an entire IV curve at each value of applied field. In Fig 4.5b, the field is scanned from 0 to 0.3 mT and then from 0.3 mT to 0. From the IV curves, the I_c is extracted. The plots show the I_c peaking and then decaying to some equilibrium level. The modulated I_c is within a few mA from its peak value, never being completely suppressed. In both cases the plots peak at the point where the measurement begins. These measurements were performed repeatedly at different temperatures, with larger magnetic fields, and over multiple devices from the set. There was no observed oscillatory behaviour indicative of the Josephson regime. It is clear that considering the dimensions of weak-link, especially the thickness of the film, $d \sim 100$ nm, the coupling in the bridge is too strong to be considered a Josephson device.

Normally, the film thickness is kept to few tens of nm as fabricated previously [26], but as per the requirement of MOI, a minimum Nb thickness of 100 nm is essential. Additionally, the device has extremely long contact leads, again due to imaging requirements. With the long superconducting leads extending from the pads to the center, where the device is, there is a thermal gradient that forms. In this process temperature near the pads is higher than the center, and with increasing current and time, this gradient tends to become smaller. In a perfectly compact and well thermalised system the effect would be minimal but in long leads this has been observed. The slight decay of the I_c from a peak value to the equilibrium level is attributed to this thermal gradient that forms from the outer pads through the long superconducting leads and then to the center of the device, until it reaches some steady-state equilibrium as the measurement progresses [26]. The dependence of the critical current on temperature is a fundamental property of the superconducting state.

There was also some clear degradation of the critical current values after long periods of measurement. In some cases, the change in values was due to some hysteretic effects and could be recovered by heating the system above T_c and cooling back down. But over time due to repeated cycles of current flow through the structure, there was clear electromigration of Nb atoms and the weak-link would simply break, as observed with imaging.

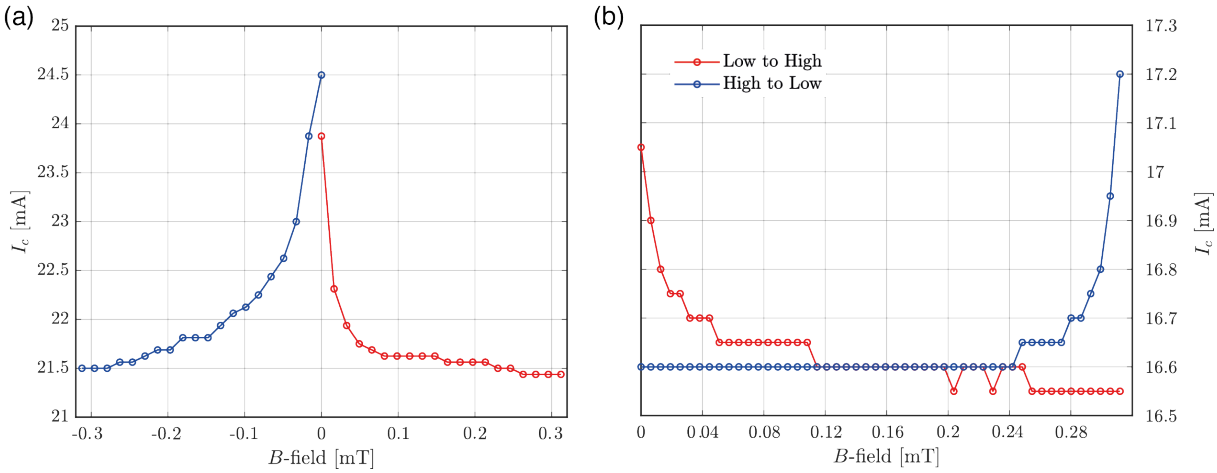

Figure 4.5: **SQUID magnetic field dependence.** (**a**) Magnetic field sweep from 0 to 0.3 mT and 0 to -0.3 mT, reversing the current direction in the coils. (**b**) Forward (low to high) and backward (high to low) sweep of the magnetic field. The measurements are performed at 7K and show decaying I_c at the beginning of the measurement with small change in the critical current.

4.2.3 Optical heating of weak-link

It is clear that the SQUIDs do not exhibit any Josephson coupling in their weak-links, most likely due to the thickness of Nb weak-link. A proposed method to solve this issue was to locally thin the thickness of the Nb weak-link during fabrication using FIB etching, while leaving 100 nm of Nb in the electrodes. However, this next step did not come to fruition due to extenuating circumstances. Therefore, an alternative approach is to optically thin the film by locally heating the constriction and reducing the superconducting character within few tens of nms to weaken the coupling of the order parameter between the two electrodes.

4.2.3.1 Confocal imaging

The constriction bridge has dimensions of $l \sim$ 150-200 nm for the length, $w \sim$ 50-70 nm for the width, and a thickness $d \sim$ 100 nm. Using the same optical system as the SIL-MOI setup, we are able to focus light from a 532 nm diode laser down to a spot size of ~330 nm. This allows us to image the finer structures of the device, and more importantly locally heat the area of the constriction bridge. This focused laser spot is scanned over the device area and the reflected light is collected to map a confocal image, shown in Fig. 4.6. As seen from the image, the weak-link can be discerned with great clarity, and using this map, the laser is placed at the central region to locally heat the constriction bridge.

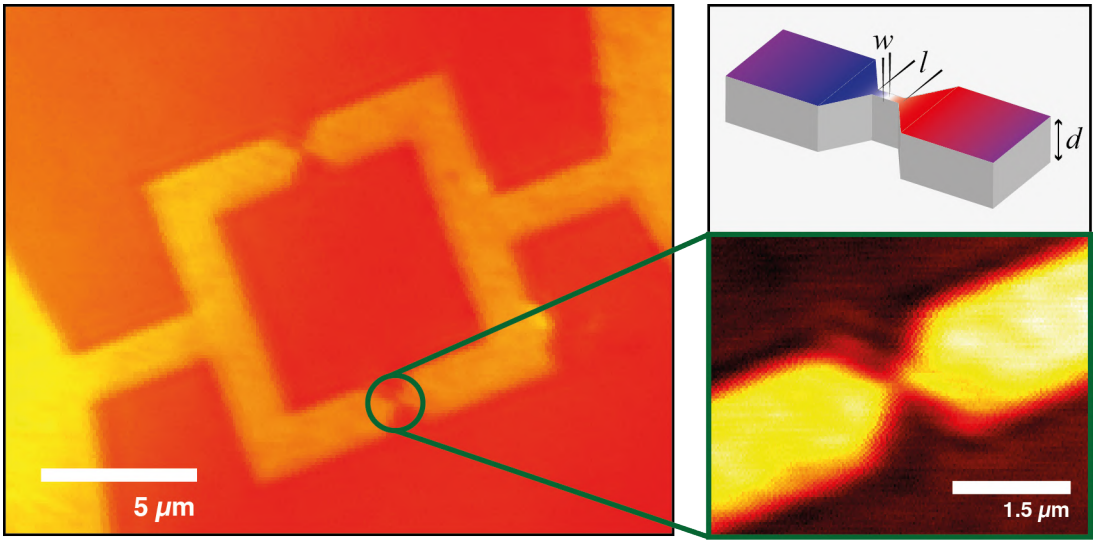

Figure 4.6: **SQUID confocal image.** A scanning confocal image of the device area is mapped using the SIL. The weak-link region can be further isolated and using finer steps, a high resolution image of the structure can be mapped. The region of the bridge cannot entirely be resolved as the dimensions fall below the resolution capability of the system.

4.2.3.2 Modulation of IV curve

Using the confocal localisation, the focused laser spot is centred on the constriction of one of the weak-links in the SQUID loop and the IV data is recorded with increasing intensity. In Fig. 4.7a. IV data is recording as a function of increasing laser intensity at $T \sim 8.3$K, close to T_c. Prior to illuminating the weak-link, an IV is taken for reference for the pristine device. The laser intensity is increased until a shift in the IV is observed, and then a full scan is taken from $-I$ to I, while the constriction is under continuous illumination. After that, the laser is blocked and the system is allowed to settle, followed by another IV under no illumination. The necessity of checking the recovery of the system is to ensure that no damage has occurred at the constriction due to heating, and the effect of real-time heating on the IV can be discerned from degradation due to physical damage. In Fig. 4.7a, within the illumination range of 0.14-0.57 mW/μm^2, the critical current starts to decreases until no transition is observed. This process is repeated at the other weak-link to show the same behaviour, albeit with slightly different values. This is attributed to the asymmetry of the weak-links and the minor differences in alignment as it pertains to the movement of the light due to the galvanometric mirrors and the alignment with the SIL, which would produce minor differences in focus.

The measurement is conducted at a range of temperatures as shown in Fig. 4.7b. At lower temperatures, the critical transition cannot be suppressed completely within the range of available laser intensity (up to 1.4 mW/μm^2), and shows a change in I_c within a limited range. Larger intensities can be used but the risk of damaging the weak-link is higher. Only after $T \sim 8$K, a full dynamic range of complete suppression and recovery be achieved. The minimal change in I_c due to optical heating at lower temperatures is a consequence of the strong coupling at the weak-links, and further justifies the absence of Fraunhofer oscillations.

Considering that a SQUID with two constrictions in parallel can be modelled as two circuit components in parallel, the total critical current of the device is $I_c = i_{c1} + i_{c2}$, where $i_{c1/2}$ are the individual critical currents of the respective constrictions. If both constrictions are symmetric, $i_{c1} = i_{c2}$, then $I_c = 2i_c$, and illuminating one constriction should halve the critical current of the total device, and the modulation should be limited to $1/2I_c$. However, this is not what is observed, at least at temperatures close to T_c. At lower temperatures this point is more challenging to discern from the effect of insufficient heating for complete suppression. It is possible that due to lateral diffusion of the heat, the second weak-link also heats up and the effect of complete suppression of the critical transition is one that is cumulative, rather than localised at a single weak-link. It is unlikely that heat diffusion occurs through the sapphire substrate, as both the substrate and sample holder (Cu) materials have high heat conductivity, resulting in efficient heat sinking. Moreover, the second weak-link is $\sim$7.5 μm away. But it is possible that at temperatures close to T_c the diffusion of heat occurs via Nb in the loop of the SQUID, and the effect we observe is cumulative rather than completely localised at one weak-lnk In order to further investigate the source of this effect, we can fix two laser spots at the weak-links and independently modify illumination power and subsequently the coupling strength. This would be a method to access the the full range of critical currents $[0, 2i_c]$ at low temperatures, where the suppression of superconductivity due to local optical heating can be separated from potential global heating due to heat diffusion.

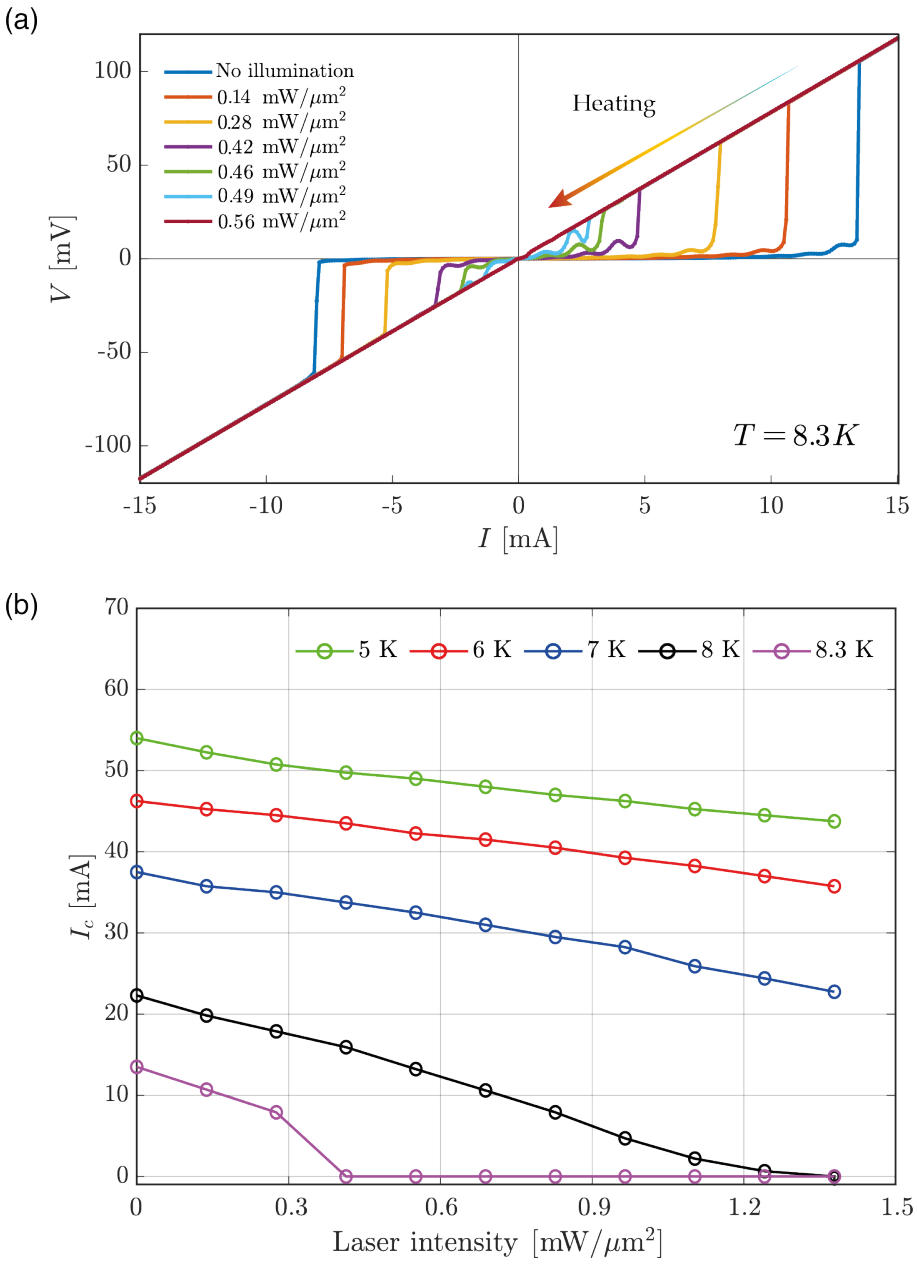

Figure 4.7: **SQUID IV modulation.**(**a**) Optically induced modulation of the I_c of one weak-link at $T \sim 8.3$K. Within a range of impinging illumination intensities the I_c of the device can be suppressed completely and recovered by cutting the illumination. (**b**) Suppression of the device I_c at T = 5-8.3K. The suppression is limited at low temperatures even with strong illumination.

Given that the weak-links can be weakened by optical means and recovered at will, it follows that the measurement of a magnetic-field dependence is performed to verify operation in the Josephson regime. Unfortunately, since these devices tend to have a limited lifetime due to the aforementioned breaking of the weak-links due to electromigration, and the limited availability of more devices, it was not possible to further investigate this phenomenon.

4.3 Nonzero Josephson phase difference in planar JJ

The flow of dissipationless current across a JJ stems from a nonzero Josephson phase difference (JPD) between the superconducting electrodes, described by the current phase relation (CPR), $I_s = I_c \sin(\Delta\theta)$. The important relations for the Josephson effect were derived in Sec. 1.5. This form of the CPR is rooted in the preservation of either the time reversal ($t \to -t$) or inversion ($\vec{r} \to -\vec{r}$) symmetry. If one of these symmetries is preserved, the JPD is $\Delta\theta = 0$ and no current flows across the junction. These symmetry constraints impose a *phase rigidity* on the superconducting phase [27]. The generation and control of a nonzero JPD in the ground state is sought after due to its potential use as phase batteries, which are key components of quantum circuits. Analogous to a classical battery which converts chemical potential energy into a voltage bias pushing current in an electronic circuit, a phase battery element, or JJ in our case, provides a persistent phase bias to the wave function thus pushing a nonzero supercurrent across the junction [28].

The manifestation of a nonzero JPD in the ground state is best understood by looking at the Josephson energy, E_J. While no energy is dissipated by the junction when operating in the superconductive state, there exists a finite binding energy, known as the *Josephson coupling energy*, due to the overlap of the macroscopic wave functions of the weakly coupled superconductive electrodes. Recalling the voltage-phase relation, $V = \frac{\Phi_0}{2\pi}\frac{\partial(\Delta\theta)}{\partial t}$, the Josephson energy can be calculated considering this change in energy or equivalently to the work done on the junction to go from the initial to the final state. Assuming that at a time 0 the Josephson phase is 0 and at a later time t the JPD evolves to $\Delta\theta$. The energy stored in the junction is then given as

$$E_J = \int_0^t I_s V dt = \frac{I_c \Phi_0}{2\pi} \int_0^{\Delta\theta} \sin(\theta) d\theta$$

$$E_J = E_{J0}[1 - \cos(\Delta\theta)] \tag{4.9}$$

where $E_{J0} = I_c\Phi_0/2\pi$ is the coupling energy.

When there is no applied current ($I = 0$) or the junction is disconnected, the junction is in its ground state and the $\Delta\theta = 0$. Conversely, the JPD can also be $\Delta\theta = \pi$ with no current flowing across the junction. However, in a pristine junction the $\Delta\theta = \pi$ state is an unstable energetic maximum in the Josephson energy, while $\Delta\theta = 0$ is a stable energetic minima, illustrated in Fig. 4.8a. While maintaining the phase rigidity, the breaking of only time-reversal symmetry, with the application of an external magnetic field, results in a π shift in the energy profile, illustrated in Fig. 4.8a [29]. A system allowing transitions between $0-\pi$ states is critical in the development of novel cryogenic memories where the JPD can be used to switch the current from a 0 and 1 state with maximum distinction [5, 30].

Now if both time-reversal and inversion (by applying a current) symmetries are broken a finite phase shift $0 < \phi_0 < \pi$ can be induced with the CPR reading $I_s = I_c \sin(\Delta\theta + \phi_0)$, shown in Fig. 4.8b. A π-junction is a specific example of a ϕ_0-junction. This is referred to as the anomalous Josephson effect. From the new CPR it is clear that this so called ϕ_0-junction will generate a constant phase bias in an open circuit configuration, but when inserted into a closed superconducting loop it will induce an

anomalous Josephson current as per $I_s = I_c \sin(\phi_0)$. The ϕ_0-junction is non-degenerate in its ground state.

Another phase configuration can also be implemented, denoted as a ϕ-junction. In contrast to the ϕ_0-junction, a ϕ-junction is doubly degenerate $\Delta\theta = \pm\theta$ in the ground state, and provides two energetic minimas for two different currents $I_{c1,2}$ within a period. This is an attractive prospect as it opens up the possibility for more complex operations. Some different physical properties of the junction can be obtained when considering a Josephson energy and CPR that includes higher harmonics of the form below [31]

$$E_J = \frac{\Phi_0}{2\pi}[I_{c1}[1 - \cos(\Delta\theta)] + I_{c2}[1 - \cos(2\Delta\theta)]] \tag{4.10}$$

$$I_s = I_{c1}\sin(\Delta\theta) + I_{c2}\sin(2\Delta\theta) \tag{4.11}$$

where the second harmonic term with an amplitude $I_{c2} < 0$ depends on the physical properties of the junction. The two minima at $\Delta\theta = \pm\theta$ are obtained when $I_{c1} > 1$ and $I_{c2} < -I_{c1}/2$ with $\phi = \arccos(-I_{c1}/2I_{c2})$. The Josephson energy and CPR for this junction are shown in Fig. 4.8c. For illustrative purposes the parameters chosen while adhering to the aforementioned conditions are $I_{c1} = I_c$ and $I_{c2} = -I_c$. The two stable ground states $\pm\phi$ can be used to store digital information as a memory cell or as a two-level quantum system [32].

There have been several methods employed to achieve a nonzero spontaneous ground state JPD. The use of unconventional superconductors with sign-reversal order parameter is one that has been investigated. High temperature cuprate superconductors (e.g. YBCO or BSCCO) have an anisotropic order parameter. In these structures the order parameter can be -1, 0 or 1 depending on if one looks along different crystal axes. In contrast, conventional superconductors exhibit a uniform order parameter regardless of the orientation. By making JJs with high temperature superconductors in different orientations, or with a combination of both high and low temperature superconductors, a π JPD can be achieved [33, 34, 35].

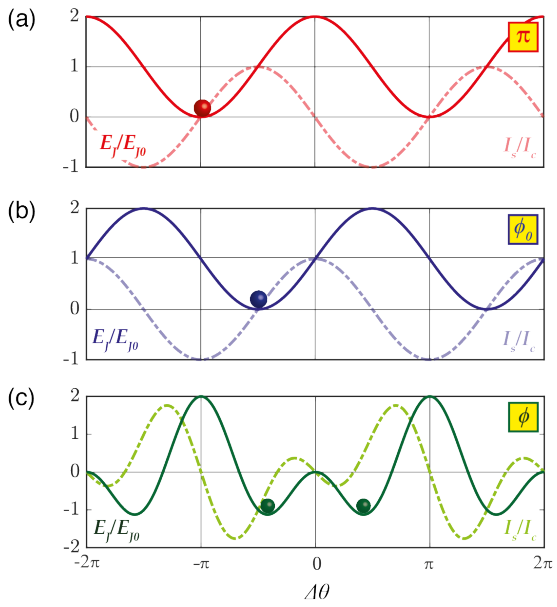

Figure 4.8: **Ground state JPD.** Josephson energy E_J (solid line) and current-phase relation I_s (dashed line) for **(a)** a π-, **(b)** a ϕ_0-, and **(c)** a doubly degenerate ϕ-junction. The spheres show the energetic minima corresponding to the ground states.

Exploiting structures like a S|F|S junction where a ferromagnetic layer between superconducting electrodes has also proven effective in achieving a nonzero spontaneous JPD. The exchange field inside the F-layer produces spatial oscillations of the order parameter and the ratio of the F-layer thickness and the oscillation field determines if the junction will have a 0 or π ground state. More interestingly, by

spatially varying the thickness of the F-layer along the junction cross-section, where some parts correspond to a 0-junction while the other to a π-junction, can result in the appearance of a spontaneous $\Delta\theta = \pm\phi$ JPD. [36, 31, 37]. Furthermore, a ϕ_0-junction can also be created in S|F|S structures with strong spin-orbit coupling[38]. It has been shown that a S|F|S junction can be tuned between 0 and π states by changing the temperature [39]. This method of tunability requires the presence of magnetic impurities and careful design of the F-layer thickness.

An alternative approach to have more tunability of the JPD is embedding some current injection points into one of the electrodes close to the junction. The application of current induces some non uniformity in the JPD along the junction thereby modifying its ground state. It can be done by implanting a pair of microscopic current injectors in a source drain configuration with the JPD being proportional to the injected current [40, 41]. This method has been used to achieve ϕ_0 and ϕ JPDs as a function of the current injection parameters [42]. The obtained JPD is extremely sensitive to the position of the injectors and precise placement during fabrication is required. However, engineering of the desired ground state by this means is challenging and is extremely difficult to tune post fabrication.

4.3.1 Abrikosov vortex driven JPD

In line with the use of current injectors, the presence of Abrikosov vortices in JJ electrodes realises a similar effect. The exploitation of an AV as a phase shifting bit has been demonstrated with the use of holes fabricated into the electrodes acting as vortex traps [3]. It was shown that the phase modulation along the junction length is equivalent to the polar angle $\Theta_v = \arctan\frac{x-x_v}{z_v}$ of the vortex position, shown in Fig. 4.9a. An SEM image of a JJ with a fabricated vortex trap is shown in Fig. 4.9b. The phase shifts appear in the magnetic field dependence of the critical current $I_c(B)$, with the corresponding distortion of the oscillation pattern being indicative of a π shift in the ground state. Given the fixed position of the vortex trap, the JJ can be switched between 0 and π when the trap is empty or contains a vortex. This methodology was further developed into a more complex array of traps where the vortex entry and exit could be controlled by current pulses to report a proof of concept for the operation of a Abrikosov vortex driven memory cells [5], and as reconfigurable phase shifters in JJs with a large dynamic range beyond $0-\pi$ transitions [43].

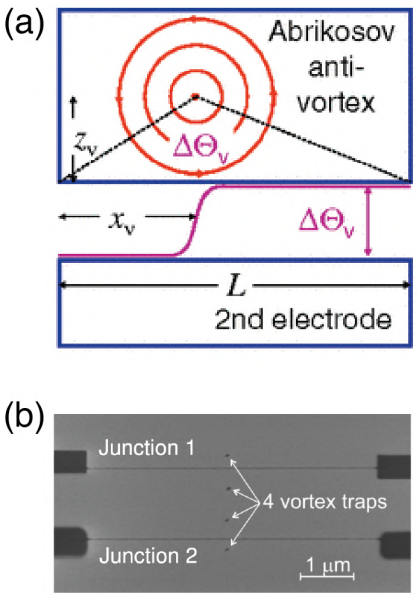

Figure 4.9: **AV induced JPD.** [3, 43] (**a**) The induced JPD is proportional to the polar angle Θ_v. (**b**) SEM of device with two JJ and multiple fabricated vortex traps.

There are two distinct mechanisms that contribute to a shift in the JPD of the ground state. Consider a planar junction, shown in Fig. 4.10a., a vortex trapped in one of the

superconducting electrodes near the junction will induce nonuniform phase profiles along the junction. This is due to the circulating supercurrent around the vortex, which decays exponentially at a short range, on the scale of the London penetration depth $\lambda_L \sim 100$ nm. When the vortex is at a proximity $\leq \lambda_L$, it is the circulating currents that are the primary contributors to the induced JPD. This effect is generally calculated using the image method of electrostatics [2, 44]. The second mechanism becomes the primary contributor to the phase shifts at a long range, $z_v \sim \mu m > \lambda_L$. The long range mechanism is due to the stray magnetic fields that propagate outside the electrodes and terminate at the junction, shown in the profile view in Fig. 4.10b. The induced JPD is seen to depend on the position of the vortex dictated by the polar angle Θ_v. There is a clear crossover point for the applicability of phase shifts due to the circulating supercurrent or due to the stray fields of the vortex. Looking at the induced JPD as a function of Θ_v, there is a superlinear dependence at a short range and a linear dependence at a long range, respectively [44]. This is shown in Fig. 4.10c. Therefore, it is possible to induce a significant JPD from a longer range. In practise, this is the effect that is exploited to achieve a shift in the Josephson phase.

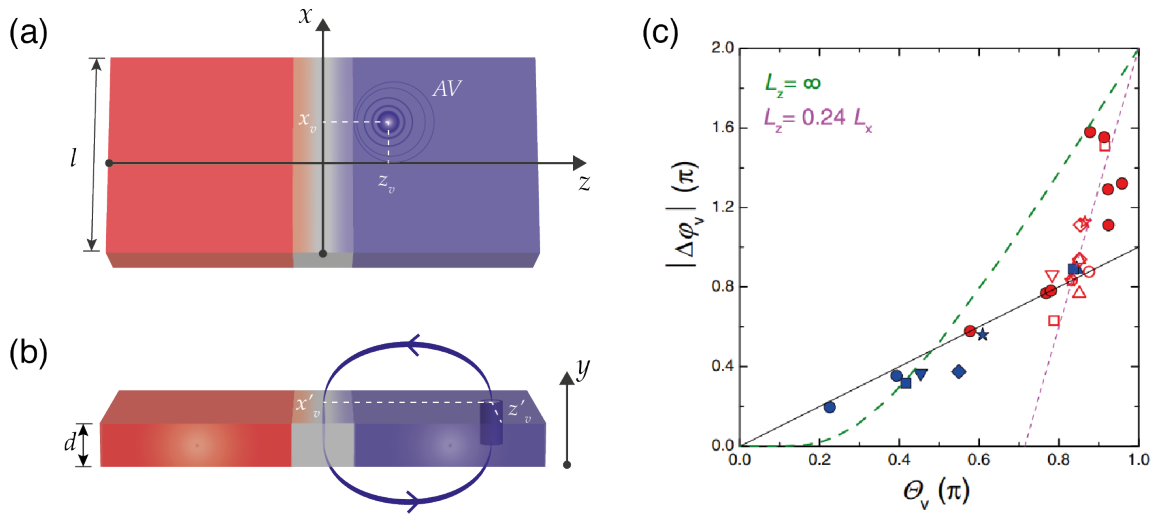

Figure 4.10: **Mechanisms of AV induced JPD** [44]. (**a**) Vortex trapped close to the barrier at the position (x_v, z_v), where $z_v \sim \lambda_L$. The effect is short-range as the JPD is largely influenced by the circulating supercurrents around the vortex. (**b**) Profile view of JJ with vortex trapped at (x'_v, z'_v) and $z'_v > \lambda_L$, with the stray fields terminating at the junction. This effect is long-range. (**c**) The vortex induced JPD plotted as a function of the polar angle Θ_v. The symbols represent experimental results and similar symbols correspond to junctions of the same device. The solid line represents phase shifts due to stray fields calculated using the polar angle relation, and the magenta and olive dashed lines represent shifts due to circulating current calculated using image solution formulism. At $\Theta_v \sim 0.8\pi$, there is a crossover between superlinear and linear dependence, separating the contributions of the two mechanisms.

With these recent works it is clear that AV driven cryoelectronics is an avenue holding immense potential. However, the limitation lies again with the lack of tunability post-fabrication with the position of the vortex traps in the superconducting electrodes.

As demonstrated in our group the optical tweezers technique is capable of ultrafast optical positioning of single vortices. This can be exploited to gain dynamic tunability of the JPD with no limitations placed by fabricated structures [2, 7].

4.3.2 Josephson phase difference Simulation

The effect of the presence of a vortex on the oscillation pattern can be calculated using the calculations shown in Ref. [1, 2, 45]. The supercurrent densities $\mathbf{J}_{1,2}$ in the respective electrodes 1,2 are determined by the supercurrent equation Eq. 1.13. The derivation of the throughput current through the junction, and the magnetic field dependence are detailed in Sec. 1.5.2. The modulation of the throughput current is driven by a phase difference $\Delta\theta = \theta(l) - \theta(0)$ over the junction width. In the Meißner state, without a vortex, the phase difference due to an external applied field is given by

$$\Delta\theta_M = 2\pi\frac{\Phi}{\Phi_0} \tag{4.12}$$

where $\Phi = t_B \int_0^l B dx$ is the effective magnetic flux in the junction. Integrating this expression the spatial modulation of phase difference is given as $\Delta\theta_M(x) \simeq (2\pi t_B B/\Phi_0)x + \mathrm{C}$, where C is the integration constant. The supercurrent equation is linear, thus, the phase difference due to a vortex is simply given by the superposition of contributions from the Meißner state $\Delta\theta_M(B)$ and from the vortex at zero external magnetic field $\Delta\theta_v$.

$$\Delta\theta = \Delta\theta_M(B) + \Delta\theta_v \tag{4.13}$$

As before, the magnetic field dependence of the critical current with the effect of the vortex field is given by

$$I_c(B) = \frac{I_{c0}}{l}\int_0^l \sin[\Delta\theta_M(x) + \mathrm{C} + \Delta\theta_v(x)]dx \tag{4.14}$$

The I_c pattern is obtained by maximising this equation with respect to C. Using this formulation, we can simulate the expected modulation of the magnetic field dependence in the presence of a vortex in the electrode.

The phase $\Delta\theta_v = \Theta_{v1}(x)$ along the junction is in the limit of $z_v > \lambda_L$ is given by the polar angle of the vortex.

$$\Theta_{v1}(x) = \arctan\frac{x - x_v}{z_v} \tag{4.15}$$

where the parameters (x_v, z_v) are the coordinates of the vortex position and x is the position along the junction. The phase shift in the second electrode Θ_{v2} due to the flux from the vortex in the first electrode reaching the second electrode can be considered negligible.

When in close proximity to the junction ($z_v \leq \lambda_L$), it is the circulating supercurrents that influence the JPD, and this can be considered by solving the supercurrent equation with contribution of the vortex current, $\mathbf{J}_{vx}$. The phase difference across the length of the junction is then given by

$$\Delta\theta_v = \frac{2\pi\mu_0\lambda_L^2}{\Phi_0}\int_0^l \mathbf{J}_{vx}\, dx \tag{4.16}$$

The evolution of the effect of this mechanism on the JPD as a function of the distance is plotted in Fig. 4.11 [2]. The effect persists within a few λ_L. While this is a simplistic presentation of the results of these calculations, in Ref. [2] a full set of solutions is presented with various vortex configurations.

Thus, it is clear that the distinct $I_c(B)$ patterns carry information regarding field distribution and amplitude of the vortex source due to its proximity. These equations will be used in conjunction with a fitting algorithm to extract the resulting phase shifts. This method can be used to create a system of coding information purely based on spatial manipulation of the vortex in the electrode.

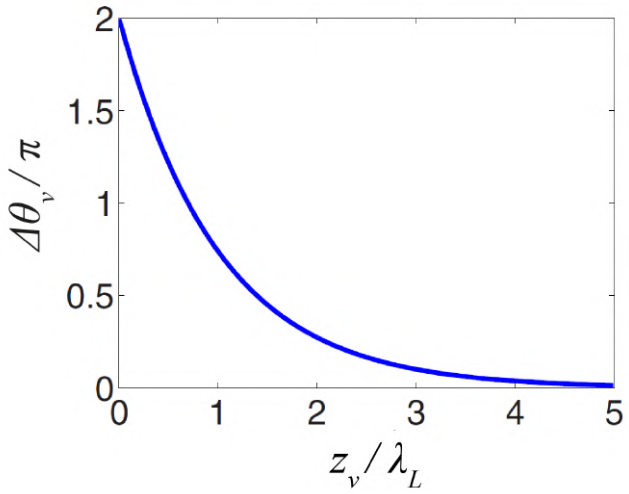

Figure 4.11: **JPD shift due to votex current.** [2] The phase shift in the JPD due to circulating vortex currents. The effect persists with the range of few λ_L.

We can grasp an intuitive understanding of the potential of our optical method by mapping the continuous vortex induced phase differences by as a function of the vortex position. In Fig. 4.12a. a 2D plot illustrating an electrode on one side of the junction and the coordinate dependent phase shift that a single vortex will induce along the junction edge. In this case we only consider the long-scale contribution of the vortex induced phase difference, so the model diverges in the immediate vicinity of the junction edge ($\sim \lambda_L$). All coordinates are normalised to the length of the junction l. The map marks multiple positions correlated to plots in Fig. 4.12b. that show the profile of the phase difference along the junction. In Fig. 4.12c. a series of plots are illustrated simulating the evolution of the $I_c(B)$ patterns with changing local fields due to the presence of a vortex. The patterns are correlated to the positions shown in the 2D map. In the first row the vortex is moved along the center line $x_v = 0.5l$ travelling from far to extremely close to the junction. In this case the amplitude of the field associated with the vortex is changing upon approach. The patterns get more distorted the closer the vortex gets to the junction. In the second row the vortex is moved along the junction at a fixed distance $z_v = 0.1l$ from one edge to another. In this case only the position of the flux source changes while the amplitude remains the same. The phase Θ_v yields a total flux in the junction of $|\Phi| = |\Theta_v/2\pi|/\Phi_0$.

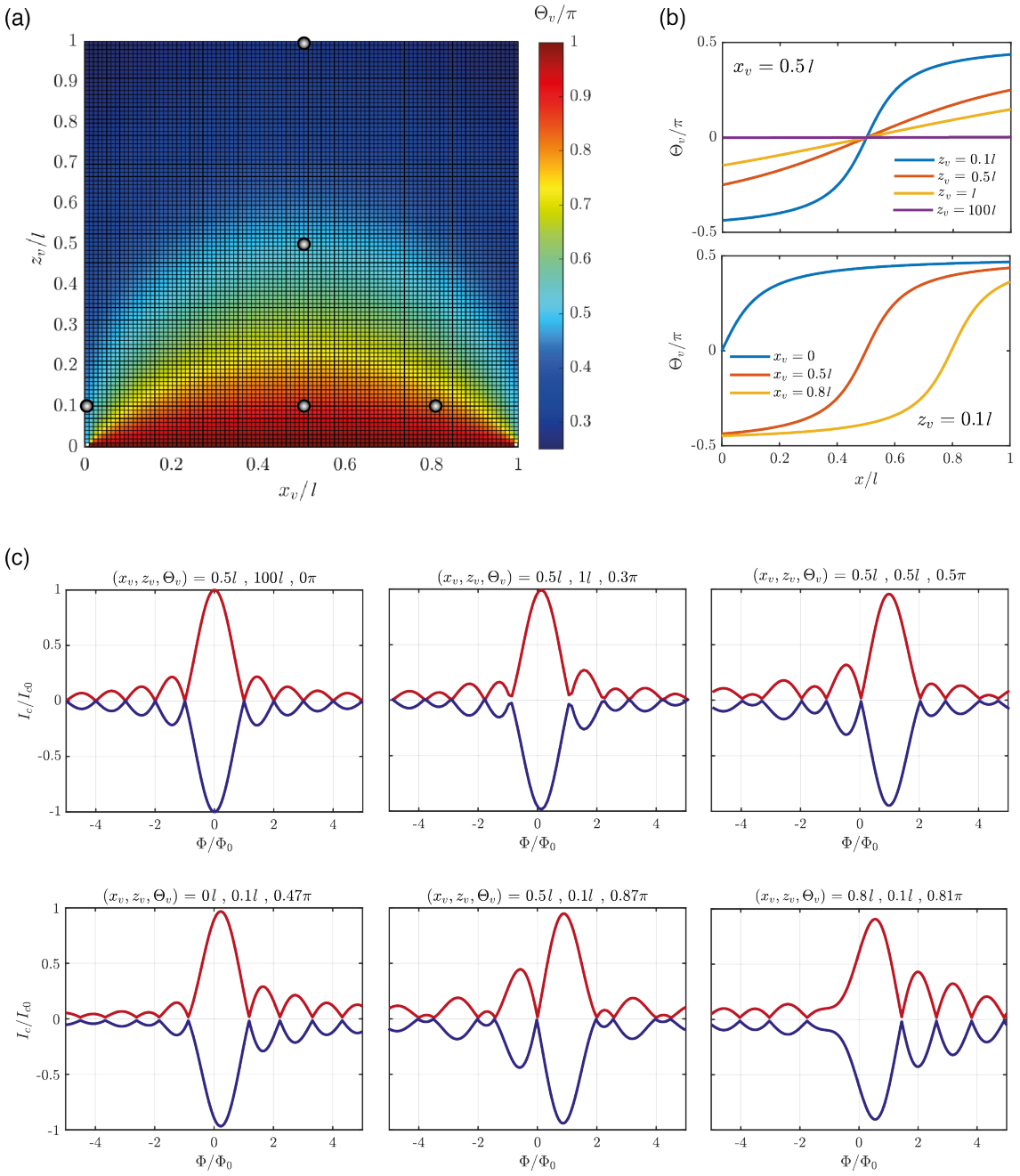

Figure 4.12: **Josephson phase shift** (**a**) A 2D map of one electrode of a junction is illustrated. The dimensions are normalised to the junction length l. The map shows the position dependent phase shift a vortex induces along the junction length. (**b**) The plots show position correlated phase difference profiles. (**c**) The simulated Fraunhofer oscillation plots are shown for the positions marked on the 2D map. The distortion of the interference patterns results from the net effect the presence of a vortex has on the spatial profile of the phase along the junction edge.

4.4 Optically driven Abrikosov vortex - Josephson junction

4.4.1 SNS junction

In this study we use a type of S-N-S junction where the constriction is a *variable thickness bridge*, shown in Fig. 4.13. Rather than sandwiching a normal metal layer between two superconducting electrodes (or *banks*), the normal metal is an underlying *span* film. In this type of structure the supercurrent flows due to *the proximity effect*. The effect lies in the fact that if a normal metal and a superconducting metal are brought into good electrical contact, Cooper pairs are able to conserve the amplitude and phase of the order parameter $\Psi(\mathbf{r}, t)$ into the normal metal decaying exponentially within the metal over a skin-depth or a normal coherence length ξ_N. In general, at a *N*-*S* interface, even in the absence of any throughput current, the order parameter permeates into the normal metal.

For typical type-II superconductors the coherence length ξ_c is on the order of tens nanometers, while a non-superconducting metal in contact with a superconductor can have a coherence length ξ_N of hundreds of nanometers. Then the width of the normal layer d_N can be much greater than a typical oxide layer in an insulating barrier ($\sim \xi_c$). The typical thickness of the superconductor bank film is ∼100 nms, while the metal span film may be tens of nms. This relative difference in thicknesses results in low critical current in these devices, and the thicker banks improve the thermal flow from the span to reduce self-heating effects. The effective spacing d_{eff} between the electrodes should normally be $d_{eff} \sim \xi_N$ to minimise deviations from the simple sinusoidal current-phase relation. Typical normal metals used for this junction include gold, silver, copper, aluminum, among others. For these materials the ξ_N well below T_c tends to be ∼100-200 nm, and have been used at these widths to exhibit the 'ideal' Josephson effect. The devices used here are made of copper and niobium as the span and bank materials, respectively. Copper has a $\xi_N \sim 200$ nm in the range of T_c of Nb [46]. Besides, the normal metals listed above have sufficiently high melting points to safeguard against accidental device burnouts [24, 47].

4.4.1.1 Fabrication

The devices used here were produced at the *Moscow Institute of Physics and Technology*. The variable thickness bridge junctions with the Nb/Cu/Nb structure were fabricated using UHV magnetron sputtering, electron beam (E-beam) lithography technique with hard mask, and plasma-chemical etching. First, a 50-nm Cu film followed by 100 nm of Nb is deposited onto Si/SiO_2 substrate, in a single vacuum cycle. The 500 μm Si/SiO_2 substrate has a layer of Cu of a few hundred nms on the underside. A polymer mask for the Nb banks, the extended lines and contact pads was then formed by E-beam lithography. The pattern was covered by a 20-nm-thick aluminum layer lift off, forming the Al hard mask for Nb banks. Next, the Nb was etched by the plasma-chemical process. After Nb patterning the Al mask was removed. The resulting device in the JJ area, shown in Fig. 4.13, has a junction length of 5μm and a junction width of 150 nm. A layer of 200 nm PMMA is deposited on top of the device area to prevent oxidation of

the Cu layer, as oxidised copper will become insulating and render the device unusable.

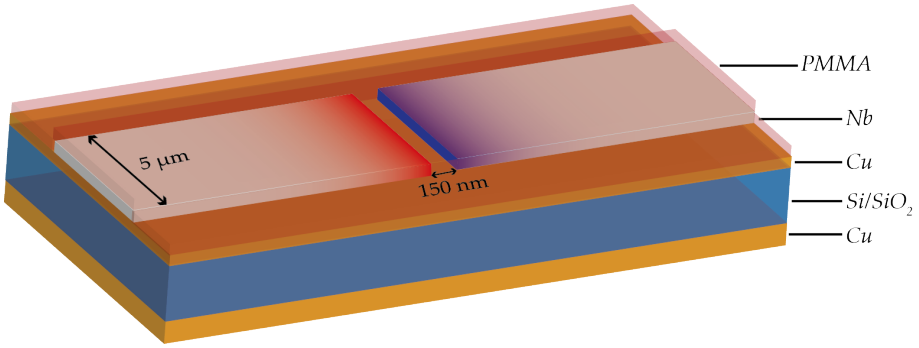

Figure 4.13: **Variable thickness bridge - SNS junction.** The junction length is 5 μm, with a width of 150 nm. A layer of 200 nm PMMA is deposited on top to protect the Cu from oxidation. Each of the electrodes branches into a pair of contact pads, and the transport properties are measured by applying a current and measuring the voltage drop across the junction in a 4-point configuration.

4.4.1.2 Critical transitions

Here we study a device based on 100 nm Nb on 50 nm Cu. The critical resistive and current transitions are characterised for the SNS device. The resistive transition shown in Fig. 4.14a. shows a broad transition ($\sim$ 0.5K) from 7.2K, reaching a stable normal resistance $R_N \sim 5m\Omega$ at T_c ~7.7K. It has been shown the broad transition is common in these devices due to spontaneous flux flow [48].

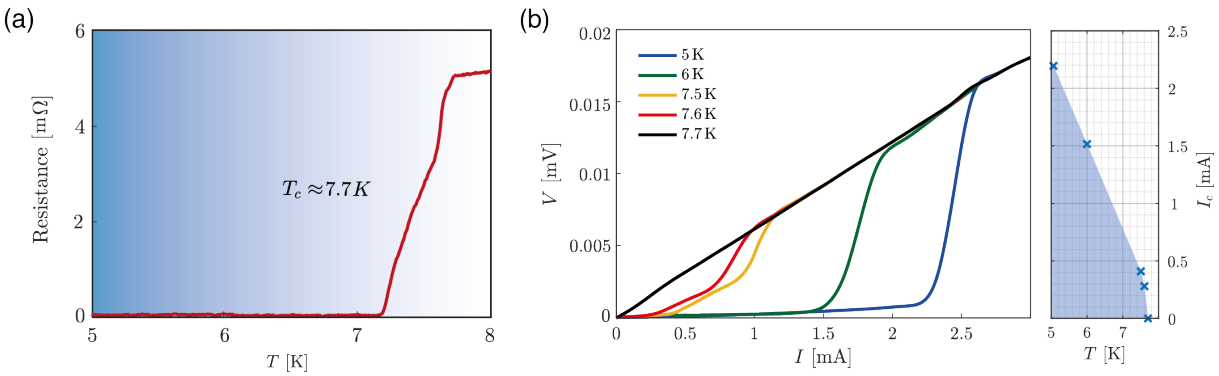

Figure 4.14: **Critical transitions(a)** Resistive transition of device with a $T_c \sim$ 7.7K and $R_N \sim 5m\Omega$. **(b)** Current transition plotted as a function of temperature. $I_c \sim$ 2.3 mA at 5K.

The critical current transitions in Fig.4.14b are taken at the onset of the sharper finite voltage transitions. The I_c has a peak value of $I_c \sim$ 2.2 mA at 5K. The normal voltage tends to be low in devices of this structure and follows $V_N \approx V_{\max} \exp[-d_N/\xi_N(T_c)]$, where $V_{\max}$ does not exceed tens of micro-volts [24].

4.4.2 Magnetic field dependence - $I_c(B)$

In order to establish operation in the Josephson regime, the magnetic field dependence of the critical current is measured. The magnetic field is applied perpendicular to the device surface and a full IV scan is taken at each increment of magnetic field. The junction surface area used for the flux calculation has been taken as $A = l \times t_B$, where $l = 5$ μm is the geometrical length of the junction, and $t_B \approx 400$ nm is the so-called magnetic thickness of the junction. It is calculated as $t_B = d_N + 2\lambda_L \coth(d/\lambda_L)$, where $d_N = 150$ nm is the geometrical distance between the two Nb electrodes, λ_L and d are the usual London penetration depth and thickness of the Nb film, both ~100 nm. Using this, the period of the oscillation is found as $T_B = \Phi_0/A_{\text{junc}}$ ~1 mT.

In Fig. 4.15, we sweep the magnetic field from 0 to 5 mT acquiring an IV curve at each point. The magnetic field is produced using home-made solenoid coils placed around the cryostat. It is verified using MOI that there are no vortices within the FOV (60 μm) around the junction. Both sets of data are combined to produce the final plot. The white curve illustrates the ideal Fraunhofer oscillation pattern for a junction with the calculated periodicity and $I_c(B = 0)$ of 2.4 mA. Similar curves are measured at different temperatures, shown in Fig. 4.16. This is the first time that this measurement has been successfully performed in our group using the home-built set-up and vortex imaging capabilities.

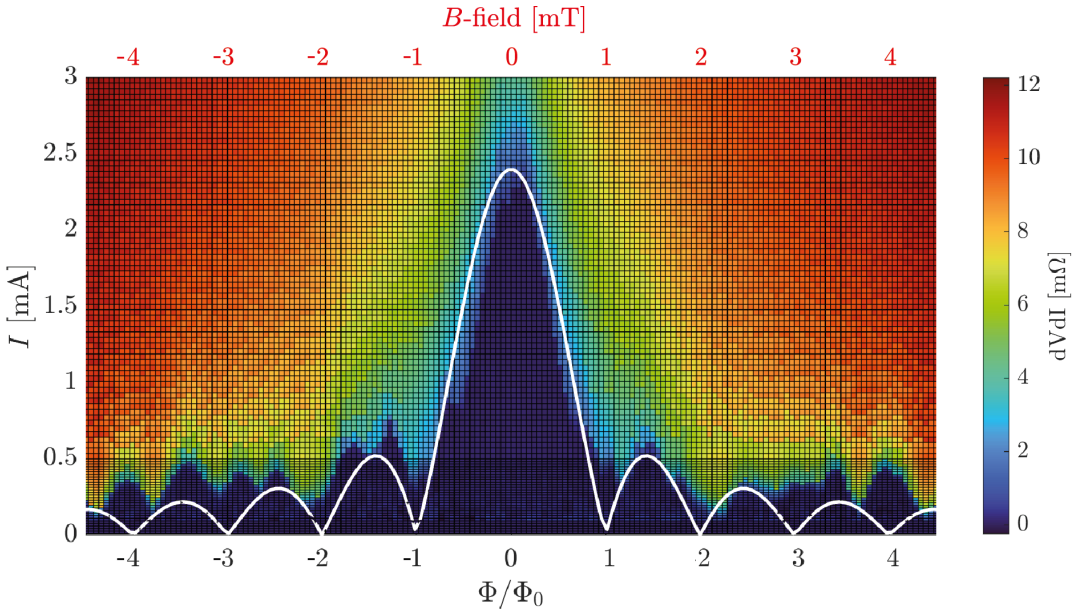

Figure 4.15: **Magnetic field dependence.** The magnetic field is swept from -3 to 3 mT, acquiring a full IV curve at each increment. Fine increments are taken at low current values. The colour scale shows the dV/dI intensity. The white curve is the interference for an ideal junction of the calculated periodicity. Data acquired at $T \sim 5$K.

At first observation it is clear that while the central peak matches the ideal oscillation pattern, the peaks at higher fields are distorted, lacking discernible periodicity or shape. Normally, this type of distortion is a result of external stray fields that superpose inhomogeneously with the pristine interference pattern. Vortices can be a source of distortion in the oscillation pattern but in this case there were no vortices present close to the

junction. Alternatively, these distortions stem from sharp gradients in magnetic fields originating from the environment surrounding the cryostat. Currently the application of the magnetic field is limited to one axis, normal to the device surface. Therefore, to compensate for these stray fields, modifications to the set-up will be carried out to implement coils along the other two axes. These factors can contribute to the distortion observed in the oscillation pattern, which will make it challenging to discern the contribution of a vortex to the phase shift in the pattern. Since these are initial measurements, improvements in the equipment are required to ensure proper isolation and therefore improved sensitivity to vortex fields.

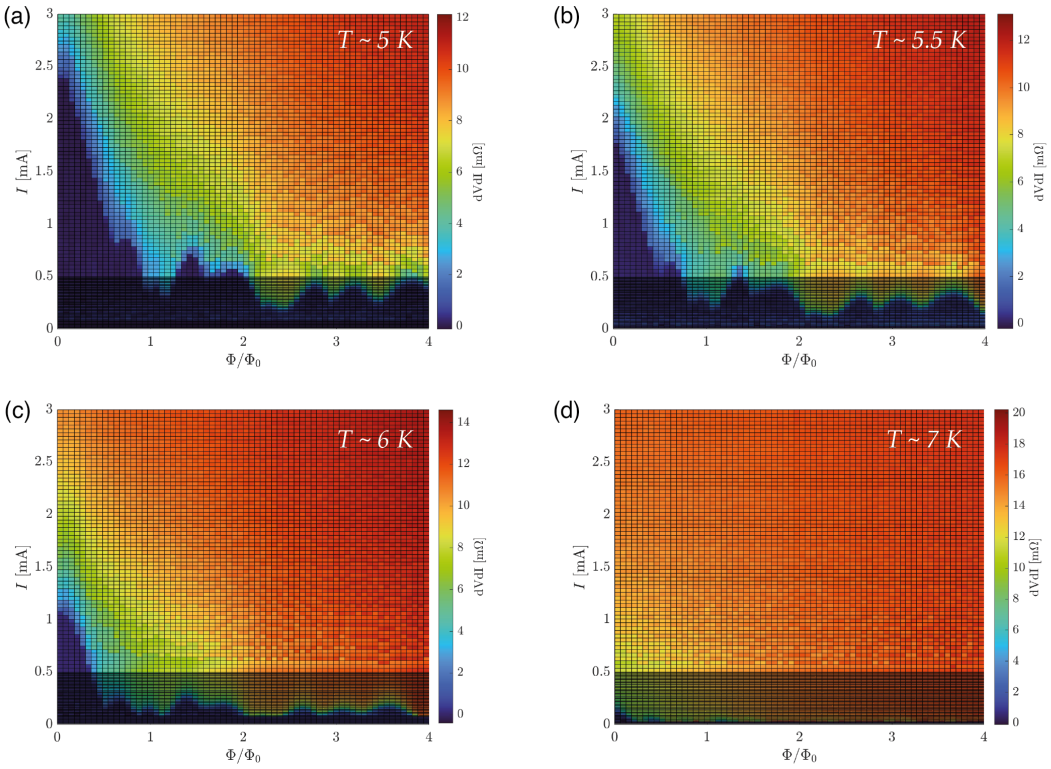

Figure 4.16: **Magnetic field dependence with temperature.** Fraunhofer oscillation patterns measured at temperatures $T \sim 5$, 5.5, 6 and 7 K in (**a-d**), respectively. The measurements are performed with no vortices present within the optical FOV ($\sim$60 μm). The distortions in the pattern persist and the amplitude of the oscillations diminish with increasing temperature.

4.4.3 Vortex imaging and transport measurements

A key aspect of this study has been implementing the SIL in order to visualise single vortices in the devices under study. Through the course of refining the intricacies of this implementation, the SIL-MOI technique was applied to smaller structures (i.e. wave guides, strips) to observe single vortices. In this section we show imaging of single vortices in the SNS junction, while simultaneously performing some IV measurements, shown in Fig. 4.17.

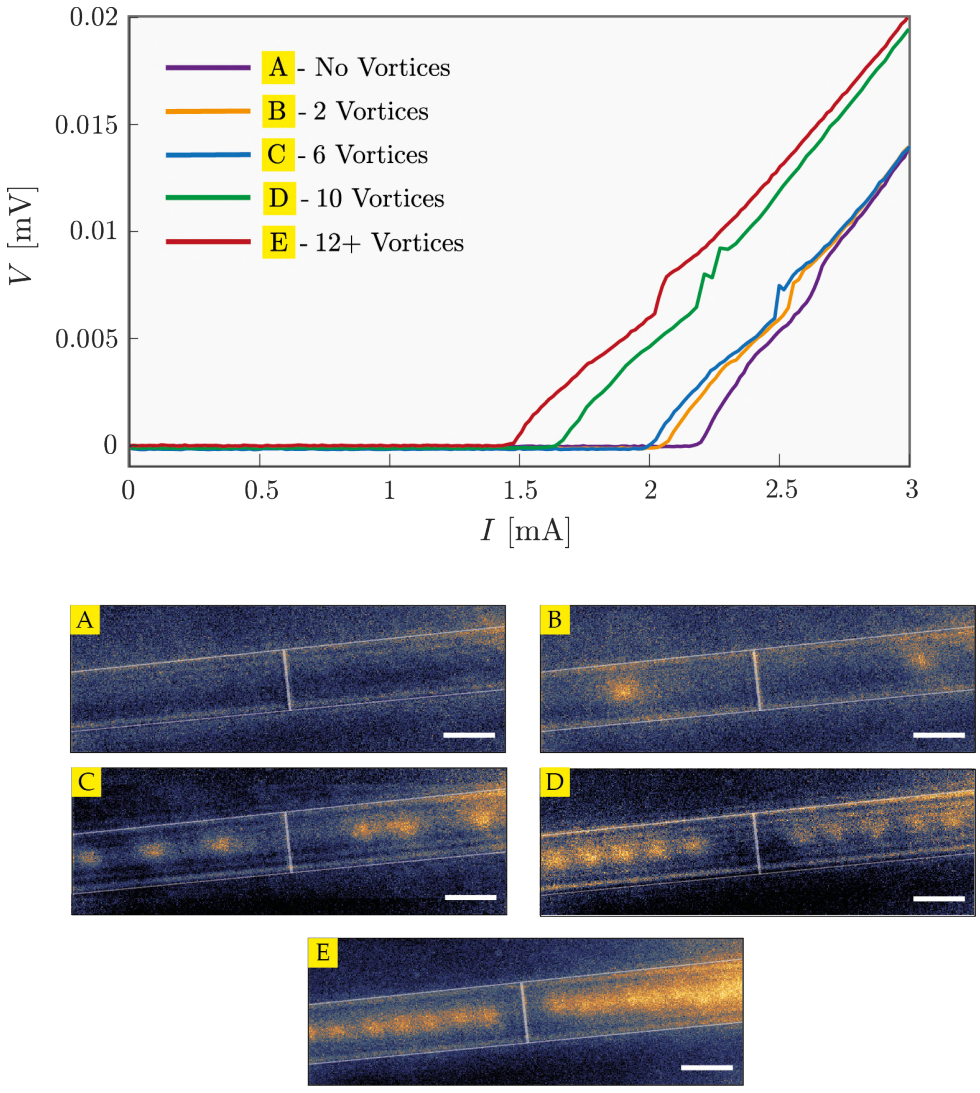

Figure 4.17: **Vortex imaging and IV measurement.** Vortex image correlated IV curves are obtained. Image (A) is cooled with a compensating field to remove the Earth's field. In images (B-E), vortices are trapped within the devices with field cooled conditions of 0.52, 0.63, 0.73 and 0.84 mT. Corresponding IV curves show changes in the I_c and difference in the shape of the transition related to the vortex distribution. The scale bars are 5 μm.

Imaging in small structures can prove challenging. Extreme care is required to assemble the sample, as the SIL is small and the physical junction must be placed under

the central region of the SIL to minimise aberrations, and maximise the resolution and contrast. Without proper handling there is a big risk of physically damaging the device as the components are shifted during assembly to ensure proper alignment. Specifically in these SNS junctions, there is a 200 nm layer of PMMA that protects the copper from oxidation, which is critical in maintaining the functionality of the device. However, this intermediate layer is detrimental to imaging quality, as the first few hundreds of nanometers is where most of the vortex flux emanates above the surface. Due to the fast diverging nature of this flux, close contact with the surface is critical to ensuring resolution and contrast. In our case, due to the necessity of this layer, a large part of our signal is lost. However, due to the SIL we are still able to image single vortices in this system due to the enhanced photon collection.

In Fig. 4.17, the device is field cooled to trap vortices at different densities and an IV curve is acquired corresponding to the vortex density in the device. In the images the junction is outlined for clarity, as the PMMA reduces the contrast of the Nb against the substrate. In image (A), the device is cooled in a field that compensates the Earth's field removing spontaneously trapped vortices within the FOV. In images (B-E), the device is cooled under fields of 0.52, 0.63, 0.73 and 0.84 mT, respectively. These fields correspond to the trapping of 2, 6, 10 and 12+ vortices cumulatively on both sides of the junction. The IV curves show a lowering of the I_c with increasing vortex density. There are also some changes in the shape and sharpness of the curves as the distribution of the vortex fields influence the subtle features of the curve.

The shifts in the IV curves correspond to a global effect of flux trapping and flux flow within the device. The entire device spans about 20 mm with Nb lines running across this distance. We can only visually verify the presence of a vortices within a relatively small region ($\sim$60 μm) around the junction. In Fig. 4.18 we monitored the vortices trapped around the junction within the FOV to correlate the applied current I_{app} to the depinning of these vortices. In principle, the depinning of the vortices should correlate to the observed critical current transition. In Fig. 4.18a., I_{app} = 3 mA, just above the device I_c observed previously. In Fig. 4.18b. , I_{app} = 6 mA and the vortices still remain pinned. In Fig. 4.18c. I_{app} = 10 mA and the vortices in the FOV are finally unpinned. From this we can conclude that since the position of the junction is the farthest physical point from the contact pads where the current is applied, there is a gradient of

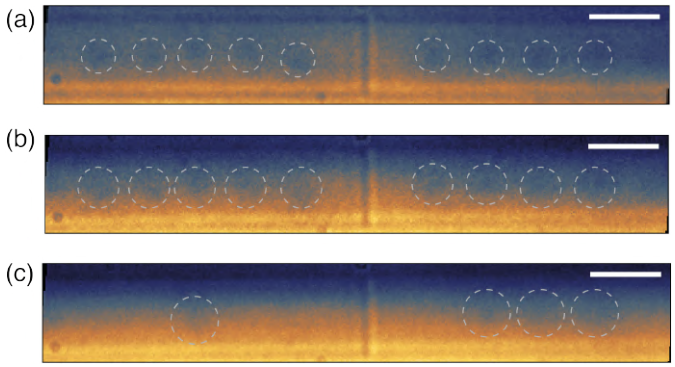

Figure 4.18: **Vortex depinning near junction.** Vortices near the junction remain pinned above the I_c determined from the transport measurement. Here MO images of the vortices (dark spots) are taken corresponding to the condition of I_{app} = (**a**) 3 mA, (**b**) 6 mA, and (**c**) 10 mA are applied. Vortices become unpinned at about 10 mA, 4 times larger than the I_c. Scale bars are 5 μm.

temperature as the current travels across these long lines. There is a 4-fold increase in current required to depin vortices in the central region. The observed I_c corresponds to flux flow in other parts of the device and does not entirely reflect changes due to the presence of vortices near the junction.

Further characterisation, correlating the images with Fraunhofer oscillation patterns and subsequently with conditions where the vortices are moved using the optical tweezers are currently limited. However, the current results are promising in going towards the direction of optical manipulation of vortices in these systems and correlating those configurations with interference measurements. It is indeed the first time that such optical image and transport correlated data has been measured.

4.5 Conclusion

During this course of this chapter, two primary avenues in optically controlled Josephson transport were explored: (1) using optical heating in the SIL configuration as a means of inducing the Josephson regime in bridge constrictions, and (2) combining SIL-MOI and transport measurements to explore the possibility of optically controlled AV to drive Josephson transport.

In the first set of experiments, a SQUID loop made from two *Dayem* bridge style weak-links are studied. Keeping the original motivation of AV-driven JJs in mind, these devices were initially used to develop this methodology. However, the devices are observed to have strong coupling in the weak-links where no Josephson effects are observed. The primary contributor to this was the larger thickness of the Nb layer, which is required for MOI. While local thinning of the weak-leak in fabrication was the next proposed step, it remains unexplored due to fabrication bottlenecks. Another method to achieve this is to *thin* the material by heating, reducing the superconducting character locally. We localised and illuminated the constriction in a SIL- based imaging set-up with a laser spot, and recorded the resulting IV curves under illumination. It was clear that at lower temperatures the coupling was too strong to completely suppress the order parameter, but at temperatures close to T_c the IV could be modulated within a range of complete suppression and recovery. For the SQUID, two laser spots fixed at the weak-links can be used to independently alter the coupling strength to access the the full range of critical currents $[0, 2i_c]$ at lower temperatures. It is clear that with controlled localised heating, conditions can be established where Josephson effects can be induced in the structure, further verified with a magnetic field dependence.

In the second set of measurements, we explore a SNS junction designed with wide electrodes allowing a large area for vortex imaging and manipulation. Imaging in small structures is a challenging task as the alignment of optical components over the small junction is necessary to maximise the imaging resolution and contrast. We were successfully able to not only image vortices in this structure, but also perform correlated IV measurements. Additionally, for the first time we were also able to perform a magnetic field dependence in a MOI-SIL configuration. The oscillation patterns observed were not ideal and most likely are a result of sharp magnetic field gradients in the environment, which will be addressed. Further refinement of this measurement is required to reduce distortions in the pattern, as it reduces the sensitivity to vortex induced changes. Additionally, the layer of PMMA on the device is detrimental to imaging quality. Although implementation of vortex manipulation can still be performed with limited imaging quality, accurate localisation of the vortex in the image will suffer. The PMMA can be removed in vacuum, but after the removal the sample must also be assembled. Operation in a clean room or vacuum box is possible, but vacuum transfer to the cryostation will be challenging. With the transport measurements and imaging functioning with an optimised device design, these initial results are promising and require a complete characterisation of this method.

Bibliography

[1] J. R. Clem. Effect of nearby Pearl vortices upon the I_c versus **B** characteristics of planar Josephson junctions in thin and narrow superconducting strips. *Physical Review B*, 84, 10 2011.

[2] S. Mironov, E. Goldobin, D. Koelle, R. Kleiner, Ph. Tamarat, B. Lounis & A. I. Buzdin. Anomalous Josephson effect controlled by an Abrikosov vortex. *Physical Review B*, 96, 2017.

[3] T. Golod, A. Rydh & V. M. Krasnov. Detection of the Phase Shift from a Single Abrikosov Vortex. *Physical Review Letters*, 104, 06 2010.

[4] S. Nagasawa, K. Hinode, T. Satoh, Y. Kitagawa & M. Hidaka. Design of all-dc-powered high-speed single flux quantum random access memory based on a pipeline structure for memory cell arrays. *Superconductor Science and Technology*, 19, 03 2006.

[5] T. Golod, A. Iovan & V. M. Krasnov. Single Abrikosov vortices as quantized information bits. *Nature Communications*, 6, 10 2015.

[6] K. Miyahara, M. Mukaida & K. Hohkawa. Abrikosov vortex memory. *Applied Physics Letters*, 47, 1985.

[7] I. S. Veshchunov, W. Magrini, S. V. Mironov, A. G. Godin, J. -B. Trebbia, A. I. Buzdin, Ph. Tamarat & B. Lounis. Optical manipulation of single flux quanta. *Nature Communications*, 7, 2016.

[8] A. Rochet, V. Vadimov, W. Magrini, S. Thakur, J-B. Trebbia, A. Melnikov, A. Buzdin, Ph. Tamarat & Brahim Lounis. On-Demand Optical Generation of Single Flux Quanta. *Nano Letters*, 9, 2020.

[9] W. Magrini, S. V. Mironov, A. Rochet, P. Tamarat, A. I. Buzdin, & B. Lounis. In-situ creation and control of Josephson junctions with a laser beam. *Applied Physics Letters*, 114, 2019.

[10] A. Gilabert. Interaction between light and superconductors. *Ann. Phys. Fr.*, 15, 1990.

[11] A. Rothwarf & B. N. Taylor. Measurement of Recombination Lifetimes in Superconductors. *Physical Review Letters*, 19, 07 1967.

[12] L. R. Testardi. Destruction of Superconductivity by Laser Light. *Physical Review B*, 4, 1971.

[13] C. Vanneste, A. Gilabert, P. Sibillot, & D. B. Ostrowsky. Dynamic behavior of optically induced superconducting weak links. *Applied Physical Letters*, 38, 1981.

[14] A. Gilabert, D. B. Ostrowsky, M. Papuchon, B. Puech & C. Vanneste. Superconducting weak links induced by optical guided waves. *Applied Physical Letters*, 31, 1977.

[15] W. H. Parker & W. D. Williams. Photoexcitation of Quasiparticles in Nonequilibrium Superconductors. *Physical Review Letters*, 29, 1972.

[16] P. Hu, R. C. Dynes & V. Narayanamurti. Dynamics of quasiparticles in superconductors. *Physical Review B*, 10, 1974.

[17] A. D. Smith, W. J. Skocpol & M. Tinkham. Quasiparticle-energy distributions in optically illuminated Al-PbBi superconducting tunnel junctions. *Physical Review B*, 21, 1980.

[18] Ting-wah Wong, J. T. C. Yeh & D. N. Langenberg. Quasiparticle-Injection-Induced Superconducting Weak Links. *Physical Review Letters*, 37, 1976.

[19] G. Dolan & J. Lukens. Properties of superconducting weak links formed by magnetically weakening a short length of a uniform aluminum film. *IEEE Transactions on Magnetics*, 13, 1977.

[20] A.F. Volkov. Weak Coupling Produced in Superconductors by Irradiation. *JETP*, 33, 1971.

[21] R. Janik, L. Morelli, N. Cirillo, J. Lechevet, W. Gregory,& W. Goodman. Effects of laser irradiation on weak link devices. *IEEE Transactions on Magnetics*, 11, 1975.

[22] V. Ambegaokar & A. Baratoff. Measurement of Recombination Lifetimes in Superconductors. *Physical Review Letters*, 10, 04 1963.

[23] Y. Enomoto & T. Murakami. Optical detector using superconducting $BaPb_{0.7}Bi_{0.3}O_3$ thin films. *Journal of Applied Physics*, 59, 1986.

[24] K. K. Likharev. Superconducting weak links. *Reviews of Modern Physics*, 51, 1979.

[25] W. J. Skocpol, M. R. Beasley & M. Tinkham. Self-heating hotspots in superconducting thin-film microbridges. *Journal of Applied Physics*, 45, 1974.

[26] N. Kumar; T. Fournier; H. Courtois, C.B. Winkelmann & A. K. Gupta. Reversibility Of Superconducting Nb Weak Links Driven By The Proximity Effect In A Quantum Interference Device. *Physical Review Letters*, 114, 04 2015.

[27] A. A. Golubov, M. Yu. Kupriyanov & E. Il'ichev. The current-phase relation in Josephson junctions. *Reviews of Modern Physics*, 76, 2004.

[28] E. Strambini, A. Iorio, O. Durante, R. Citro, C. Sanz-Fernández, C. Guarcello, I. V. Tokatly, A. Braggio, M. Rocci, N. Ligato, V. Zannier, L. Sorba, F. S. Bergeret & F. Giazotto. A Josephson phase battery. *Nature Nanotechnology*, 15, 2020.

[29] A. Buzdin. Peculiar properties of the Josephson junction at the transition from 0 to π state. *Physical Review B*, 72, 2005.

[30] A. K. Feofanov, V. A. Oboznov, V. V. Bol'ginov, J. Lisenfeld, S. Poletto, V. V. Ryazanov, A. N. Rossolenko, M. Khabipov, D. Balashov, A. B. Zorin, P. N. Dmitriev, V. P. Koshelets & A. V. Ustinov. Implementation of superconductor/ferromagnet/ superconductor -shifters in superconducting digital and quantum circuits. *Nature Physics*, 6, 2010.

[31] A. Buzdin & A. E. Koshelev. Periodic alternating 0- and π-junction structures as realization of ϕ-Josephson junctions. *Physical Review B*, 67, 2003.

[32] E. Goldobin, D. Koelle, & R. Kleiner. Tunable $\pm\phi$, ϕ_0 and $\phi_0 \pm \phi$ Josephson junction. *Physical Review B*, 91, 2015.

[33] C. C. Tsuei; J. R. Kirtley. Pairing symmetry in cuprate superconductors. *Review of Modern Physics*, 72, 10 2000.

[34] D. J. Van Harlingen. Phase-sensitive tests of the symmetry of the pairing state in the high-temperature superconductors - Evidence for $d_{x^2\text{-}y^2}$ symmetry. *Review of Modern Physics*, 67, 04 1995.

[35] G. Testa, A. Monaco, E. Esposito & E. Sarnelli. Midgap state-based π-junctions for digital applications. *Applied Physical Letters*, 85, 2004.

[36] A. I. Buzdin, L. Bulaevskii & S. V. Panyukov. Critical-current oscillations as a function of the exchange field and thickness of the ferromagnetic metal (F) in an S-F-S Josephson junction. *Sov. Phys. JETP*, 35, 1982.

[37] H. Sickinger, A. Lipman, M. Weides, R. G. Mints, H. Kohlstedt, D. Koelle, R. Kleiner & E. Goldobin. Experimental Evidence of a ϕ Josephson Junction. *Physical Review Letters*, 109, 2012.

[38] A. Buzdin. Direct Coupling Between Magnetism and Superconducting Current in the Josephson ϕ_0 Junction. *Physical Review Letters*, 101, 2008.

[39] V. V. Ryazanov, V. A. Oboznov, A. Yu. Rusanov, A. V. Veretennikov, A. A. Golubov & J. Aarts. Coupling of Two Superconductors through a Ferromagnet: Evidence for a π Junction. *Physical Review Letters*, 86, 2001.

[40] A. V. Ustinov. Fluxon insertion into annular Josephson junctions. *Applied Physics Letters*, 80, 2002.

[41] T. Gaber, E. Goldobin, A. Sterck, R. Kleiner, D. Koelle, M. Siegel & M. Neuhaus. Nonideal artificial phase discontinuity in long Josephson 0-κ junctions. *Physical Review B*, 75, 08 2005.

[42] E. Goldobin, S. Mironov, A. Buzdin, R. G. Mints, D. Koelle & R. Kleiner. Effective model for a short Josephson junction with a phase discontinuity. *Physical Review B*, 93, 2016.

[43] T. Golod, R. A. Hovhannisyan, O. M. Kapran, V. V. Dremov, V. S. Stolyarov & Vladimir M. Krasnov. Reconfigurable Josephson Phase Shifter. *Nano Letters*, 21, 2021.

[44] T. Golod, A. Pagliero & V. M. Krasnov. Two mechanisms of Josephson phase shift generation by an Abrikosov vortex. *Physical Review B*, 100, 11 2019.

[45] V. M. Krasnov. Josephson junctions in a local inhomogeneous magnetic field. *Phys. Rev. B*, 101, 2020.

[46] V. G. Kogan. Coherence length of a normal metal in a proximity system. *Phys. Rev. B*, 26, 1982.

[47] K. K. Likharev. *Dynamics of Josephson Junctions and Circuits*. CRC Press, 1986.

[48] V.M. Krasnov, O. Ericsson, S. Intiso, P. Delsing, V.A. Oboznov, A.S. Prokofiev & V.V. Ryazanov. Planar S–F–S Josephson junctions made by focused ion beam etching. *Physica C*, 418, 2005.

Chapter 5

Conclusions and perspectives

5.1 Conclusions

The work produced in this thesis was motivated by the larger idea of optically driven transport in superconducting devices. In the first part of this work, we developed a solid immersion lens (SIL) integrated magneto optical imaging (MOI) set-up that allowed us to image single vortices below the sub-micron scale. This addressed the critical bottleneck in optical imaging resolution of single vortices. Having already developed techniques to optically displace and generate single vortices, the resolution enhancement via this SIL based technique beautifully integrates all these techniques for application at the physical scale of superconducting devices. The second part of this work is broken into two parts: (i) the application of the SIL to perform some optical patterning in an attempt to locally *thin* the superconducting condensate to create a weak-link, and (ii) using the SIL-MOI method for simultaneous visualisation of vortices and acquisition of transport measurements in Josephson devices. This is the first time such measurements have been performed. These results bring us closer to the realisation of completely optically driven Josephson transport.

While there are several methods used to visualise vortex structures in superconductors, MOI provides a far-field method that provides the capability of capturing dynamic processes, and is easily implemented. However, it is limited by its low imaging resolution as compared to other techniques. The imaging is indirect via the Faraday effect and is achieved with use of a high-refractive index magneto-optical indicator ($n \sim 1.97$) pressed on top of the superconductor. By introducing a solid immersion lens (SIL) with $n \sim 2$ on top of the indicator, the transition of the illuminating beam from a high-refraction medium into air is eased, thus reducing refraction and maximising collection into the coupling aspheric lens [1, 2]. By exploiting the aplanatic point in the super-hemisphere geometry we were able to achieve a 3.2$\times$ enhancement of a potential $n^2 = 4$ in effective numerical aperture (NA) to obtain an imaged single vortex resolution of 583 nm. This is the best reported resolution for this optical technique. The enhanced resolution allows the visualisation of single vortices at high densities which were previously unresolvable by the conventional technique. Since the imaging method is based on detecting the change in polarisation angle due to a vortex via Faraday rotation, preserving polarisation quality was critical in ensuring contrast. An increasing NA has the inherent effect of distorting the polarisation profile. This leads to degradation in the

imaging quality. However, there exists an optimal $NA \sim 0.4 - 0.5$ where high resolution (sub-micron) can be achieved without perceptible loss of contrast. The enhanced photon collection compensates for increasing polarisation degradation. The conception of this technique provides a platform for studies beyond our motivation of application to Josephson devices, but can be used to optically resolve vortices to study real-time vortex-vortex interactions at high densities. There are further improvements that can be made to this method such as reducing the air-gap between the superconductor and indicator where vortex flux is lost. While the deposition of niobium on the indicator is a challenging exercise in fabrication, producing a high quality film would result in a further enhancement closer to the theoretical SIL enhancement of n^2.

In pursuit of the optically manipulated vortex driven Josephson junction, we initially used a SQUID, where the device dimensions, i.e. electrode width, contact lines and niobium thickness, were all designed to accommodate the integration of MOI and optical manipulation. However, these devices based on the *Dayem*-bridge weak-link structure displayed strong coupling due to the larger thickness of the film, and no Josephson coupling was observed. To maximise the use of these devices we proposed two methods to modify the device to weaken the coupling, (i) in the process of fabrication of future devices, the weak-link area would be locally etched to physically thin the niobium while preserving the thickness in the electrodes as required for imaging, and (ii) attempt a simple patterning technique to optically thin the weak-link area by locally heating the region with a tightly focused laser spot [3]. Due to logistical challenges the fabrication method could not be explored, but leaves room for future investigation. Using the SIL, a confocal image was mapped, and the weak-link was localised to allow heating of the region and full suppression and recovery of the superconducting state was observed in the current-voltage (IV) data. Due to the strong coupling, the full range of suppression could not be accessed at lower temperatures within the range of laser heating. A curious point in these measurements was the complete suppression of the superconducting state while only one weak-link was illuminated. A SQUID with two parallel weak-links can be treated as a circuit with two resistive elements in parallel, where the total critical current $I_{tot} = i_{c1} + i_{c2}$, and $i_{c1/2}$ are the respective critical currents of the two weak-links. Therefore, while illuminating one weak-link the maximum suppression should be $1/2I_{tot}$. However, this complete suppression is only observed near T_c where it is possible that there is heat transfer around the SQUID loop through the niobium and the observed effect is not stemming from an isolated weak-link but is a cumulative effect of the device. To isolate the effects just from heating the weak-links, two independent laser spots can be focused on each of the weak-links at low temperatures. This will allow us to independently control the coupling strength in each of the weak-links and discern their respective contributions to I_{tot}. Refining this method will allow real-time creation of Josephson coupling, with the possibility of modulating the coupling strength and symmetry of the weak-links. It has been shown that the SQUID devices based on high-temperature superconductors show reduced noise levels with asymmetric weak-links [4], so dynamic tunability has practical implications on device performance. Further investigation of this phenomenon is still limited due to unavailability of these devices.

Following this, we pivoted to a different system, a planar SNS Josephson junction. The design configuration of this device eliminated the challenges experienced with the SQUID, and provided the proper dimensions for imaging and Josephson coupling. Us-

ing the SIL-MOI set-up we were able to image single vortices in a field of view (FOV) of 60 μm around the junction. Under different field cooling conditions, the density of vortices was varied and corresponding IV curves were obtained. With increasing density of vortices the IV curves showed lowering of the critical current, which is an expected behaviour as critical current corresponds to the appearance of a finite voltage due to vortex motion. However, vortex motion around the junction is only observed upon increasing the applied current up to 4 times larger than the observed current transition. Due to the clearance required around the junction area to integrate the imaging set-up, the niobium lines from the contact pads to the junction are long ($\sim$10 mm). The temperature gradient developed in these long lines causes depinning of vortices near the contact pads first, followed by depinning moving into the central region with increasing current. This leads to the broad critical transitions we observed. Compensating for stray fields by field-cooling the sample can help reduce global trapping of vortices, but it cannot be avoided when we required vortices near the junction. In general, optical tweezers can be used to clean an area in the FOV, but cannot be extended into the outer lines. While maintaining no vortices within the FOV, verified by MOI, magnetic field dependence measurements were performed and show the characteristic oscillation pattern. This was an important measurement to verify the operation of the device in Josephson regime. There are some distortions in the outer periods which can be a product of sharp gradients of magnetic field in the environment. The addition of magnetic coils along the other two axes should help compensate for these stray fields and eliminate these distortions, and will be part of the next series of improvements to the set-up. This is the first demonstration of MOI combined with transport measurements, and these first results are promising in moving towards vortex manipulation in this system to induce phase shifts in the Josephson ground state.

5.2 Perspectives

5.2.1 Optically driven Josephson junction

The catalogue of optical methods previously developed in the group, in addition to the strides made in this thesis, bring us closer to the realisation of optically driven Josephson transport. There are two main avenues of exploration that should follow this work:

1. With all tools in place, some modifications to the transport measurement set-up should ensure sufficient isolation from stray fields. Following this, optical tweezers can be implemented to modify the vortex-junction proximity and the subsequent phase shifts should be confirmed in the Fraunhofer oscillation pattern. As schematically illustrated in Fig. 5.1a., this system does not require pre-fabricated pinning sites to set the location of the vortex, therefore, has the ability to access arbitrary phase shifts in real-time.Using the Kibbel-Zurek mechanism several vortices can be generated [5], and with the introduction of multiple independent laser spots, these vortices can be independently manipulated in the electrodes to allow complex encoding of information.

2. Further investigation and testing of optical patterning configurations should be conducted to characterise the optical heating parameters required to produce steady-state conditions resulting in Josephson coupling. The application of this methodology would allow for dynamic creation of Josephson junctions [3], SQUID-like structures (Fig. 5.1b.), and could be scaled up to create multiple junctions. A key advantage of this method is that since the constriction is not physical, the device is more robust against damage due to electrostatic discharge, as we've experienced with the *Dayem* bridge structures.

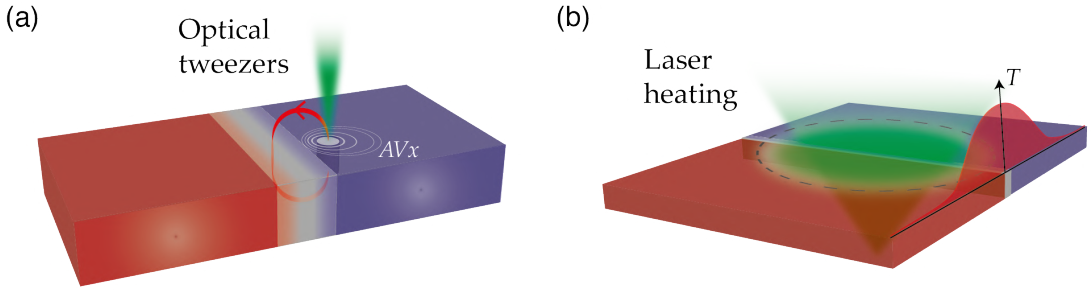

Figure 5.1: **Optical manipulation and creation of Josephson junction.** (**a**) Schematic illustration of a Josephson junction with an optically manipulated vortex. Pre-fabricated trapping sites are not required and an arbitrary phase can be accessed in real-time. (**b**) An optically created SQUID structure made from a planar junction. With sufficient rise in temperature over a large area, a loop structure can be created. The structure persists under illumination and returns to its original configuration when illumination is turned off.

5.2.2 Magneto-optical imaging of vortices in high-T_c superconductors

In terms of practical technological applications, high-T_c superconductors (HTS) provide a clear advantage in cooling cost. It is far less expensive to liquefy nitrogen and it has a much greater cooling capacity than liquid helium. For any application in which liquid nitrogen can replace liquid helium, the refrigeration cost is about 1000 times less. Conversely, the cuprate-based ceramic HTS have a few drawbacks. The materials tend to be very brittle, like most ceramics, and do not carry enough current for useful application. Making supple bendable wires that don't induce too much strain is a heavily researched engineering problem. A more important drawback is that the magnetic properties of these materials vary greatly from the conventional metallic low-T_c superconductors (LTS). Weaker flux pinning at high temperatures makes the sustainable critical fields low. However, if these ceramic materials are operated at low temperatures (4-20K), they show the ability to stay superconducting under large fields. Therefore, for applications requiring large currents, it is better to use the ceramic superconductors at lower temperatures [6].

While HTS systems still have challenges that need to be overcome for large scale implementation, the advantages of using this system are not trivial. The optical methods that we've developed work in conjunction with magneto-optical imaging. Application of this imaging method is limited for HTS materials for reasons that will be elucidated upon. However, if a method can be developed to optically visualise vortices in HTS materials, all the other optical methods can be integrated to control transport behaviour in HTS devices. In the brief proof of concept presented here, we use YBCO as the HTS system under test. Here, we combine a LTS (Nb) and HTS (YBCO) material to optically image vortices in YBCO. There is no equivalent report where single vortices in YBCO have been imaged via MOI.

5.2.2.1 High-T_c superconductors

Crystal structure

The crystal structure of HTS materials is relatively more complex and is a major determinant of both its mechanical and electrical properties, especially superconductivity. In comparison, LTS materials have simpler structures and have essentially no structural effects on their properties. Cuprate HTS materials are variations of the crystal type known as *perovskites*, which tend to have a chemical formula of the type ABO_3. We will limit our discussion as it pertains to YBCO [6]. A key feature of this unit cell, as is the case with other layered cuprate superconductors, is the presence of two layers or planes of CuO_2. The CuO_2 plane is termed the *conduction plane*, and this is where superconductivity occurs. The outermost plane of the cell is a copper oxide region with missing oxygens and is known as a copper oxide chain. The missing oxygens are very important in $YBa_2Cu_3O_{7-x}$ as the x refers to the fraction of missing oxygen. When $x = 0.15$, T_c is maximised near 92K, and at $x \approx 0.7$ superconductivity is nonexistent. The role of oxygen is instrumental in controlling the superconductive properties of YBCO.

Vortex matter in HTS materials

The layered structure of HTS compounds carries with it an expected anisotropy since electron mobility is directionally dependent. This anisotropy affects the superconductive properties, as the coherence length tends to be very small, on the scale of a few interatomic spacing, and the penetration depth tends to be very large, on the scale of a few thousand interatomic spacing.

Applications using type-II materials operate in the mixed state to maximise the operating currents and fields. The flow of dissipation-free current in a superconductor is limited by the depinning current j_p, where the current becomes large enough to cause vortex motion by the Lorentz force F_L, thus dissipating power. The Lorentz force is countered by the pinning force f_{pin}. The pinning force density is given as $\mathcal{F}_{pin}(L) \simeq \sqrt{f_{pin}^2 n_i \xi_c^2 L}$, where n_i is the density of the pinning defects, f_{pin} is the individual pining force of the defects, and L is the segment length of the flux line on which these forces act on [7]. The pinning potential landscape in a pristine HTS is set by intrinsic pinning centers due to oxygen and copper vacancies which have sizes below the order of magnitude of ξ_c, which makes $\mathcal{F}_{pin}$ very weak. The random pinning forces add up in a stochastic manner, giving a net total force that increases as $\sqrt{n_i}$. Therefore the pinning landscape of the sample must be optimised to maximise the critical current-density ratio j_p/j_{dp}, where j_{dp} is the depairing current where superconductivity vanishes. Thermally activated motion of flux lines can occur even at $j < j_p$ as the thermal energy proves sufficient to overcome the pinning barriers, leading to vortex creep. Thermal disorder smooths the pinning potential, thereby reducing the depinning current of the system [8].

With these governing parameters in mind we can begin to understand the systemic differences in LTS and HTS materials. In a conventional pristine defect-less LTS the pinning is usually strong, $j_p/j_{dp} \simeq 10^{-2} - 10^{-1}$, whereas opposing thermal fluctuations are weak. In contrast, HTS materials like YBCO tend to have weak pinning strength $j_p/j_{dp} \simeq 10^{-3}$, whereas thermal fluctuations are strong. The material properties of HTS materials accentuate thermal fluctuations making intrinsic pinning weak. However, when considering extrinsic pinning due to implanted defects such as nanoparticles, strain, stacking faults, and twin boundaries, the pinning strength is orders of magnitude larger. By lowering the operational temperature, the fluctuations can be suppressed and the overall pinning strength can be increased dramatically, resulting in sustaining of high critical fields [7].

Vortex elasticity

Due to the fact that superconductivity only exists in the CuO_2 planes, the superconductive properties along the *c*-axis are suppressed. The current density parallel to the CuO_2 along the *ab*-plane is much higher than the current flowing along the *c*-axis. This also manifests in the way flux is trapped in these structures. This relates directly to the separation distance between the CuO_2 planes and the electronic coupling between them. In YBCO the superconducting planes are separated by a distance $\sim 2\xi_c$, so the order parameter is not fully suppressed and the flux line is coupled between the planes and experiences a local re-trapping within the unit cell. In bismuth, mercury or thallium

based cuprates the separation distance between the superconducting planes is much larger than $2\xi_c$ and the vortex is broken, undergoing a 2-dimensional distribution of flux, so called "pancake vortices".

As discussed previously in the context of pinning, we can consider the vortex as an elastic object that has point defects, i.e., oxygen vacancies, acting on it to pin the flux line. This pinning force competes with a collective Lorentz force $\mathcal{F}_L(L) \simeq j\Phi_0 L$ due to a flowing current. Here L is the length of segment of the vortex subjected to this force. The Lorentz force has a linear dependence on the distance L, while the pinning only has a $\sqrt{L}$ dependence due to the random addition of pinning forces. This implies that over a large distance, the Lorentz force always overpowers the pinning, so a stiff vortex would not be pinned. However, due to the weakness of these defects, the vortex can reorient itself as accommodated by the pinning potentials and experience elastic deformation. Such a deformation will cost an elastic energy $\mathcal{E}_{el} \simeq \epsilon_l(\xi_c/L)^2 L$, which competes with the pinning energy $\mathcal{E}_{pin} \simeq \mathcal{F}_{pin}(L)\xi_c$. As previously, ϵ_l refers to the vortex line energy or the line tension within the paradigm of treating vortices as elastic objects. There exists a critical deformation length L_c, where $\mathcal{E}_{el}(L_c) \simeq \mathcal{E}_{pin}(L_c)$, which defines the maximum deformation sustainable before the vortex breaks into various segments [7]. In HTS materials where the crystalline structure is anisotropic, the vortex line energy or line tension is expressed along the two axes.

$$\epsilon_l^{\perp} \approx \Gamma \frac{\Phi_0^2}{4\pi\mu_0\lambda_{ab}^2}, \qquad \epsilon_l^{\parallel} \approx \frac{1}{\Gamma}\frac{\Phi_0^2}{4\pi\mu_0\lambda_{ab}^2} \tag{5.1}$$

where Γ can also be obtained as $\Gamma = \lambda_c/\lambda_{ab} > 1$. Here λ_{ab} and λ_c are the London penetration depths in the *ab*-plane and along the *c*-axis, respectively. These values for YBCO are on the order of $\lambda_{ab} \sim 750$ nm and $\lambda_c \sim 150$ nm, depending on the sample and type of measurement used to determine the values [9]. This gives an anisotropy parameter $\Gamma \sim 5 - 6$. Due to the relatively low anisotropic character of YBCO, a low angle tilt can be induced within the structure deforming it in the manner explained in this section. In highly anisotropic HTS, artificial deformation resulting in controllable bending [10], cutting and reconnecting [11, 12], or tangling [13, 14] has been proposed.

5.2.2.2 Magneto-optical imaging in HTS materials

The impediment to implementing the MOI technique to HTS materials is the background subtraction scheme. In general, the vortex images are acquired by subtracting an image taken at $T < T_c$ from a background image taken at $T > T_c$. For LTS materials like Nb, the temperature difference between these two images is minimal, the background is taken at 10K, while the vortex image is taken at 4K. However, for a HTS material like YBCO the background image has to be taken above 90K ($> T_c$), while the vortex image should be taken below 20K. Below T_c of YBCO flux is indeed trapped, but the vortex size is larger at elevated temperatures and the vortex field becomes less concentrated. We can estimate the vortex size at different temperatures by using familiar dependence of the penetration depth on temperature $\lambda_L(T) \approx \lambda_{L,0}/\sqrt{1-(T/T_c)^4}$. At 70K the vortex size is ~ 235 nm, while at 10K it is ~150 nm. So in order to minimise the vortex size and concentrate the field, a lower temperature is necessary to maximise imaging sensitivity. During the cooling process there are mechanical shifts in the stage and metallic components of the sample holder which misaligns the relative physical positions of the two images. Additionally, due to these moving parts during cooldown the piezo stage defocuses the image. Now the vortex image cannot be subtracted from the background image, which makes the background subtraction scheme unusable. Another method to circumvent this problem is break superconductivity by applying a large enough current, depairing current, and then trap vortices followed by a rapid cooling of the superconducting condensate. While this may address the thermally induced mechanical misalignment, the depairing current density in YBCO is quite large (~300 MA/cm^2 at 4.2K). This would cause severe heating and breaking of the wires and electrodes. Therefore, both approaches present their own specific limitations.

Flux re-trapping

An interesting approach to address this problem is to use a LTS material as a flux re-trapping layer [15].The sample consists of a 170 nm YBCO film deposited on sapphire is capped with a 100 nm intermediate layer of gold, followed by the deposition of a 100 nm Nb film. The thicknesses of the superconductors are all at the scale of their respective penetration depths. The role of the intermediate layer is to ease the lattice mismatch between the two materials. The samples for this measurement were fabricated in *Unité Mixte de Physique CNRS/Thales* in Palaiseau.

Ideally, direct deposition of the capping Nb layer on the garnet indicator or YBCO film would provide the ideal sample, as we could preserve the signal lost due to flux divergence over the thickness of the spacer layer. However, through our own trials with deposition of Nb on garnet indicators and YBCO films, the deposited Nb film can be porous, lacks a smooth morphology and does not stick well to the material. These factors severely deteriorate the vortex trapping and subsequent imaging capability. Therefore, the necessity of a spacer material is important and preparing the sample structure in this manner ensures film quality ideal for imaging. Using this sample, flux re-trapping can be used to image vortices. The process is illustrated in Fig. 5.2.

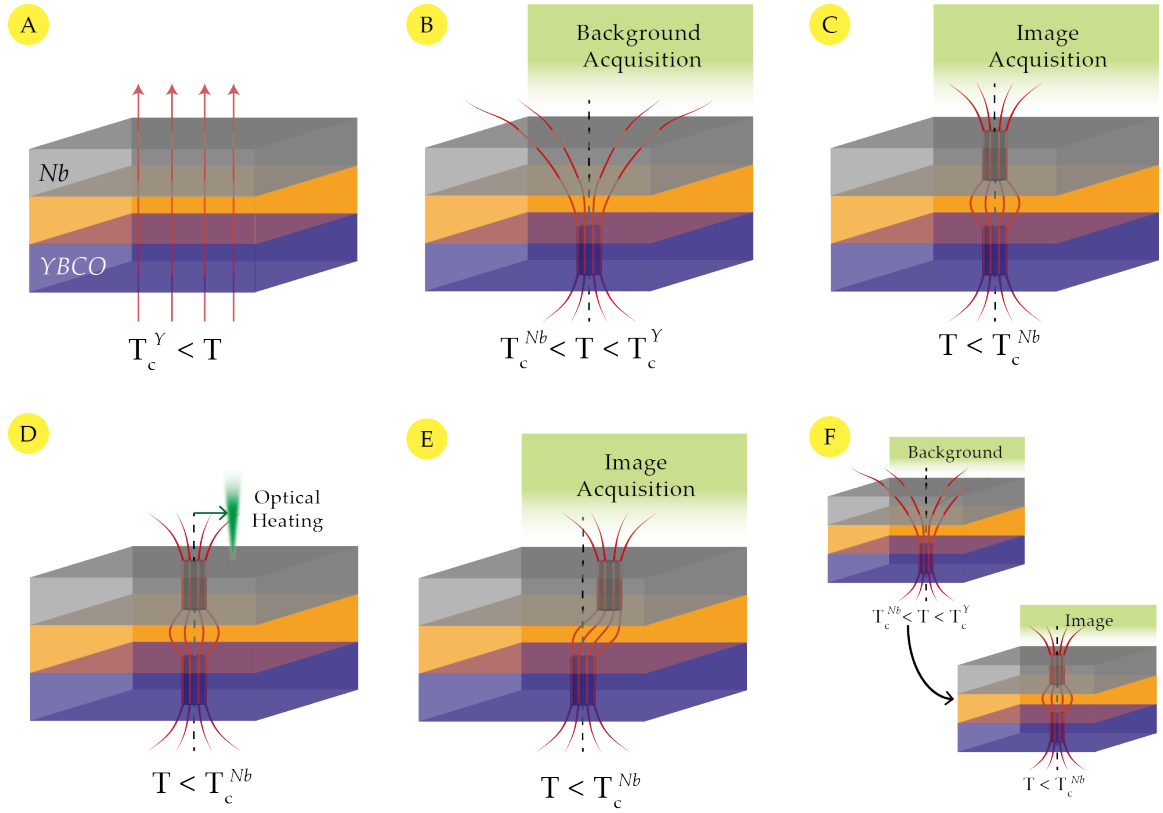

Figure 5.2: **Flux re-trapping mechanism.** (A) At $T > T_c^Y$, the magnetic field passes through the layers of superconductors unhindered. (B) Flux gets trapped in the form of vortices in the YBCO film when the temperature is below T_c^Y at 86K. At 10K, these vortices are strongly pinned and a background acquisition is taken above T_c^{Nb}. (C) When cooled below T_c^{Nb}, the previously diverging flux is re-trapped in the Nb film as a vortex once again. The image is acquired with background subtraction to visualise the vortex in the Nb film. (D) A focused laser spot is placed at the center of the FOV. (E) The laser spot displaces the vortices in the Nb layer, revealing the underlying flux from the YBCO vortex that is present in the background. The position is indicated by the dotted line. (E) When heated above T_c^{Nb} and cooled back down to re-trap the vortices in Nb, the vortices return to their original position.

MOI of HTS structure

As the temperature cools down through the T_c^Y of YBCO, flux becomes trapped as vortices. The vortex flux then diverges above the surface of the YBCO. This flux can be re-trapped using a capping layer of Nb placed on top of YBCO and the background subtraction scheme can be applied. Following the visualisation of vortices in Nb via the Nb/YBCO structure, the optical tweezers technique is applied and the thermal force displaces the Nb vortices to form a cluster, as shown in Fig. 5.3a-b. The displaced vortices leave dark spots marking their previous position. The dark spots actually are a signature of the signal from YBCO vortices that is present in the background image as diverging flux. When the image of the displaced vortices is subtracted from the background image, this signature reveals itself. By characterising the profiles of the Nb (light) and YBCO (dark) vortices, a FWHM of the Nb vortex is 1.8 μm characteristic of

conventional MOI in Nb, while the size of the YBCO vortex is larger at 2.6 μm which correlates to enlarged vortex size due to the divergence of flux ~100 nm above the surface of the superconductor. Upon warming up the sample above T_c^{Nb} and cooling down again to image the same area, all the vortices have returned to their original position, seen in Fig. 5.3c. Comparing this to images of displacement of vortices in a sample of sapphire and Nb in Fig. 5.3d-e., there are no dark spots and no such signature present. We conclude that we are indeed observing flux signal from the underlying vortices.

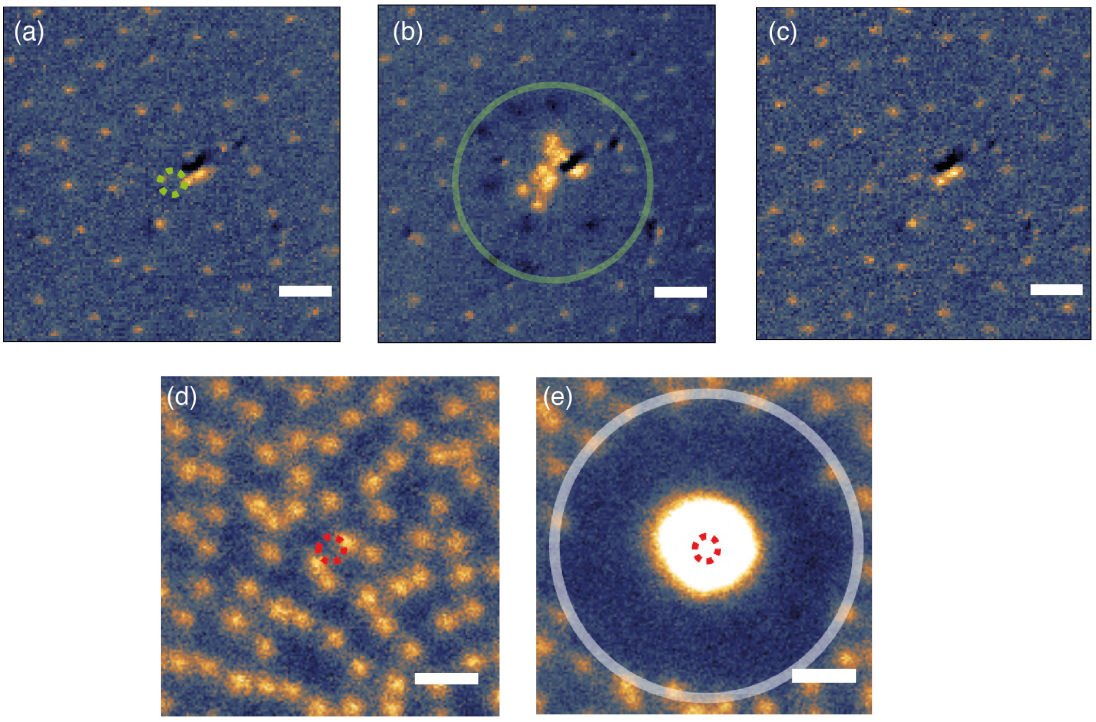

Figure 5.3: **Vortex displacement in Nb/YBCO.** (**a**) A focused laser spot is placed at the center of the FOV. (**b**) The laser spot displaces the vortices in the Nb layer, revealing the underlying flux from the YBCO vortices (dark) that is present in the background. (**c**) When heated above T_c^{Nb} and cooled back down to re-trap the vortices in Nb, the vortices return to their original position. This is compared to displacement of vortices in a sample with just Nb, before vortex displacement (**d**) and after displacement (**e**). No signature such as the dark spots are observable. The scale bars are 10 μm.

Here we showed magneto-optical imaging of vortices in a Nb capping layer on top YBCO. These initial results have allowed us to, firstly, observe the flux initially trapped in YBCO at 86K, as it traverses into Nb and is re-trapped below 8.6K, where it is imaged in Nb. The continuous vortex forms two separate segments in the respective LTS and HTS layers, that are electromagnetically coupled. Secondly, the vortex segment in Nb is displaced to reveal the vortex flux emanating from YBCO, which is in the background signal. This allows us to indirectly observe for the first time single vortices in an HTS material using the MOI technique.

Since the spontaneous distribution of vortices visualised in Nb is correlated to the pinned vortices in the YBCO layer. The vortex segment in YBCO can also be displaced by the optical tweezers. While not being able to directly visualise the YBCO vortex,

the position of the vortex can be discerned due to the vortex distribution in Nb. By carefully aligning the position of the focused laser on the backside of the sample, at the surface of YBCO, the vortex segment in YBCO can be displaced. Following this, the system can be heated up above T_c^{Nb} and cooled back down to image the new displaced vortex distribution. The imaging and ability to displace vortices in the Nb or YBCO layer extends the application of our optical methods to HTS devices.

Additionally, more fundamental studies on vortex interactions can be performed. The facile implementation of the optical tweezers technique is an advantage over the use of an MFM set-up [10]. The step precision of the laser movement can be controlled by the stability of the laser source and voltage discretisation of the galvo mirror system. With this, measurements in vortex bending, cutting, twisting and tangling can be performed with great precision. Further measurements are required using alternate non-metallic spacer materials. Using aluminum oxide or other insulators would allow the structure to mimic a device-like configuration and electrodes can be added to observe transport behaviour, while simultaneous imaging and manipulation is performed. It is also important to quantify the displacement force as a function of displacement distance. This will not only provide us information regarding practical parameters regarding vortex manipulation, but also on the elastic tension in the vortex line in different media.

Bibliography

[1] Mansfield, S. M. & Kino, G. S. Solid immersion microscope. *Applied Physics Letters*, 57, 1990.

[2] G. S. Kino, Gordon S. & Y. B. Band. SPIE Proceedings [SPIE Optoelectronics '99 - Integrated Optoelectronic Devices - San Jose, CA (Saturday 23 January 1999)] Optical Pulse and Beam Propagation - Applications and theory of the solid immersion lens. volume 3609, 1999.

[3] W. Magrini, S. V. Mironov, A. Rochet, P. Tamarat, A. I. Buzdin, & B. Lounis. In-situ creation and control of Josephson junctions with a laser beam. *Applied Physics Letters*, 114, 2019.

[4] U. Sinha, A. Sinha & F. K. Wilhelm. Improving high-T_c dc SQUID performance by means of junction asymmetry. *Superconductor Science and Technology*, 22, 2009.

[5] A. Rochet, V. Vadimov, W. Magrini, S. Thakur, J-B. Trebbia, A. Melnikov, A. Buzdin, Ph. Tamarat & Brahim Lounis. On-Demand Optical Generation of Single Flux Quanta. *Nano Letters*, 9, 2020.

[6] T. P. Sheahen. *Introduction to High-Temperature Superconductivity*. Springer, 2002.

[7] G. Blatter, M. V. Feigel'man, V. B. Geshkenbein, A. I. Larkin, & V. M. Vinokur. Vortices in high-temperature superconductors. *Reviews of Modern Physics*, 66, 1994.

[8] E. H. Brandt. The flux-line lattice in superconductors. *Reports on Progress in Physics*, 58, 1995.

[9] A. K. Saxena. Crystal structure of high temperature superconductors. In *High-Temperature Superconductors*, chapter 2, pages 43–60. Springer, 2012.

[10] O. M. Auslaender, L. Luan, E. W. J. Straver, J. E. Hoffman, N. C. Koshnick, E. Zeldov, D. A. Bonn, R. Liang, W. N. Hardy K. A. Moler . Vortex cutting in superconductors. *Nature Physics*, 5, 2008.

[11] H. Safar, P. L. Gammel, D. A. Huse, S. N. Majumdar, L. F. Schneemeyer, D. J. Bishop, D. López, G. Nieva, & F. de la Cruz. Observation of a nonlocal conductivity in the mixed state of $YBa_2Cu_3O_7$: Experimental evidence for a vortex line liquid. *Physical Review Letters*, 72, 1994.

[12] A. Glatz, V. K. Vlasko-Vlasov, W. K. Kwok, and G. W. Crabtree. Vortex cutting in superconductors. *Physical Review B*, 94, 2016.

[13] David R. Nelson. Vortex Entanglement in High-T_c Superconductors. *Physical Review Letters*, 60, 1988.

[14] C. J. Olson Reichhardt & M. B. Hastings. Do Vortices Entangle? *Physical Review Letters*, 92, 2004.

[15] M. Tokunaga, T. Tamegai & T. H. Johansen. Improvement of vortex imaging in magneto-optical technique and Bitter decoration. *Physica C*, 437-438, 2006.

Abstract

Superconducting circuits have high operating frequencies, low switching energies, and intrinsically generate less heat allowing denser packing than its semiconducting equivalent. Abrikosov vortices represent the most compact magnetic nano-objects in superconductors, on the scale of $\sim$100 nm. They can be used to engineer the desired ground state phase of a Josephson junction to control the throughput current by modifying the proximity of the vortex to the junction. In our group we have developed optical methods to create, image and manipulate single vortices at high rates at the sub-micron scale. Moreover, using optical patterning techniques, junction-like structures can be created by local weakening of the superconducting condensate by optical heating. These methodologies provide an avenue for complete optical control of Josephson transport, with the potential for large scale implementation. The work of this thesis builds on these previously developed techniques. We firstly address a bottleneck due to optical imaging resolution. We have developed a magneto-optical imaging setup based on a hemispherical solid immersion lens (SIL) leading to sub-600 nm optical resolution of single Abrikosov vortices. This represents a three-fold improvement in the resolution with respect to single lens imaging systems. While the initial motivation of this new implementation was optical imaging of single vortices in smaller structures, this method will also allow the study of vortex lattice interactions, where inter-vortex distances can be a few hundred nms. Using this method, we have been successfully able to resolve single vortices in device electrodes, which has allowed real-time optical observation of single vortices correlated with transport measurements. The optical manipulation techniques can be further applied to control vortex position without the need for pre-fabricated vortex pinning sites, allowing access to a full dynamic range of phase shifts for complex operations. The SIL has also allowed us to localise subtle structures of the device geometry to perform optical heating to modify the superconducting properties. The modulation of the transport properties by heating can be quantitatively correlated to changes in the density of Cooper pairs in the heating volume. Additionally, vortices in high-temperature superconductors (HTS) have also been optically imaged and manipulated for the first time. The method employed here uses a flux re-trapping mechanism where the vortices in the HTS are imaged through a low-Tc superconductor that is deposited on top. This opens up avenues for studying unique vortex interactions like twisting and cutting, and further application of optical techniques to drive transport behaviour in HTS devices.

Keywords: superconductivity, Josephson junction, magneto-otpical imaging, Abrikosov vortex

Résumé

Les circuits supraconducteurs ont des fréquences de fonctionnement élevées, de faibles énergies de passage, et génèrent intrinsèquement moins de chaleur permettant des configurations plus denses que ses équivalents semi-conducteurs. Les vortex d'Abrikosov sont les nano-objets magnétiques les plus compacts dans les supraconducteurs, à l'échelle de $\sim$100 nm. En modifiant la distance entre un vortex et une jonction Josephson, ils peuvent être utilisés pour créer la phase désirée de l'état fondamental afin de contrôler le courant de passage. Au sein notre groupe, nous avons développé des méthodes optiques permettant de créer, d'imager et de manipuler des vortex uniques à des vitesses élevées et à l'échelle submicronique. De plus, en utilisant des techniques de modelage optique, des structures analogues à une jonction peuvent être créées par affaiblissement local du condensat supraconducteur par chauffage optique. Ces méthodes offrent une possibilité de contrôle tout-optique du transport Josephson, avec un potentiel de mise en œuvre à grande échelle. Le travail de cette thèse s'appuie sur ces techniques précédemment développées. Nous abordons tout d'abord la difficulté liée à la résolution de l'imagerie optique. Nous avons développé une configuration d'imagerie magnéto-optique basée sur une lentille hémisphérique à immersion solide (SIL) permettant une résolution optique inférieure à 600 nm de vortex d'Abrikosov uniques. Cela représente une amélioration par trois fois de la résolution par rapport aux systèmes d'imagerie à lentille unique. Si la motivation initiale de cette nouvelle mise en œuvre était l'imagerie optique de vortex uniques dans des structures plus petites, cette méthode permettra également d'étudier les interactions dans les réseaux de vortex, où les distances inter-vortex peuvent être de quelques centaines de nm. En utilisant cette méthode, nous avons réussi à résoudre des vortex uniques dans des électrodes de circuits, ce qui a permis l'observation optique en temps réel de vortex uniques, corrélée avec des mesures de transport. Les techniques de manipulation optique peuvent être appliquées au contrôle de la position des vortex sans avoir recours à la préfabrication de sites de fixation des vortex, permettant d'accéder à une gamme dynamique complète de différences de phase en vue d'opérations complexes. La SIL nous a également permis de modifier les propriétés supraconductrices d'appareils par chauffage optique, en localisant des structures fines jusqu'ici non discernables. La modulation des propriétés de transport par chauffage peut être corrélée quantitativement aux modifications de la densité des paires de Cooper dans le volume de chauffage. De plus, les vortex dans les supraconducteurs à haute température (SHT) ont également été imagés et manipuler optiquement pour la première fois. La méthode employée ici utilise un mécanisme de re-piégeage de flux dans lequel les vortex dans le SHT sont imagés à travers un supraconducteur à faible température critique, déposé au-dessus. Cette méthode ouvre la voie à l'étude d'interactions entre vortex uniques comme la torsion et la bouture, et au développement de techniques optiques pour piloter les propriétés transport dans les dispositifs SHT.

Mots-clés : supraconductivité, jonctions Josephson, imagerie magnétooptique, vortex d'Abrikosov